Microstructural characterization and multiscale ionic conductivity in lithium and sodium-based solid state electrolytes

Zur Erlangung des akademischen Grades einer

DOKTORIN DER NATURWISSENSCHAFTEN

(Dr. rer. nat.)

von der KIT-Fakultät für Chemie und Biowissenschaften

des Karlsruher Instituts für Technologie (KIT)

genehmigte

DISSERTATION

von

M. Sc. Charlotte Alina Fritsch

1. Referent: Prof. Dr. rer. nat. Helmut Ehrenberg

2. Referent: Prof. Dr. rer. nat. Annie K. Powell

Tag der mündlichen Prüfung: 12.04.2021

Affidavit - Selbstständigkeitserklärung

Die vorliegende Arbeit wurde im Zeitraum vom 15. November 2018 bis 1. März 2021 am Institut für Angewandte Materialien - Energiespeichersysteme und am Institut für Anorganische Chemie der Fakultät für Chemie und Biowissenschaften am Karlsruher Institut für Technologie (KIT) unter der Leitung von Prof. Dr. Helmut Ehrenberg angefertigt.

Hiermit versichere ich, dass ich die vorliegende Arbeit selbstständig verfasst habe, dass ich keine anderen als die angegebenen Quellen und Hilfsmittel benutzt habe, dass ich die wörtlich oder inhaltlich übernommenen Stellen als solche gekennzeichnet habe und dass ich die Satzung des KIT zur Sicherung guter wissenschaftlicher Praxis in der jeweils gültigen Fassung beachtet habe.

Karlsruhe, den . . . .

. . . .
(**Charlotte Fritsch**)

"The language of experiment is more authoritative than any reasoning. Facts can destroy our ratiocination, not vice versa." - Alessandro Volta

Table of contents

List of abbreviations

Chemical element symbols of the periodic system of elements are not listed.

Kürzel	Bezeichnung
°C	Degree Celsius
a , b, c	Lattice parameters
A	Absorption multiplier
AC	Alternating current
a.e.	Auxiliary electrolyte
ASSB	All-solid-state-battery
a.u.	Arbitrary unit
Å	Angström
α	Thermal exansion coefficient
B	Magnetic field
BF	Bright field
C	Capacitance
CAM	Cathode active material
CGHE	Carrier gas hot extraction
cn	Coordination number
CPE	Constant phase element
C-rate	Charging-/ discharging rate
CV	Cyclic voltammetry
D	Diffusion coefficient, also temperature-induced line broadening
d	Lattice plane distance
DC	Direct current
def	Deficiency
DESY	Deutsches Elektronen Synchrotron
DF	Dark field
DSC	Differential scanning calorimetry
DWF	Debye-Waller factor
δ	Chemical shift
δ_g	Gradient pulse length
Δ	Diffusion time
$\Delta\nu(T)$	Central linewidth
E_{hkl}	Extinction
E_A	Activation energy
ED	Electron diffraction
EDS	Energy dispersive X-ray spectroscopy
EIS	Electrochemical impedance spectroscopy
EO	Ethylene oxide
eq.	Equation
ex	Excess
f	Correlation factor
f_j	Atomic form factor

F	Farad
F	Structure factor
$F(Q)$	Reduced total scattering function
FID	Free induction decay
FT	Fourier transformation
FWHM	Full width at half maximum
g	Field gradient strength
g_j	Occupation
g	Gram
$G(r)$	Total scattering pair distribution
$\vec{G}$	Reciprocal lattice vector
γ	Gyromagnetic ratio
h	hour
HAADF	High Angle Annular Dark Field
HF	High freqency
h, k, l	Miller indices of crystallographic planes
ICP-OES	Inductively-coupled plasma optical-emission spectroscopy
$\text{Im}(Z)$	Imaginary part of complex resistance
i	Electric current, imaginary number
I	Intensity, Nuclear spin quantum number
IR	Infrared spectroscopy
J	Spectral density
k	Scale
k_B	Boltzmann constant
$\vec{k}$	Wave vector
K	Kelvin
K	Shape factor
KIT	Karlsruher Institut für Technologie
l	medium jump length
L	Crystallite size orthogonal to lattice plane
L_Θ	Lorentz geometry
LATP	Lithium Aluminium Titanium Phosphate
LCO	Lithium Cobalt Oxide
LIB	Lithium ion battery
LiTFSI	Lithium bis(trifluoromethanesulfonyl)imide
LLZO	Lithium Lanthanum Zirconium Oxide
λ	Wave length
m	Meters
M	Atom mass
M_x	Magnetization in x-direction
MAS	Magic angle spinning
MEM	Maximum entropy method
min	Minute
mL	Milliliter
MLN	Motional line narrwowing

MLZ	Heinz Maier-Leibnitz Zentrum
μ	Magnetic moment
N_A	Avogadro constant
N_{Li^+}	concentration of Lithium ions
NASICON	Sodium (Na) Superionic Conductor
NCM	Lithium nickel cobalt manganese oxide
nm	Nanometers
NMR	Nuclear resonance spectroscopy
NPD	Neutron powder diffraction
n.s.	Not specified
NZP	$NaZr_2(PO_4)_3$ - derived structure (Space group No. 167)
ν	Frequency
ω	Angular frequency
ω_L	Larmor frequency
p	Multiplicity
P	Nuclear spin
$P_\ominus$	Polarization
PETRA	Positron-Elektron-Tandem-Ring-Anlage
PDF	Pair distribution function
PEO	Polyethylene oxide
PFG	Pulsed field gradient
PISE	Polymer-in-salt-electrolytes
PLD	Pulsed laser deposition
PTMC	Poly(trimethylene carbonate)
PXRD	Powder X-ray diffraction
ϕ	Phase angle
q	Charge
Q	Constant phase element
$\vec{Q}$	Scattering vector
R_1	Relaxation rate
σ	(Ionic) conductivity
SEM	Scanning electron microscopy
Sst	Stainless Steel
STEM	Scanning transmission electron microscope
r	Distance
R	Resistance, also displacemet vector
R^2	Mean square displacement
$Re(Z)$	Real part of complex resistance
RF	Radio frequency
rpm	Revolutions per minute
RT	Room temperature, 25 °C
SAED	Selected area electron diffraction
SIB	Sodium ion battery
SG	Space group
$S(Q)$	Total structure function

SHE	Standard hydrogen electrode
SSE	Solid state electrolyte
st	Stoichiometric
σ	Conductivity
σ_g	Gradient shape factor
t_j	Temperature factor
T	Temperature
T_{hkl}	Preferred orientation factor
T_c	Onset temperature f motional narrowing
T_1	Spin lattice relaxation time
T_2	Spin-spin relaxation time
T_2^*	Time constant of FID
T_V	Vogel Temperature
TED	Transmission electron diffraction
TEM	Transmission electron microscopy
TGA	Thermogravimetric analysis
τ	Mean size of ordered crystal domains
τ_1	Jump rate
τ_c	Correlation time
θ	Scattering angle, also referred to as bragg position
U	Electric potential, voltage and halfwidth parameter
VTF	Vogel-Tamman-Fulcher equation
V	Halfwidth parameter
W	Halfwidth parameter
W_S	Warburg short
x	Molar fraction
XAS	X-ray absorption spectroscopy
XRD	X-ray diffraction
XRF	X-ray fluorescence spectroscopy
Z	Complex resistance

Zusammenfassung

Um dem zunehmenden Bedarf an Energiespeichersystemen für mobile Geräte, Elektrofahrzeuge und stationäre Energiespeicher gerecht zu werden, werden die vorhandenen Batterietechnologien ständig weiterentwickelt. Ein wichtiges Kriterium für die Leistung der Batterie ist ihre Energiedichte. Obwohl die Kathode einen Großteil des Gewichts einer Lithium-Ionen-Zelle ausmacht, besteht eine vielversprechende Möglichkeit zur Gewichtsersparnis auf der Anodenseite, indem Graphit durch reines Lithiummetall ersetzt wird. Zu diesem Zweck muss ein Elektrolyt entwickelt werden, der insbesondere gegen das Potential des Lithium Metalls stabil ist. Flüssige Elektrolyte können diese Anforderung nicht erfüllen und beherbergen außerdem Sicherheitsrisiken wie Entflammbarkeit. Festkörperelektrolyte sollen folglich die Verwendung einer Li-Metallelektrode ermöglichen. Aufgrund von Ressourcenknappheit werden außerdem Technologien auf Natriumbasis für den Einsatz als stationäre Energiespeicher entwickelt.

Thiophosphate weisen unter allen Festelektrolyten die höchsten Ionenleitfähigkeiten auf. In vielen Fällen bieten amorphe Thiophosphate noch höhere Leitfähigkeiten als ihre kristallinen Analoga, begründet in strukturellen Unterschieden. Eine strukturelle Untersuchung amorpher Verbindungen ist mit Standard-Röntgendiffraktion nicht möglich. Ihre lokale Struktur muss jedoch aufgeklärt werden, damit eine reproduzierbare Synthese stattfinden kann.

Der amorphe Festkörperelektrolyt $Na_2P_2S_6$ wurde über Kugelmahlen synthetisiert und anschließend thermisch kristallisiert. Der amorphe Feststoff zeigt eine von der kristallinen Komponente verschiedene Struktur. Eine Kombination aus XRD-PDF-Analyse und ^{23}Na / ^{31}P MAS-NMR zeigt, dass einzelne PS_4^{3-} Tetraeder und eckenverknüpfte Tetraeder während der Kristallisation in kantenverknüpfte Tetraeder umgewandelt werden. Der Prozess des Kristallisierens kann durch (erneutes) Kugelmahlen umgekehrt werden. Mit Impedanzspektroskopie wird gezeigt, dass amorphes $Na_2P_2S_6$ eine um drei Größenordnungen bessere Leitfähigkeit von $5.7 \cdot 10^{-8}$ S cm^{-1} als kristallines $Na_2P_2S_6$ ($2.6 \cdot 10^{-11}$ S cm^{-1}) zeigt. Die höhere Leitfähigkeit kann durch Kugelmahlen von kristallinem $Na_2P_2S_6$ zurückgewonnen werden.

Lithium-Lanthan-Zirkonoxid (LLZO) weist eine hohe Ionenleitfähigkeit und Stabilität gegenüber Lithiummetall auf und ist daher ein vielversprechender Kandidat als Festkörperelektrolyt. Spezifikationen zur Leitfähigkeit sind jedoch häufig nicht zuverlässig oder streuen. Zumeist werden die streuenden Leitfähigkeitswerte den unterschiedliche Substituenten, Sinterzeiten oder Oberflächenpassivierungen zugeschrieben.

Ein mikrostruktureller Vergleich von vier unterschiedlich substituierten LLZO Proben wird durchgeführt, um die Gründe für die unterschiedlichen Leitfähigkeiten aufzuklären.

Röntgenbeugung zeigt, dass kommerzielle LLZO-Proben in der Hydrogranat-Struktur (Raumgruppe Nr. 220) kristallisieren, welche erstmals mit einem Substituenten auf den Zr- und La-Lagen beschrieben wird. Das Kugelmahlen von Al^{3+}, Nb^{5+}, Ta^{5+} and W^{6+} substituiertem LLZO führt zu einer Phasentransformation von der Granat-Struktur in die Hydrogranat-Struktur mit einer niedrigeren Symmetrie. In der Hydrogranat-Struktur liegt eine im Vergleich zur Granat-Struktur verschiedene Verteilung der Lithium Ionen vor. Dies wurde mit ^{6}Li MAS-NMR und Neutronendiffraktion untersucht. Weiter unterscheidet sich auch die lokale Struktur. Im Hydrogranat ist eine größere Verzerrung von ZrO_6-Oktaedern mit Totalstreuung zu erkennen. Die Umwandlung von Hydrogranat-LLZO in Granat-LLZO erfolgt durch eine Kalzinierung bei 1100°C für 10 h. Mit Hochtemperatur-Röntgenbeugungsmessungen zeigt sich eine äußerst geringe thermische Ausdehnung der Hydrogranat Einheitszelle im Vergleich zur größeren Ausdehnung der Granat Einheitszelle.

Die Ionenleitfähigkeit im Hydrogranat wird mittels Linienformanalyse, Relaxometrie und Feldgradienten-NMR untersucht. Die Mobilität des Lithiums zeigt sich signifikant erniedrigt. Dies kann in Kombination mit der Strukturanalyse auf die hohe Besetzung der Li3 Position im Hydrogranat-LLZO zurückgeführt werden. Diese blockiert die langreichweitige Lithiumdiffusion. Aufgrund der Phasenumwandlung während der Kalzinierung ist die Bestimmung der Leitfähigkeit mit Impedanzspektroskopie nur für die Granat-Struktur möglich. Für diese liegen die ionischen Leitfähigkeiten im Bereich von 10^{-4} S cm^{-1}.

Die Fragestellung, ob die langreichweitige Lithium Mobilität in der Hydrogranat-Struktur im Vergleich zur Granat-Struktur verringert ist, wird durch die Verwendung eines LLZO-Polymer Kompositelektrolyten vertieft. Unter dessen Einsatz ist keine Sinterstufe zur Ermöglichung von Impedanzmessungen nötig. Es wird eine Leitfähigkeit (25 °C) von $1.2 \cdot 10^{-6}$ S cm^{-1} für einem Kompositelektrolyten mit Hydrogranat-LLZO und $3.4 \cdot 10^{-6}$ S cm^{-1} für einen Kompositelektrolyten mit Granat-LLZO gemessen. Auch die gemessene Aktivierungsenergie der Diffusion ist im Hydrogranat-Äquivalent höher. Die verringerte Ionenleitfähigkeit des Hydrogranat-Komposits wird mit Feldgradienten-NMR Messungen des Li-Diffusionskoeffizienten verifiziert. Es werden außerdem "Blindtests" mit Kompositelektrolyten durchgeführt, die keine oder die nicht-ionenleitende SiO_2 Keramik enthalten. Unter einem Verzicht auf die keramische Komponente leidet die Leitfähigkeit. Mit SiO_2-Anteil hingegen können ebenfalls sehr hohe ionische Leitfähigkeiten erzielt werden. Der nächste Schritt zur Optimierung eines Festkörperelektrolyten hinsichtlich der Ionenleitfähigkeit besteht darin, seine Kompatibilität mit den Elektroden, hier der Kathode, zu untersuchen. Diese Untersuchungen sind auch im Hinblick auf eine Beschichtung von NCM mit LLZO unter dem Einsatz eines Thiophosphat-Separators nötig.

Die Grenzfläche von LLZO zum etablierten Kathodenmaterial Lithium Nickel Cobalt Mangan Oxid (NCM) wird mittels Hochtemperatur-Röntgendiffraktion, [6]Li MAS-NMR und Transmissionselektronenmikroskopie bestimmt. Ein vereinfachtes System aus LLZO und NCM wird auf seine Lithiumdifusionsbarriere elektrochemisch unter dem Einsatz eines Hilfselektrolyten mit Impedanzspektroskopie vermessen. Das Kathodenkomposit Pellet wird dafür zwischen zwei Lagen eines LLZO-Polymer-Kompositelektrolyten eingebracht. Die Trennung von elektrischer und ionischer Leitfähigkeit kann aufgrund der relativ hohen elektrischen Leitfähigkeit des Elektrolyten nicht vollständig erfolgen. Das Prinzip der Messung unter dem Einsatz eines Hilfselektrolyten konnte jedoch erfolgreich realisiert werden.

Der Elektrolyt Lithium Aluminium Titan Phosphat (LATP) wird im Hinblick auf eine Hochskalierung der Synthese kristallografisch untersucht. Dabei wird der Phosphorsäuregehalt in der Synthese variiert. Es kommt unter einem Überschuss an Phosphorsäure zur Ausbildung von $AlPO_4$, das die Leitfähigkeit beeinträchtigt. Bei stöchiometrischem Verhältnis der Ausgangsstoffe kommt es nicht zur Ausbildung von Fremdphasen. Bei einem Mangel an Phosphorsäure bildet sich $LiTiOPO_4$. Diese Fremdphase beeinträchtigt die Leitfähigkeit nicht in negativer Weise, behindert allerdings die Verdichtung des Materials.

Die Erkenntnisse aus dieser Arbeit leisten einen Beitrag zum Verständnis struktureller Veränderungen von Festelektrolyten während der Verarbeitung und tragen damit zu einer Verbesserung von künftigen Feststoffbatterien bei.

1. Abstract

In order to meet the increasing need for energy storage systems in consumer devices, electric vehicles and stationary energy storage devices, the existing battery technologies are constantly being further developed. An important criterion for the performance of the battery is its energy density. Even if the cathode accounts mostly for the weight of a lithium ion battery cell, there is a promising possibility of weight saving on the anode side by replacing graphite with pure lithium metal. To this end, an electrolyte needs to be developed that is stable against the potential of the pure metal. Liquid electrolytes cannot meet this requirement and also involve safety risks as flammability. Solid-state electrolytes are supposed to enable the use of a lithium-metal electrode.

Additionally, due to the scarcity of resources for lithium, sodium-based technologies are being developed for use as stationary energy storage devices.

Thiophosphates feature the highest ionic conductivities among all solid electrolytes. In many cases, amorphous thiophosphates offer even higher conductivities than their crystalline analogues and their structure can differ, too. A structural investigation of amorphous compounds may not be possible with a standard X-ray analysis. However their local structure has to be enlightened so that a reproducible synthesis can take place.

The solid electrolyte $Na_2P_2S_6$ was synthesized via ball milling in an amorphous state with subsequent crystallization. The structure of the crystalline phase differs markedly compared to the corresponding amorphous phase. A combination of XRD-PDF analysis and ^{23}Na/^{31}P MAS NMR spectroscopy measurements indicate that single PS_4^{3-} tetrahedra and corner-sharing tetrahedra are transformed to edge-sharing-tetrahedra during crystallization of amorphous $Na_2P_2S_6$ to crystalline $Na_2P_2S_6$. Impedance spectroscopy shows that amorphous $Na_2P_2S_6$ has a conductivity of $5.7 \cdot 10^{-8}$ S cm^{-1} which is three orders of magnitude higher than crystalline $Na_2P_2S_6$ ($2.6 \cdot 10^{-11}$ S cm^{-1}). The higher conductivity can also be recovered by ball milling crystalline $Na_2P_2S_6$, inducing a re-amorphization.

Lithium Lanthanum Zirconium oxide (LLZO) exhibits a high ionic conductivity and stability against lithium metal and is therefore a promising candidate as solid state electrolyte. Yet, specifications on its conductivity are often not reliable and spread widely. Attempts are made to attribute the differences in reported conductivities to the different substituents, sintering times or surface passivations. A microstructural comparison of four differently substituted samples is performed to elucidate the reasons for the different conductivities.

X-ray diffraction revealed that commercial LLZO samples crystallize in the hydrogarnet structure (space group No. 220), which is described for the first time with a substituent

on Zr and La sites. Ball milling of Al^{3+}, Nb^{5+}, Ta^{5+} and W^{6+} substituted LLZO results in a phase transformation from the garnet structure into the hydrogarnet structure with a lower symmetry. The distribution of lithium ions in the hydrogarnet structure differs from that in the garnet structure which was investigated with ^{6}Li MAS NMR and neutron diffraction. A targeted conversion of the hydrogarnet structure into the garnet structure is proved by calcining the material at 1100 °C for 10 h. With high-temperature X-ray diffraction, an low thermal expansion of the hydrogarnet unit cell is observed in comparison to the greater expansion of the garnet unit cell. The ionic mobility of Li ions in the hydrogarnet structure is examined by means of NMR, in particular line shape analysis, relaxometry and pulsed-field gradient NMR. This combination of techniques shows that the mobility of lithium is significantly reduced on small length scales. In combination with the structural analysis, this can be traced back to the high occupancy of the Li3 position in the hydogarnet structure, blocking long-range lithium diffusion. However, it was not possible to access the long-range mobility of Li in the hydrogarnet structure (at 25 °C).

Therefore, the contribution of the ceramic component to the total ionic conductivity of polymer composite electrolytes is evaluated. The question whether the long-range lithium mobility in the hydrogarnet structure is lower compared to the garnet structure is assessed without the necessity for sintering the LLZO to pellets. Impedance spectroscopy shows a conductivity of $1.2 \cdot 10^{-6}$ S cm^{-1} for a composite electrolyte with a hydrogarnet structure and $3.4 \cdot 10^{-6}$ S cm^{-1} for a composite electrolyte with a garnet structure. The higher Li mobility of the garnet-based composite electrolyte compared to the hydrogarnet-based electrolyte is verified with PFG-NMR measurements of the diffusion coefficient: $6.1 \cdot 10^{-14}$ m^2 s^{-1} (garnet), resp. $1.1 \cdot 10^{-14}$ m^2 s^{-1} (hydrogarnet). The measured activation energy of diffusion is also higher in the hydrogarnet composite. The conductivity results measured with impedance spectroscopy are compared with commercial composite electrolytes; a SiO_2-ceramic-polymer and a purely polymer-based electrolyte.

The next step from optimizing a solid state electrolyte in terms of ionic conductivity is to look at its compatibility with the electrodes, here the cathode. It is tested whether ball milling of LLZO with the established cathode material Lithium Nickel Cobalt Manganese oxide (NCM) results in a good contact of the two materials and consequently a low Li ion diffusion barrier.

The interface between LLZO and NCM is investigated by X-ray diffraction, ^{6}Li MAS NMR and transmission electron microscopy. A model system consisting of LLZO and NCM is characterized with impedance spectroscopy for a lithium diffusion barrier sandwiched between an auxiliary electrolyte in order to separate the ionic conductivity from

the electrical. An evaluation of only the ionic conductivity apart from the electrical conductivity is not possible due to the high electrical conductivity of the auxiliary electrolyte.

The electrolyte Lithium Aluminum Titanium Phosphate (LATP) is examined crystallographically against the background of upscaling of the synthesis. If the process is upscaled, local inhomogeneities of the educts can be expected in a way that varying educt contents have an effect on the product. This applies especially to phosphoric acid, the concentration of which cannot be specified precisely due to its hygroscopy. A Rietveld refinement analysis against X-ray diffraction data of LATP with varying phosphoric acid content during synthesis is performed. An excess of phosphoric acid leads to the formation of $AlPO_4$, which impedes the ionic conductivity. Insufficient phosphoric acid causes the formation $LiTiOPO_4$. TiO_2 is formed in this material after a second sintering step.

The findings in this work contribute the understanding of structural changes in solid electrolytes during processing and thus contribute to the improvement of future solid-state batteries.

2. Theory

2.1. Structural characterization

Diffraction is used in this work to elucidate the long-range order of crystalline solids. It can also be used to determine the site occupation in crystal structures, which alongside with nuclear magnetic resonance and impedance spectroscopy, can provide information about the Li mobility. The local structure was examined with NMR and PDF. Here, NMR is particularly suitable for making a distinction between different atomic environments around the observed nuclei. Especially structural units like molecules can be examined with PDF. Raman is used to detect covalent bonds, too, and can also be used to detect impurities that are not visible with diffraction due to the small particle size.

2.1.1. Diffraction

The principle of diffraction for investigating crystalline materials is the generation of constructive interference on the crystal lattice. The obtained diffraction pattern allows to draw conclusions about the crystal structure.

Constructive interference is achieved when the phase shift of the scattered wave with the wavelength λ is an integer multiple of the product of the lattice plane distance d times the double sine of the angle of incidence θ. From this the Bragg equation 1 emerges.

$$n \cdot \lambda = 2d \cdot \sin(\theta) \tag{1}$$

The Laue condition for constructive interference in the scattering on a crystal can be demonstrated with the help of the Ewald sphere. Constructive interference in a scattering process is obtained, if the change in the wave vector $\vec{k}$ corresponds to a reciprocal lattice vector $\vec{G}$, see eq. 2. This is called Laue condition. The Ewald sphere is used to link the real and the reciprocal space.

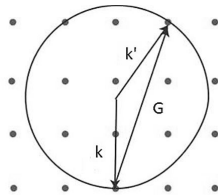**Figure 1** – Ewald construction.

$$\vec{k} - \vec{k'} = \vec{G} \tag{2}$$

One way to implement the powder diffraction experiment is the Debye-Scherrer method with monochromatic light. A diffraction pattern arises from the image of the circular

spreading Debye-Scherrer cones by rotation of the lattice planes around the incident X-ray beam. The Debye Scherrer method allows no distinction of (hkl) planes with the same d value.

The distance between two scattering atoms corresponds to the lattice distances d. The Miller indices can be calculated according to eq. 3 from the d values. In this example eq. 3 is for a cubic lattice ($a_0 = b_0 = c_0$).[61,77]

$$d_{hkl} = \frac{a_0}{\sqrt{h^2 + k^2 + l^2}} \tag{3}$$

Translation grids, sliding mirror planes or screw axes can cause extinction of reflections through phase shift of $d/2$.

A diffraction pattern is always centrosymmetric. This is called Friedels law and allows no differentiation whether there is an (additional) inversion center in the crystal or not. We distuingish between 11 Laue groups, 32 point groups or 230 space groups and seven crystallographic families: cubic, monoklin, triklin, orthorhombic, tetragonal, trigonal and hexagonal.

Rietveld refinement

The Rietveld structure refinement is a calculation method for diffration patterns out of crystallographic models that is used to analyze diffraction data.[146] Quantitative determination of crystalline phases is possible. Real-structure effects such as reflection broadening due to small crystallite sizes and microstrain can be detected. For Rietveld refinement in this study, the software *FullProf* was used.[148] This software calculates diffraction patterns using eq. 4 and 5. The aim of the refinement is an adaptation of the calculated diffraction pattern in such a way that the smallest possible deviation of the calculated from the measured intensities is obtained. The crystallographic data of the initial diffraction pattern can be obtained from the ICSD database.[2]

Equation 4 describes the intensity of Bragg reflections.

$$I_{hkl} = k \cdot p_{\mathrm{hkl}} \cdot L_\theta \cdot P_\theta \cdot A_\theta \cdot T_{\mathrm{hkl}} \cdot E_{\mathrm{hkl}} \cdot |F|^2 \tag{4}$$

Those factors are in order from left to right scaling k, multiplicity p_{hkl}, Lorentz geometry L_θ, polarization P_θ, absorption A_θ, orientation T_{hkl}, extinction E_{hkl}, and the structure factor F. The structure factor F is calculated with eq.5.

$$F_{hkl}(\vec{G}) = \sum_{j=1} g_j \cdot t_j \cdot f_j \cdot e^{2\pi \cdot \vec{G} \cdot \vec{x}_j} \tag{5}$$

The intensity of the reflection is also determined by the occupation number g, temperature factor t, atomic form factor f and reciprocal lattice vector $\vec{G}$.

Size broadening can be calculated with the Scherrer equation. τ is the mean size of ordered crystal domains. K is a shape factor. λ is the wave length, L is the crystallite size orthogonal to the lattice plane and θ is the Bragg position.

$$\tau = \frac{K \cdot \lambda}{L \cdot \cos \theta_0} \qquad (6)$$

Microstrain and size effects lead to Gaussian and Lorentian contributions in the peak shape which is modeled with a double-Voigt approach.[160]

Debye-Waller factor

The Debye-Waller factor (DWF) is used to describe the attenuation of X-ray scattering by thermal motion in a crystal lattice. The expression is given by eq. 7. k_{B} is the Boltzmann constant, ω is the vibration number with the dimension $2\pi/\mathrm{s}$, M is the mass of the atom.

$$\mathrm{DWF} = e^{\frac{-k_B \cdot T \cdot |\vec{G}|^2}{M \cdot \omega^2}} \qquad (7)$$

Vegard's law

Assuming two components A and B having the same crystalline structure, a solid solution of both has a lattice parameter that is linear dependent on the molar fraction of the components, see eq. 8.[181]

$$a_{\mathrm{A}_{(1-x)}} = (1 - x)a_{\mathrm{A}} + x a_{\mathrm{B}} \qquad (8)$$

Neutron diffraction

The elastic scattering of neutrons, also called neutron diffraction, can be used for structural analyses. The scattering cross section is a function of the nucleus and is different for each element and isotope. In contrast to X-ray scattering, there is no trend in the periodic system as increasing atomic number. Neutron diffraction is especially appropriate to localize hydrogen atoms.[105]

Neutron scattering lengths are smaller than X-ray scattering lengths (factor 1-300 for atomic numbers 1-100). The neutron scattering lengths hardly decrease with increasing diffraction angle. This is because the nucleus, in contrast to the electron shell, has no spatial expansion or diffusivity. A requirement for carrying out neutron diffraction experiments is the access to research reactors and spallation sources.

2.1.2. Total scattering pair distribution function

We find diffuse scattering in the background of a powder diffraction pattern. It represents the local structure in a radial distribution and thus possibly a deviation from the average

crystal structure.

The experiment is similar to an X-ray diffraction experiments with a analysis of the diffraction pattern. However, it is necessary to record high Q in order to enable a high resolution in direct space and avoid noise from termination ripples.

$$Q = 4\pi \sin(\theta)\lambda^{-1} \tag{9}$$

Here, Q is the magnitude of the scattering vector. The resulting pair distribution function (PDF), $G(r)$ represents the probability of finding another atom at a distance r in direct space (in contrast to the reciprocal space of classical diffraction methods). Fig. 2 illustrates the principle of the measurement compared to X-ray diffraction. The position
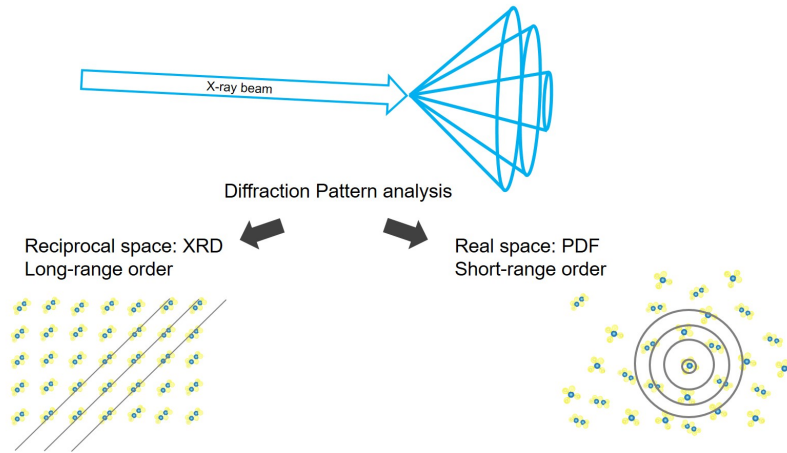

Figure 2 – Principle of PDF analysis in comparison to X-ray diffraction.

of the peaks in a PDF is determined by the atom-to-atom distances, while the decay of the function contains the crystalline correlation length (crystallite size) and depends also on the Q-resolution of the device.

2.1.3. Nuclear magnetic resonance spectroscopy

Felix Bloch and Edward Mills Purcell first demonstrated nuclear magnetic resonance signals in 1946.[12,136] Since then, NMR spectroscopy has developed into one of the most important methods in structure analysis.

Nuclear magnetic resonance spectroscopy (NMR) is a versatile tool for observing local structure and dynamics in solids. Various techniques exist to measure short-and long-range mobility such as linewidth dependency, relaxation and pulsed-field gradient spectroscopy.

The underlying principle is the excitation of nuclear spins with radio frequencies. The gyromagnetic ratio γ as a substance-specific constant is linked to the magnetic moment μ and the nuclear spin P.

$$\mu = \gamma \cdot P \tag{10}$$

The nucleus is excited by applying the so-called Larmor frequency ω_L. B_0 is the static magnetic field.

$$\omega_L = \gamma \cdot B_0 \tag{11}$$

The position of an resonance signal is depicted in units of chemical shift δ depending on the resonance frequency of a reference material ν_0.

$$\delta = \frac{\nu_0 - \nu}{\nu_0} \tag{12}$$

The setup of such an experiment with transmitter and receiver coil is shown in Fig. 3. For the measurement, the sample is placed in a homogeneous magnetic field. The sample is surrounded by an induction coil, which generates a high-frequency electromagnetic alternating field B_1 perpendicular to the main magnetic field B_0.

A Free-induction decay spectrum is obtained by switching off the B_1 field in x-direction
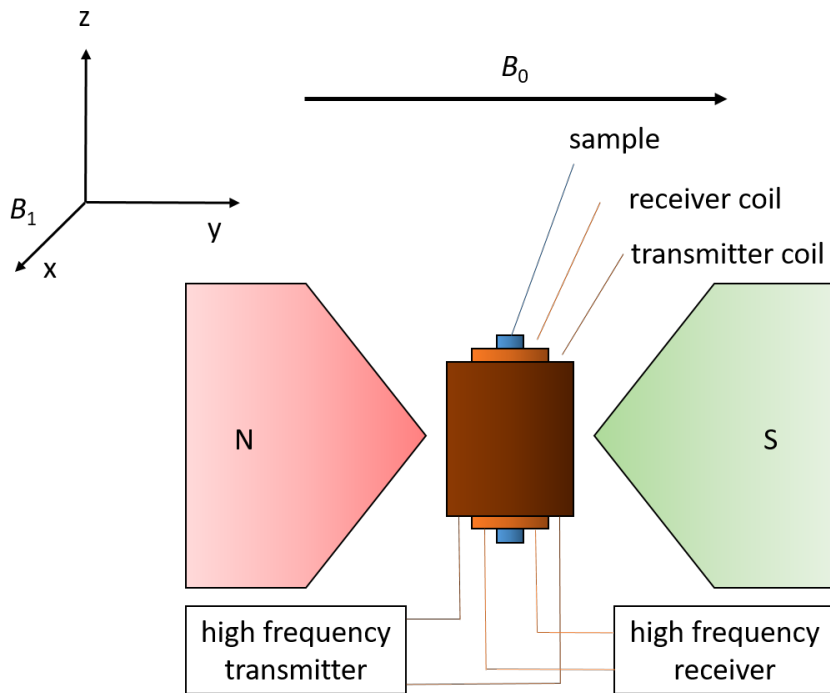

Figure 3 – Schematic setup of a NMR spectrometer.

which induces a voltage in the receiver coil. The signal decays exponentially with the time constant T_2^*. The transversal components (M_x and M_z) of the magnetization vanish. Usually the time-dependent signal is Fourier-transformed into a frequency-dependent signal.

Modern methods no longer send continuous alternating fields to the sample, but rather radio wave pulses. A short radio wave pulse stimulates a frequency band whose frequency band width is inversely proportional to the pulse duration. As a result, all transitions

that can be excited by this frequency are excited simultaneously. With the correct choice of pulse duration and pulse power, the magnetization of the excited nuclear spins can be brought into the transverse plane perpendicular to the main magnetic field. After the end of the pulse, this transverse magnetization oscillates for a short time perpendicular to the main magnetic field. These oscillations are detected as an electric current via electromagnetic induction with the same induction coil that was used to send the excitation pulse.

A drawback of NMR spectroscopy is its comparatively low signal-to-noise ratio. This is due to the fact that the energy differences between the excited states and ground states are small. Therefore, the Boltzmann-distributed population differs only slightly. This disadvantage can be compensated by a higher polarization of the nuclear spins, which is why the development of the devices aims at stronger magnetic fields.

MAS-NMR

The local order in solids is governed by anisotropic effects such as dipole-dipole interactions causing line broadening. These effects can be averaged out by fast rotation of the sample at an angle of 54.7°, the "magic angle", relative to the orientation of the magnetic field. The rotation is implemented pneumatically with strong air flow on a paddle-wheel sample container, the so-called magic angle spinning (MAS-NMR).

MAS-NMR is utilized to analyze the local magnetic field of an atom. Differently shielded chemical environments can be detected and compared. This technique is particularly useful for the case of lithium which is difficult to localize with diffraction.

Relaxometry

NMR spectroscopy provides a variety of possibilities to monitor nuclear dynamics in a wide frequency range starting from nanoseconds up to the seconds.

Relaxation refers to the processes that causes the nuclear spin magnetization to return to its equilibrium state. These processes are based on different relaxation mechanisms and are described by relaxation times for the various magnetization components.

The T_1 relaxation time is the spin-lattice-relaxation or longitudinal relaxation. The T_2 relaxation time is the spin-spin relaxation time and describes the decay of the transverse magnetization M_z.

One way to gain information about small local jumps occurring with the frequencies close to the nuclear Larmor frequency ω_L is spin-lattice relaxation studies. In the experiment the relaxation time constant T_1 is measured as a function of temperature. If the motional frequency is rather small and differs a lot from the Li Larmor frequency, the relaxation process is not efficient enough to cause the fast loss of the stimulated magnetization.

With increasing temperature, the speed of the jumps also increases and T_1 decreases until the minimum T_1 is approached. Further heating and, thus, acceleration of the motion leads to the elongation of the relaxation time constant. This is a typical trend in the case of the simple model – isotropic 3D motion. Local hopping of ions or atoms causes fluctuations in the local magnetic/electric fields at the sites of the nuclei that cause transitions between the nuclear Zeeman levels and thus induce effective relaxation of the nuclear polarization. This relaxation is most effective when the average hoping rate τ_1 of the ions equals the resonance frequency of the nuclei ($\tau_1 \sim \omega_{\mathrm{Li}}^{-1}$). For the case of isotropic and uncorrelated motion of ions, the overall temperature dependence of the relaxation rate T_1^{-1} can be described according to Bloembergen, Purcell and Pound.[65,66,75,83,84,124]

$$T_1^{-1} = \frac{\tau}{1 + (\omega\tau)^2} \tag{13}$$

Here, ω_L, is the resonance frequency of the Li nuclei at a given magnetic field, τ_0^{-1} is a pre-exponential factor for the Arrhenius expression, E_{A} is the activation energy for single Li ion jumps, k_{B} is the Boltzmann constant, and T is the temperature. Thus, having the temperature dependence of the spin-lattice relaxation time, one can estimate the jump rate τ_1 and the activation energy E_{A} of the underlying motion with eq. 14.

$$\tau^{-1} = \tau_0^{-1} \cdot e^{-\frac{E_{\mathrm{A}}}{k_B T}} \tag{14}$$

The relaxation time T_1 is particularly sensitive to movements with correlation rates in the MHz range. In contrast, $T_{1\rho}$ measurements make it possible to record jump processes in the Hz to kHz range.

Relaxation mechanisms

Magnetic dipoles from neighboring atoms cause the relaxation of the nuclear spin. We differentiate between the following mechanisms of relaxations.

Intramolecular dipole-dipole-relaxation; A homonuclear interaction happens between the same types of nuclei within one molecule. It is particularly important for hydrogen atoms in organic molecules. If the two nuclei are not of the same element, we speak of a heteronuclear interaction.

Intermolecular dipole-dipole-relaxation plays a role in paramagnetic substances where it appears as nuclear-dipole-electron-dipole interaction. The dipole of the electron is utterly strong and exceeds those of the nucleus by three orders of magnitude. It leads to a strong peak broadening and to a very short transversal relaxation times.

Anisotropy of chemical shift occurs if the chemical shift of a nucleus in a molecule depends on the orientation of the molecule with respect to the direction of the external magnetic field. This only applies to fluids. Fast rotations in fluids or gases create magnetic fields

that act as *Spin-spin rotation*-relaxations.

Scalar coupling occurs if a nucleus is scalarly coupled to a second nucleus via spin-spin coupling and if the coupling changes over time.

Core-quadropole field gradient interaction applies to all nuclei with a nuclear spin $I > 1$. The charge distribution of the nucleus is not spherical any more but ellipsoidal. This causes the occurrence of an electrical quadrupolar momentum. This quadrupole can interact with electric field gradients, if they are present at the nucleus; the nuclear spin can thereby be reoriented and thus quadrupole field gradient relaxation can take place. This additional relaxation mechanism is usually very strong and therefore dominant for such nuclei. The mostly short relaxation times and thus the broad NMR resonance lines are characteristic of nuclei with $I > 1$.

Motional narrowing

This experiment is designed in a such way that the static NMR spectrum is measured as a function of temperature. To acquire the spectrum at each temperature step we used a quadrupolar echo pulse sequence, which is particularly relevant for the nuclei possessing quadrupolar moment, such as ^{7}Li. The quadrupolar echo experiment allows measuring the full broad signal, which undergoes significant spin-spin relaxation and might be obscured by the spectrometer dead-time. ^{7}Li static spectra at low temperatures contain at least two contributions – the narrow line which experiences dipolar couplings and the quadrupolar hump which appears at the base of the spectrum. We obtain the disappearing of the dipolar-caused broadening by heating and measuring the width of the narrow component vs. temperature.

In general, if the accessible temperature range is large enough, three regions can be distinguished in the FWHM as depicted in Fig. 4.[154] Note that Fig. 4 depicts two regions of line narrowing (T_c^{Li} and T_c^{Na} for LiNaSO$_4$).

- Rigid limit is represented by the upper plateau which is visible at low temperatures. The mobility is "frozen" (295 K in Fig. 4)

- Gradual line narrowing as a response to heating (400-450 K in Fig. 4)

- The lower plateau indicates that the motion is so fast that the residual dipolar coupling is smaller than the line width caused by field and sample inhomogeneity (750 K in Fig. 4)

If the exchange frequency exceeds the difference of resonance frequencies, line coalescence happens. For a single signal this means that the jump frequency exceeds linewidth, so-called motional narrowing. An empirical approach from Hendrickson and Bray can be
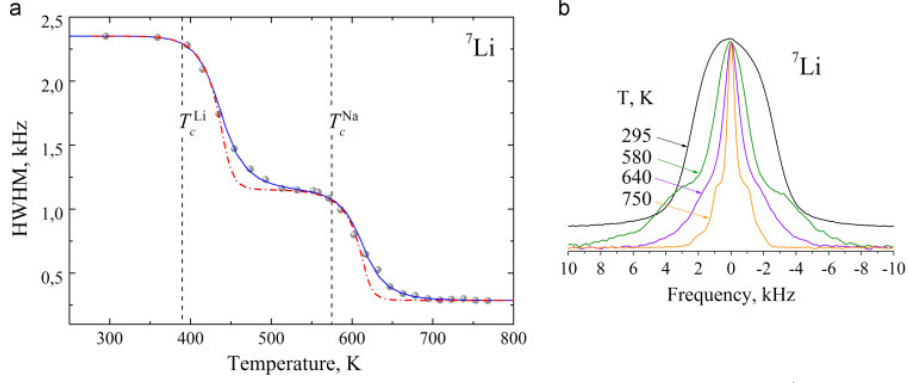
Figure 4 – Example of MLN for LiNaSO$_4$ (a) Temperature dependences of ^{7}Li NMR line width (HWHM) (dashed vertical lines indicate onset temperatures of the motional narrowing) and (b) corresponding NMR spectra, from[154]. Vertical dashed lines denote the onset temperature T_c of the motional narrowing.

used to calculate the activation energy of single ion jumps.[67]

$$\Delta\nu(T) = \Delta\nu_R \cdot [1 + \left(\frac{\Delta\nu_R}{B} - 1\right) \cdot e^{-\frac{E_A}{k_B \cdot T}}]^{-1} + D \qquad (15)$$

$\Delta\nu(T)$: Central linewidth
D : Magnetic field inhomogeneity
$\Delta\nu_R$: Linebroadening in ground state

Parameter B is attributed to the linewidth of the thermally activated nuclei.

Pulsed-field gradient NMR

A linear field gradient is applied along the direction of the magnetic field, making the resonance frequencies of the nuclei a function of their position in the field. Two pulse gradients are applied. The first gradient assigns the spins to a position with a phase angle of precession. After this pulse the ions diffuse over a specified time Δ. A second pulse turns the phase angles back. If a particle diffuses from one position to another between first and second pulse, then the magnetic field generated by the second gradient will not be able to reverse the phase coding generated by the first gradient. The consequence of this is a damping of the intensity of the generated echo.

We use the Stejskal-Tanner equation to determine the diffusion coefficient D from a variation of the field gradient strength g.[162]

$$I = I_0 \cdot e^{-D \cdot \gamma^2 \cdot \delta_g^2 \cdot \sigma_g^2 \cdot g^2 (\Delta - \frac{\delta}{3})} \qquad (16)$$

$$I \quad : \text{ signal intensity with pulsed gradient}$$

I : signal intensity with pulsed gradient

I_0 : signal intensity (without pulsed gradient)

γ : gyromagnetic ratio

δ_g : gradient pulse length

σ_g : gradient shape factor

g : field gradient strength

Δ : Diffusion time

The acquisition of the diffusion coefficients by PFG-NMR in solids is always linked with difficulties and limitations posed by the unfavorable relaxation parameters – spin-spin relaxation time which is rather short and spin-lattice relaxation which can reach hundreds of seconds.

Relation to diffusion

The methods listed above are used to examine the ionic mobility of lithium on various length scales. Fast local jumps of ions are a prerequisite for long range transport. The determination of this type of motion promotes the understanding of the hierarchy of mobility in solid electrolytes.

The Diffusion coefficient D can be calculated from the mean jump rate and the mean jump length with the Einstein-Smoluchosvski-equation.[35,184] Here, l is the average jump length of the Li ions, that can be estimated from the shortest Li-Li distance in the crystal structure.

$$D = f \cdot \frac{l^2}{6\tau} \tag{17}$$

Subsequently, the Li conductivity σ can be calculated with the Nernst-Einstein-equation. N_{Li} is the concentration of Li atoms and q is their charge.

$$\sigma_{\text{Li}} = \frac{D N_{\text{Li}} q^2}{k_{\text{B}} \cdot T} \tag{18}$$

2.1.4. Raman spectroscopy

The sample is irradiated with monochromatic laser radiation and the scattered radiation is analyzed. The Raman effect originates from changes in the polarizability of the electrons in a molecule, in contrast to infrared spectroscopy which relies on the dipole moment. Besides the elastically scattered Rayleigh radiation, a small part of the Laser light is inelastically scattered: Raman scattering. Radiation with lower and higher frequencies occurs as Stokes or Anti-Stokes lines. This inelastic scattering is called Raman scattering and is caused by molecular vibrations and rotations. Similar to infrared spectroscopy, we can conclude about the analyzed substance from the spectrum obtained.[115]

2.1.5. Infrared spectroscopy

The frequency of infrared (IR) radiation lies in the range of the rotational levels of molecules and the vibration levels of molecular bonds. Absorption leads to an excitation of vibrations in the bonds if it features a dipole moment. An IR spectrum is a very characteristic for each substance. Materials can be identified by comparing them with spectra from reference databases.

2.2. Electrochemical characterization

2.2.1. Impedance spectroscopy

Electrochemical impedance spectroscopy (EIS) is the measurement of the complex resistance with alternating current. After applying an alternating voltage one measures the resulting alternating amplitude of current, which has the same frequency as the voltage but is out of phase.

The most common way to visualize an impedance spectrum is the Nyquist plot. It was developed out of control engineering and is originally used to describe the stability of a system with feedback. It enables the representation of functions with complex-valued output values and is therefore suitable for displaying the phase shift of the input and output voltage as absolute value and phase angle.

The Nyquist plot separates imaginary and real part of a complex variable. The former can be associated with capacitance and inductance and the latter describes the resistance. For known thickness d and area a, a conductivity σ can be calculated out of the resistance R using eq. 19.

$$\sigma = \frac{d}{a \cdot R} \tag{19}$$

In an ideal case, we can assign the resistance of the bulk, grain boundary and the electrodes to a semicircle in the Nyquist plot as depicted in Fig. 5.[65] Resistance R and capacitance C are linked with equation 20 to the characteristic excitation frequency for either bulk or grain boundary. For the case that these frequencies do not differ significantly, the semicircles corresponding to bulk and grain boundary overlap and cannot be separated.[65]

$$\omega_{\mathrm{max}} = \frac{1}{RC} \tag{20}$$

Another form of representation is the Bode diagram. It depicts the amplitude and phase shift as a function of frequency.

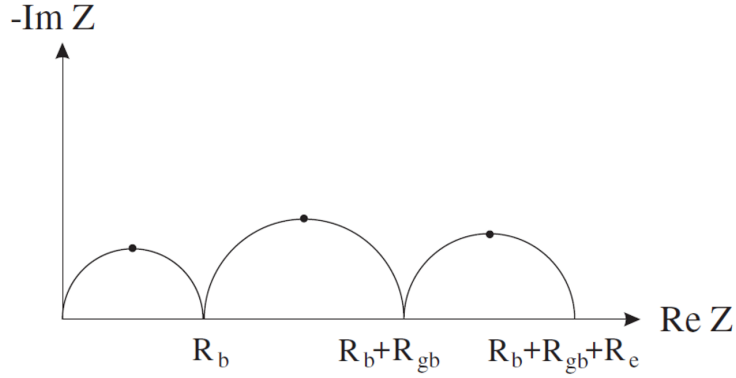For flattened semicircles we use a constant phase element Q (CPE) instead of a capacitor.

Figure 5 – Nyquist plot of impedance spectra with contributions from bulk (b), grain boundary (gb) and electrode (e) for $\omega_b \ll \omega_{gb} \ll \omega_e$, modified from Heitjans et al.[65]

Equation 21 calculates its impedance.

$$Z_{CPE} = \frac{1}{Q(i\omega)^n} \tag{21}$$

Fig. 6 depicts several electrical components that are used to model an electrolyte (or other battery components) and their shape in a Nyquist plot. Irvine et al. give a

Figure 6 – Electrical components and there shape in a Nyquist plot, taken from[152]. I: current, V: voltage.

phenomenological relation for measured capacitance values listed in table 1.[76]

Table 1. – Capacitance in an impedance measurement and their possible interpretation.[76]

Capacitance / F	Phenomenon
10^{-12}	bulk
10^{-11} - 10^{-8}	grain boundary
10^{-9} - 10^{-7}	surface layer
10^{-4}	electrochemical reactions

2.2.2. Chronoamperometry

A voltage is applied and the resulting current is measured as a function of time. After a certain time, the current reaches an equilibrium and via Ohm's law, the resistance can be calculated with equation 22, R is the resistance, U the voltage and i the current.

$$U = R \cdot i \tag{22}$$

Measuring the direct current with steel contacts we can assume there is no reservoir of moving charge carriers besides electrons so the resistance is a simple electrical resistance after the current has reached equilibrium. Together with a measurement of the total conductivity with impedance spectroscopy, the contributions from electrical and ionic conductivity can be separated.

2.3. Optical characterization

2.3.1. Scanning electron microscopy

An electron beam is accelerated through an electrical field and the sample is scanned through the inelastic and elastically scattered electrons. This is proceeded in high vacuum not to hinder electron movement. The electrons stem from the surface of the sample and thus give information about its morphology.

2.3.2. Transmission electron microscopy and electron diffraction

In the sample to be examined, the electrons change their direction of movement in the form of Rutherford scattering. In some cases they also lose kinetic energy (inelastic scattering). Elastically scattered electrons that leave the object at the same angle are focused in one point in the back focal plane of the objective lens. With a diaphragm (lens diaphragm or contrast diaphragm), only the electrons that have not been scattered can pass through in this plane. Since atoms with a higher atomic number and thicker object areas scatter more, the resulting contrast is called mass thickness contrast. In

the case of amorphous solids, this enables a very simple interpretation of the obtained micrographs. The contrast of crystalline materials follows more complicated laws and is called diffraction contrast. Since, under certain conditions, the micrograph intensity shows strong variations with small local changes in the crystal structure (inclination, atomic distance), as they occur in the vicinity of crystal structural defects (various-dimensional defects) due to internal stresses in the lattice, the real structure of solids can be excellently examined.
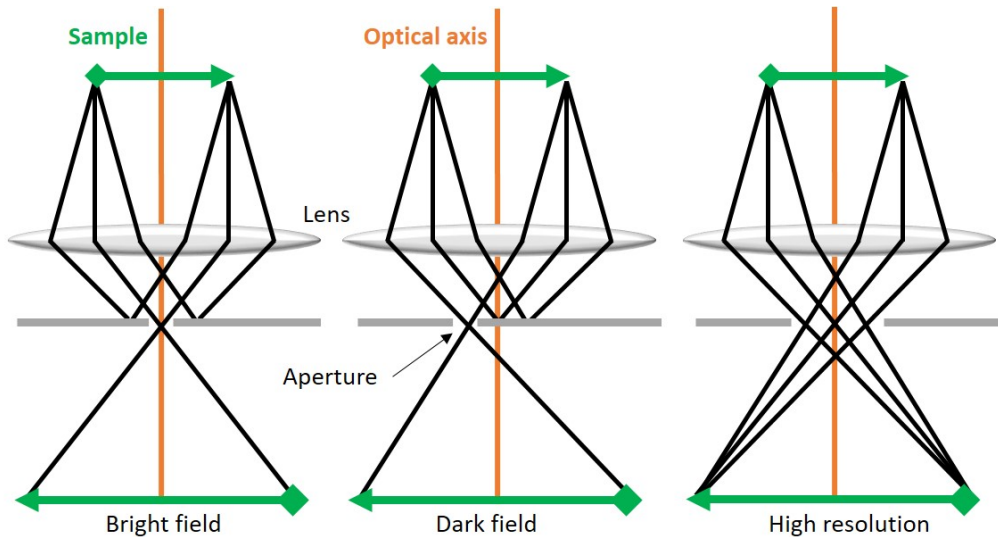
Figure 7 – TEM imaging modes: scheme of the ray paths from the object (sample) to the micrograph, shown in side view along the optical axis.

Fig. 7 schematically explains the different imaging modes: Bright field (BF), dark field (DF) and high resolution TEM (HRTEM).[97] With the high angle annular dark field signal (HAADF) of the scanning transmission electron microscope, an incoherent high-resolution micrograph can be achieved.

Scanning transmission electron microscopy

A scanning transmission electron microscope (STEM) is an electron microscope in which an electron beam is focused on a thin sample and scans a certain field line by line. The primary electrons transmitted through the sample are generally used as the image signal. Their current is measured synchronously with the position of the electron beam. According to the imaging technique, STEM is a sub-form of the scanning electron microscope (SEM). The examination geometry is according to a transmission microscope. The same requirements are placed on the samples in terms of transparency as with the transmission electron microscope.

Electron diffraction

Transmission electron diffraction (TED/ED) is a standard method in a TEM measurement. The combination of imaging and diffraction in a transmission electron microscope is particularly informative.

Electrons radiate through the object which therefore must be sufficiently thin. Depending on the atomic number of the atoms that make up the object, the level of the accelerating voltage and the desired resolution, the sensible object thickness can range from a few nanometers to a few micrometers.

2.4. Diffusion and ionic conduction in solids, polymers and composites

The movement of ions in a crystal is primarily governed by defects, e.g. vacancies and interstitials but also partial occupancies. Both can be influenced by doping and substitution which can also influence the unit cell volume which in turn can facilitate ionic movement eg. by widening 'bottlenecks' in crystal structures for diffusion.

Schottky- and Frenkel defects

Schottky defects are the pairwise appearance of vacancies in the crystal lattice. These vacancies occur in the chemical equilibrium of a crystal because they increase its entropy. The vacancies can migrate through the crystal through ion movement. An example of crystals with a high amount of Schottky defects are alkali halides.

The second type of point defect is the Frenkel defect. It arises from the irregular occupation of interstitial spaces. Frenkel defects increase the entropy, too, but also the enthalpy of a crystal. Frenkel defects are particularly found in structures with octahedral gaps. The concentration of both defects increases with increasing temperature.

Grain boundary

The conductivity across the grain boundary is usually inferior to the bulk conductivity for homogeneous interfaces. [76,93] Little is known about the diffusion across this interface besides that gaps should be prevented. Impurity phases usually form at grain boundaries and can deteriorate the conductivity, whereas in some cases they might improve it, as by the space charge or percolation effect. [93]

Percolation

An enhanced conductivity of a heterogenous interface can enhance the overall conductivity of a mixture of two components compared to the single materials. We call these type of materials dispersed ionic conductors. This phenomenon is caused by the formation of space charge layers, accumulation of dislocations or formation of new phases.[65] An
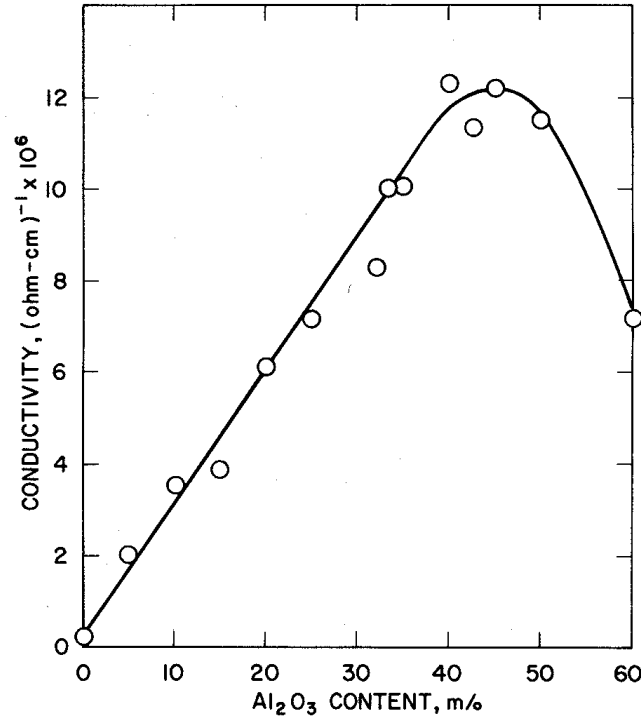

Figure 8 – Direct current conductivity of a LiI:Al$_2$O$_3$ system with varying ratio, taken from Liang.[110]

example is the mixture of LiI and Al$_2$O$_3$ by Liang.[110] This is illustrated in Fig. 8. The conductivity rises up to an Al$_2$O$_3$ content of 40%. This maximum is called percolation threshold. The low ionic conductivity of the insulating Al$_2$O$_3$ dominates after this point.

Amorphous materials

Amorphous materials can be seen as superior over crystalline materials in terms of ionic conduction by not having grain boundaries and a more open structure.[93] However, this applies only to sulfide-based materials. The maximum reported conductivity of oxide-based glasses is in the range of 10^{-6} S cm^{-1}. Li$_2$O-Nb$_2$O$_5$ and Li$_2$O-Ta$_2$O$_5$ and LiPON (Li$_{2.9}$PO$_{3.3}$N$_{0.46}$) are examples.[54]

Polymers

For ionic transport over long distances, migration of the cations from polymer chain to chain must be possible. It is also possible that the chain dynamics facilitate the hopping

of the ions between vacancies in a chain along the polymer helix. If the ionic conductivity of lithium is mainly governed by the characteristics of the polymer glass, the temperature dependence of the ionic conductivity σ in polymer electrolytes can be described by the Vogel-Tamman-Fulcher (VTF) equation 23.[46,171,183] It was originally used to describe the viscosity of glasses. In the form below, it can be applied to the conductivity.[26,56]

$$\sigma(T) = \sigma_0 \cdot \exp\left(\frac{-E_\mathrm{A}}{R \cdot (T - T_\mathrm{V})}\right) \tag{23}$$

T_V is the Vogel temperature and can be estimated 50 K below the glass transition temperature in polymer electrolytes.[17,57,182] The glass transition temperature of polyethylene oxide with $M_v = 10^6$ is 65 °C, as specified by the manufacturer Sigma Aldrich.

The nature of ion transport in polymers is different from that in solids. Fig. 9 shows four mechanisms of ion transport in polymers. To observe the actual transference of Li ions
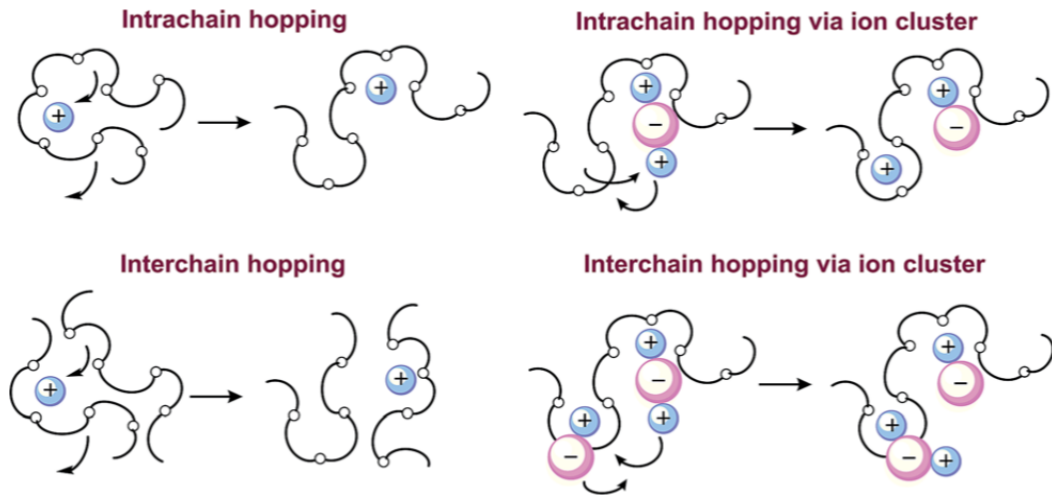

Figure 9 – Ion diffusion in polymers, taken from Xue et al.[195].

separated from other charge transfers such as the anions, we evaluate the conductivity of polymers based on the transference number.[31,41] A high mobility of anions is considered to have an enhancing effect on the Li mobility.[62]

Polymer composites

Fig. 10 illustrates how ceramic fillers can improve ionic conductivity within a polymer composite. Promoted ion-pair dissociation increases the number of ions able to participate in conduction. Here, acidic surfaces tend to attract anions and basic surfaces attract cations.[18,207] The surface of the ceramic can act as a Lewis acid or base and thereby provide additional sites for ion migration. This has been observed by Mellander et al. for Al_2O_3 particles in a PEO-LiTFSI matrix.[79] In case of strong interactions like ZrO_2, this effect can reduce the ionic mobility.[19] The particle surface could also link with the

polymer chains, changing its structure in order to create pathways for Li$^+$ transport (Fig. 10 d)).[18,19,21]
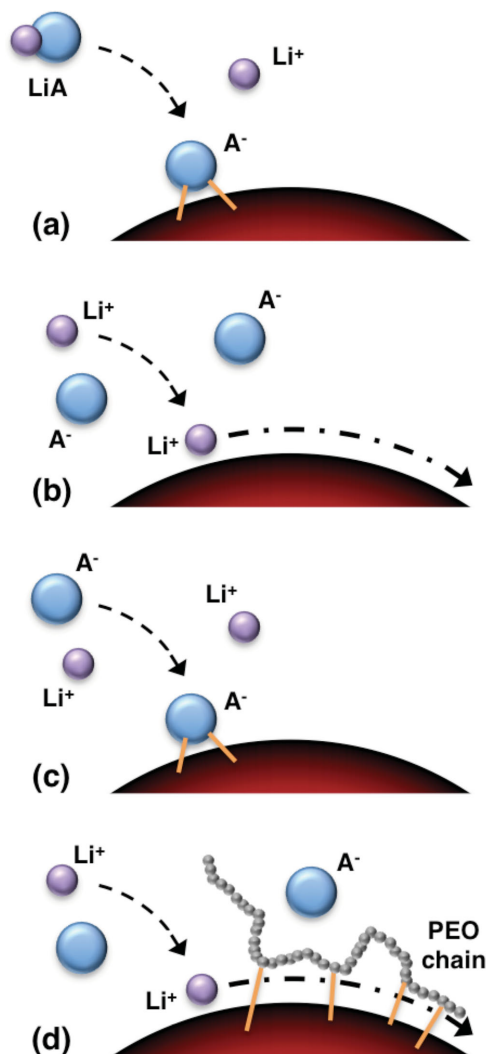

Figure 10 – Schematic of the active ion transport mechanisms in polymer nanocomposites. a) Ion pair dissociation, b) surface transport, c) anion attraction, and d) PEO chain promoted surface transport, taken from Srivastava et al.[161].

3. Current state of research

3.1. Solid state electrolytes

There are some material classes known today as candidates for solid state electrolytes that certainly are in competition with one another or, depending on price and performance, will occupy their respective niches. Much research has been done in the field of structural characterization of crystalline and amorphous materials. Still, new discoveries are published, especially through substitutions that improve ionic conductivity by several orders of magnitude.[45,60] Due to the further development of characterization methods like total scattering, amorphous structures can now also be examined. The recent elucidation of the structure of LiPON is an example.[103] This material is also exemplary for the dynamics in this field, as nowadays, due to its low conductivity, is not handled as a promising candidate anymore.

An important task in the field of solid electrolytes is the monitoring of the synthesis with the aim of upscaling while adhering to the material specifications. If no further optimization of the pure material is possible, the advantages of different materials can be combined by using composites. This is particularly useful with ceramic-polymer composites, as they can already be found on the market.

The compatibility of the solid electrolyte with the two electrodes must be considered, too. Here, research is moving in the direction of coatings, sintering additives, clarification of intermediate layers and contacting. Concerning the negative electrode, the goal is to use an "in-situ" anode.[98,138] Metallic lithium is deposited solely from the lithium contained in the cathode. Hereby, a specific capacity of 3860 mAh g^{-1} and a reduction potential of -3.04 V vs SHE is reached, in substitution of the traditional graphite. The solid electrolyte should be used as the thinnest possible separator. Due to lack of wetting with the liquid electrolyte, access to the active material for lithium ions must be guaranteed at the cathode. This should be achieved through intensive mixing of the active material with the solid electrolyte and other components to form a catholyte. These further additives can be sintering additives, conductivity additives or binders.

Fig. 11 illustrates the ongoing approaches in research about all-solid-state batteries (ASSB). The solid electrolyte simultaneously takes the function of the separator, so that this is not required as an extra component. The advantages of the solid electrolyte over the liquid are increased safety, no issues of leakages of toxic organic liquids, low flammability, non-volatility, mechanical and thermal stability, easy processability, low self-discharge, theoretically higher achievable power density and cyclability.[78]

Despite the promising advantages there are still some limitations that are hindering the transition of SSEs from academic research to large-scale production. However many car
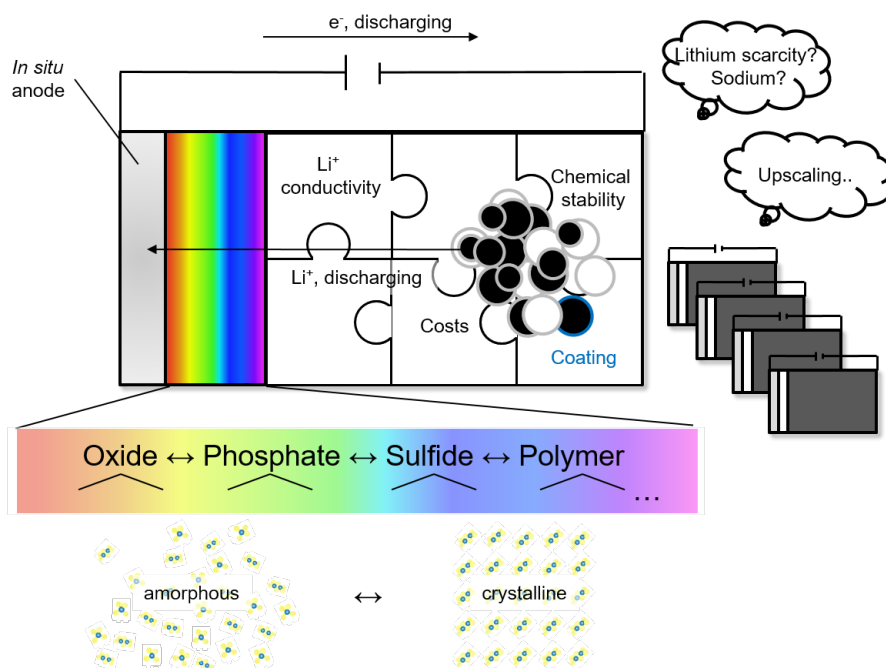
23

Figure 11 – Working principle and current challenges in all-solid-state battery development.

manufacturer (Toyota, BMW, Honda, Hyundai) expect to integrate these systems into viable devices and to commercialize solid-state battery-based electric vehicles by 2025. [89]

3.1.1. Sodium vs. lithium

From a purely economic point of view, one cannot speak of a shortage of lithium, although its price has increased. The problem with lithium-based battery technologies is rather cobalt. [174] The discussion about sodium-ion batteries should be preceded by the emphasis that science and research do not necessarily have to be subject to an economic purpose. It is therefore fundamentally important to develop new technological approaches, although it cannot be assumed that sodium-ion batteries will be used in portable devices in the near future. [126,131]

From a chemical perspective, one major issue about sodium-ion batteries is that sodium cannot intercalate graphite and neither is silicon an option. Some often referred to materials for sodium negative electrodes are hard carbon, Sb_2O_3, SnSb alloys and $Na_2Ti_3O_7$ for the positive electrode and $NaFePO_4$. [126,133–135]

3.1.2. History

The first inorganic ionic conductors were discovered by Faraday in the nineteenth century, the silver sulfide (Ag_2S) and lead(II) fluoride (PbF_2) The first polymeric material able to conduct ions in solid-state was PEO, discovered in the 1970s by Wright. [192]

Nowadays, the most promising candidates as solid state electrolytes for Li-ion batteries

are β-Li$_3$PS$_4$ as well as its amorphous pendant 75Li$_2$S-25P$_2$S$_5$, Li$_{10}$GeP$_2$S$_{12}$, Li$_6$PS$_5$Cl, Li$_{1.3}$Al$_{0.3}$Ti$_{1.7}$(PO$_4$)$_3$, and LLZO as well as composites of PEO-LiTFSI and LLZO.[138] The family of solid electrolytes comprises oxidic, sulfide- and polymer-derived materials. Each material class has its own characteristics which will be presented in the following chapters. An overview is presented in Fig. 12.
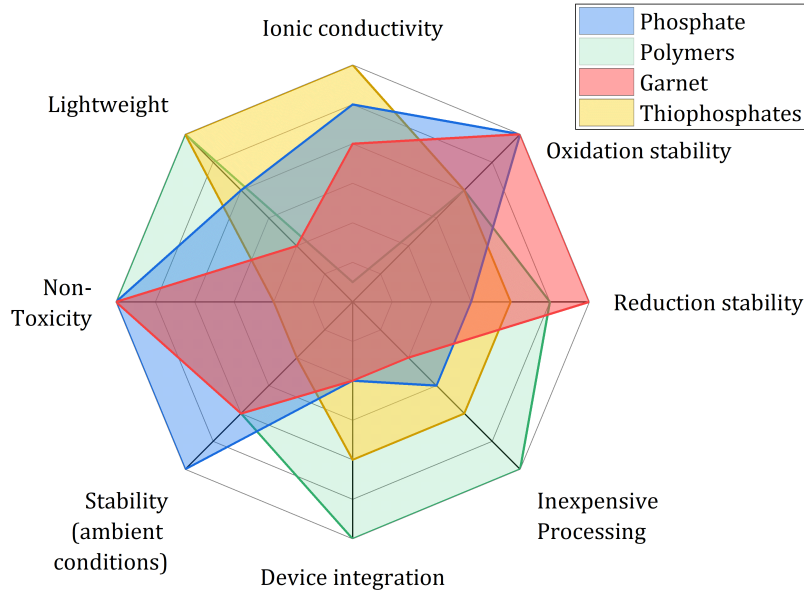

Figure 12 – Performance and characteristics of different electrolyte materials.

3.1.3. Thiophosphates

Thiophosphates started to gain interest in 1980, when it was discovered that the replacement of oxygen by sulfur has a strongly increasing effect on ionic conductivity.[116,139] Both amorphous and crystalline materials are known for thiophosphates. They captivate through their high ionic conductivity. This can be explained by the high polarizability of the sulfurous atoms[96] and also on the rotation of the PS$_4^{3-}$ tetrahedra; the "paddle-wheel" effect.[159] Another benefit is their possibility of chemical modification through different elements and different structural building blocks. Through their mechanical softness the grain boundary resistance is low and the electrolyte can be "cold-sintered". However, they are sensitive to moisture and the high toxicity and olfactory perception of H$_2$S represent an obstacle for market entry. H$_2$S forms when thiophosphates react with water. Another drawback is their limited stability against higher or lower voltages. They are considered to be stable from 1.7 to 3.0 V versus Li/Li$^+$ before S^0/S^{2-} or P^{5+}/P^{3-} reactions happen and form passivating layers.[20,91] This implies the use of a coating of both, the positive and the negative electrode.

Their structure can be chemically modified by aliovalent substitution in order to open

up the structure and bottlenecks for the lithium diffusion. Another benefit from the aliovalent substitution is generating disorder, which has been proven to be beneficial for the conductivity. The substitution of S by Cl, Br, I or Se are an example.[96,151] The incorporation of Se into the structure of $Li_6PS_{5-x}Se_xI$ is proven by XRD. $Li_6PS_{5-x}Se_xI$ $x=5$ has a two orders of magnitude higher conductivity than x=0.[151]

3.1.4. Oxides

Oxidic ceramics are non-toxic and from an electrochemical perspective highly stable materials against both high and low potentials. For a long time it was believed that the hardness of the oxides was an obstacle for lithium dendrites. Today we know that dendrites are mainly formed on microcracks. Hardness has turned to an obstacle for processing. In order to achieve the high conductivity levels described in the literature, extreme compression of the material is required. This drives up process costs and mechanical flexibility is no longer given. The use of lanthanum is also a cost factor. LLZO forms a passivating carbonate layer.

LATP has an advantage over LLZO through its higher conductivity, cheaper starting materials and stability in air. It does not form a passivating layer. A major issue is the reduction of titanium at the negative electrode. The replacement of titanium with iron and scandium is currently being examined.

Due to their high electrochemical stability, the use of oxides is also conceivable as a coating material for the positive or negative electrode with the use of another electrolyte as separator.

3.1.5. Polymers

In terms of device integration, polymer electrolytes score with their low weight, thin layer thickness and processability. By using different monomers, architectures and chain lengths, they offer a variety of possibilities for chemical tuning. To date, unfortunately, no polymer has been found that has comparable conductivities with thiophosphates or oxides. PEO is a standard material that is usually used together with LiTFSi or $LiClO_4$. There are also promising fluorinated polysulfonamides.[13]

Since LiTFSi is hygroscopic, the electrolyte cannot be regarded as stable in ambient conditions.

3.2. Structure of sulfidic electrolytes for sodium-ion batteries

Different P-S building blocks that are known from crystalline and amorphous lithium and sodium containing thiophosphates with P in oxidation state 5+ are: ortho-$[PS_4]^{3-}$,

pyro-$[P_2S_7]^{4-}$, and meta-$[P_2S_6]^{2-}$, see Fig. 13. Additionally, a hypo-$[P_2S_6]^{4-}$ unit exists with P in 4+ state. Unlike the corresponding crystalline material and the stoichiometry might suggest, a variety of these polyhedra can be present in the amorphous glasses. $[P_2S_6]^{4-}$ has been identified in a total scattering study of a lithium thiophosphate with a molar sulphide content of 75% instead of 50%, i.e. amorphous Li_3PS_4, which was also synthesized via ball milling.[165] Raman and ^{31}P MAS NMR measurements indicated the presence of P-P linked $[P_2S_6]^{4-}$ in amorphous $Li_7P_3S_{11}$ and $Li_4P_2S_7$.[28] The most common P-S units are depicted in Fig. 13. Zeier et al. found P-P linked "ethane-like" units
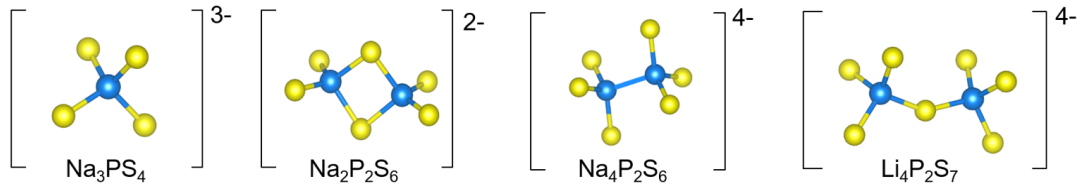
Figure 13 – Structural building blocks of crystalline thiophosphates.

surrounded by isolated $[PS_4]^{3-}$ tetrahedra in glassy $Li_4P_2S_6$ and isolated tetrahedra as glassy impurities in crystalline $Li_4P_2S_6$.[27] Less common ring or isobutane-like structures of P-S anions built from PS^{3-} building blocks have been observed with Raman and NMR spectroscopy as reported by Zeier et al.[53] Furthermore, Ohara et al. were able to demonstrate with differential pair distribution function (d-PDF) analysis that during crystallization of Li_3PS_4 from 75:25 $Li_2S:P_2S_5$ glass, the microstructure of the remaining glass phase did not change.[158]

Zeier et al. present Sb and W-substituted Na_3PS_4 $Na_{2.9}Sb_{0.9}W_{0.1}S_4$ with a ionic conductivity of 41 mS cm^{-1}.[45] Selenium substitution in Na_3PS_4 does not significantly improve the conductivity.[99] Both crystallize either cubic in the $I\bar{4}3m$ or tetragonal in the $P\bar{4}2_1c$ space group. The difference of the tetragonal structure from the cubic is a rotation of the PS_4^{3-} tetrahedra around the [111] direction.

Substituting P by As is also beneficial for the conductivity as presented by Shang et al. and Liu et al.[155,198] $Na_{11}Sn_2PS_{12}$ and $Na_{11.3}Sn_{2.1}P_{0.9}Se_{12}$ have the highest reported ionic conductivity of 3.0 and 3.7 mS cm^{-1}.[33] It is synthesized from the elements and crystallizes in space group $I4_1/acd$.

Chemical Reaction

Compared to the structural characterization of the amorphous and crystalline structures, the actual chemical reaction is not so often addressed. It should not be overlooked that the S^{2-} cation from Na_2S is binding to P_2S_5. Through the rearrangement of a pair of electrons, the adamantane structure of the P_4S_{10} results in two P_2S_5 molecules as
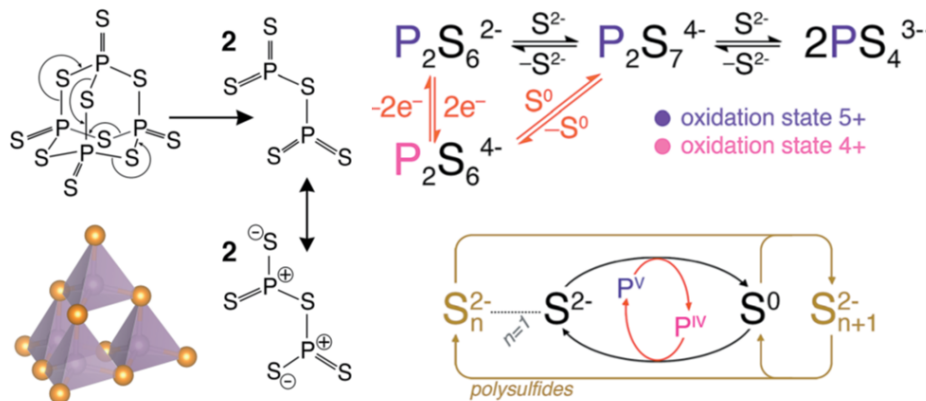
Figure 14 – Chemical reaction of P_4S_{10} forming thiophosphates, taken from [53].

illustrated by Ghidiu et al. illustrated in Fig. 14.[53] The two phosphorus atoms carry positive partial charges to which the sulfide anions can nucleophilically attack to form two corner-shared $[P_2S_7]^{4-}$ tetrahedra or single $[PS_4]^{3-}$ tetrahedra. An intramolecular nucleophile attack leads to the formation of two edge-shared $[P_2S_6]^{2-}$ tetrahedra.

3.3. Lithium Lanthanum Zirconium Oxide

3.3.1. Garnet crystal

The garnet group is a group of minerals affiliated to nesosilicates with the general formula $X_3Y_2(ZO_4)_3$. X is preferentially occupied with bi- and trivalent cations and is dodecahedrally coordinated. Y is octahedrally coordinated by oxygen and occupied by three- or fourvalent cations. Z is tetrahedrally coordinated and commonly occupied by fourvalent anions. The anion O^{2-} can be replaced with F^- or OH^-.

A characteristic feature of garnets is their high density and hardness. They are industrially applied as abrasives or used as gemstones. Garnets crystallize in space group $Ia\bar{3}d$, No. 230. The unit cell contains 8 formula units. Oxygen anions occupy the 96h position with point symmetry -1 and each oxygen anion is surrounded by 4 cations: two X, Y and Z. The Wyckoff position of the Z cation is 24d with point symmetry $\bar{4}$, that of Y is 16a, $\bar{3}$, and X is 24c, 222.

The ZO_4 tetrahedra and YO_6 octahedra are connected by shared oxygen atoms at their corners to form a framework of alternating tetrahedra and octahedra. Garnet are ortho silicates and their ZO_4 tetrahedra are not directly connected to each other. The XO_8 dodecahedra are linked by common edges to form rings of three, the plane of which is perpendicular to the spatial diagonal of the unit cell. These XO_8 dodecahedra rings are linked to one another to form a framework in which each dodecahedron belongs to two of such rings. The dodecahedra are edge-linked to the tetrahedra and octahedra of the ZO_4-YO_6 framework.

Unlike other high-density oxide structures, the oxygen ions do not form the closest packing. Large 8-fold coordinated ions would not find enough space in a cubic or hexagonal close packing. Due to the complex connection of all coordination polyhedra via common corners and many common edges, the garnet structure achieves its high density.

3.3.2. Substituents

In the formula $Li_7La_3Zr_2O_{12}$, LLZO crystallizes in a tetragonal system with a significantly lower ionic conductivity compared to the cubic crystal structure.[114] Earlier, an unintended doping of LLZO with Al occurred when using alumina crucibles for the ceramic synthesis. Today, MgO crucibles have replaced the alumina crucibles to avoid this unintentional doping.[80] A mechanism of the conversion from tetragonal, Al-free LLZO to cubic LLZO is presented by Hubaud et al. using ^{27}Al NMR. During heating, Li_5AlO_4 forms out of the Al precursor $Al(NO_3)_3$ which gets incorporated into the tetragonal garnet structure to form cubic LLZO.[72]

A stoichiometric aliovalent substitution of Li or Zr leads to a controlled and complete formation of the cubic LLZO phase. Many studies were carried out to optimize stoichiometry in terms of ionic conductivity with various substituents like Al[169,185], Ga[143], Nb[47], Ta[15], and W[108]. These substituents lead to the highest ionic conductivities among many other tested substituents. The mentioned cations and their preferred coordination in binary oxides are listed in Tab. 2.

3.3.3. Lithium sites and local hopping

From a structural perspective, lithium occupies the Z position in the lithium lanthanum zirconium garnet $X_3Y_2(ZO_4)_3$. Even, when using advanced techniques like neutron diffraction, locating Li in the garnet structure remains challenging.[95] When the Li ions occupy both neighboring octahedral and tetrahedral sites, the Coulomb repulsion among the Li-ions displaces the Li-ion in the octahedral site from the 48g position to the 96h position.[123] This displacement causes high ionic conductivity. The ionic conducdtivity is supposed to increase with Li occupancy in 48g/96h sites.[59,140,189]

^7Li NMR indicates that Li atoms, though appearing to be delocalized, spend most of their time at the tetrahedrally coordinated 24d site.

Figure 16 depicts the lithium localization in the crystal structure as analyzed by maximum entropy method and bond valence sum by Wagner et al.[186]. Several crystal chemical properties appear to promote the high Li ion conductivity in cubic LLZO. First, isotropic, threedimensioal Li-diffusion pathways, second, closely spaced lithium sites, and Li delocalization that allows for easy and fast lithium diffusion and third, low occupancies at the Li sites, which may also be enhanced by the heterovalent substitution

Table 2. – Substituting and substituted cations for aliovalent substitution in LLZO: Ionic radii[9] (all values given in Å) and coordination in binary oxides, cn = coordination number.

Ion	Tetrahedral (IV) based on halides	Octahedral (VI) based on halides	Coordination in binary oxide
Li^+	0.59	0.76	-
Al^{3+}	0.39 (V: 0.48)	0.535	Corundum: octahedral[145]
Fe^{3+}	0.49	Low spin: 0.55 High spin: 0.645	Octahedral
Ga^{3+}	0.47	0.62	Octahedral
Zr^{4+}	0.59	0.72	25°C: Baddeleyite, cn=7 >1100°C cn=8[145]
Nb^{5+}	0.48	0.64	NbO: Nb_6-Clusters[145] Nb_2O_5: distorted octahedra[51]
Ta^{5+}	-	0.64	Ta_2O_5 cn=7[163]/ cn=6 distorted octahedra[24]
W^{6+}	0.42	0.6	Octahedral in WO_3[145]
La^{3+}	VI: 1.032 XII: 1.36		Octahedral with one additional, O atom, cn= 7[191]

of Li by small cations like Al.

Local lithium diffusion is examined by Wagner et al. by relaxation and motional line narrowing (MLN). Extreme line narrowing is reached at 273 K. The motional narrowing curve of Al-LLZO is slightly shifted to higher temperatures compared to Ga-LLZO. They measure an activation energy of 0.14 eV (T_1) and 0.41 eV ($T_{1\rho}$) for Ga-LLZO with ^{7}Li relaxation. The results are shown in Fig. 15.

3.3.4. Hydrogarnet

A structural analysis of this member of the LLZO familiy with the hydrogarnet crystal structure is first published by Wagner et al. in 2016 with a Gallium-substituted compound.[186] The different crystal structure is suspected to be caused by substitution with Gallium, leading to a higher ionic conductivity compared to Al-substituted LLZO. Robben at al. agree that the symmetry reduction is caused by Gallium.[147] In a later publication, Wagner et al. propose that the hydrogarnet structure is formed by ordering of Fe^{3+} onto the tetrahedral Li1 (12a) site.[187]

Fig. 16 presents a comparison between the two structures. The hydrogarnet structure crystallizes in the space group $I\bar{4}3d$ and has an additional Li position. The garnet
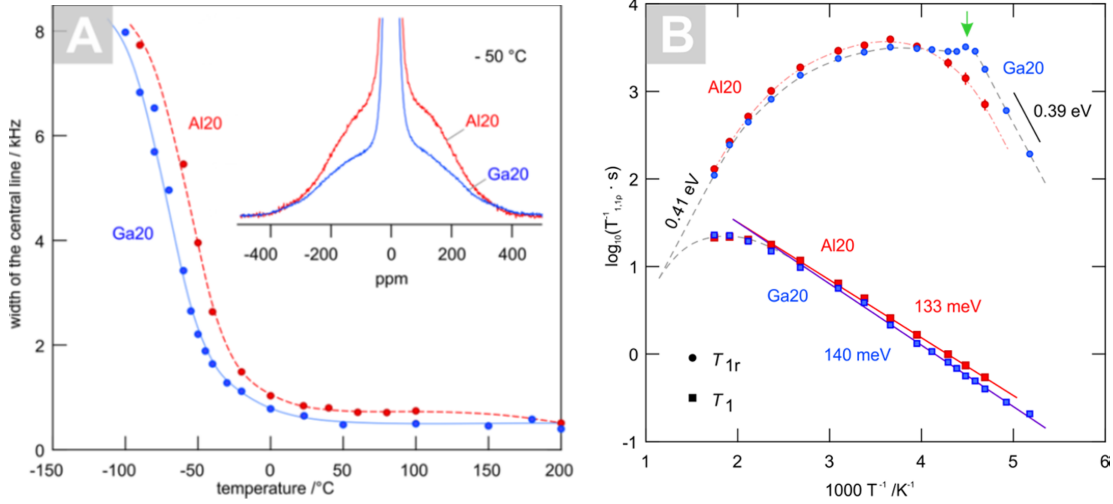
Figure 15 – A: Motional narrowing of the ^{7}Li NMR central line of Ga- and Al-substituted LLZO, and B: ^{7}Li relaxation rates, from Wagner et al.[186]

structure features two 96h Li positions that are very close. We can assume that only of these positions is occupied. In the hydrogarnet structure, the lithium positions have a larger distance to each other.

To the best of my knowledge, the formation of the hydrogarnet structure has not been reported for LLZO substituted with Al^{3+}, Nb^{5+}, Ta^{5+} or W^{6+} so far.
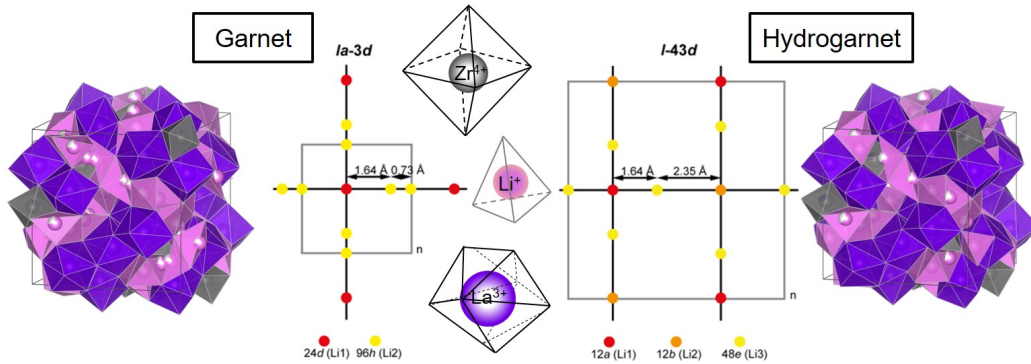
Figure 16 – Comparison of the crystal structures garnet and hydrogarnet, their cation coordination and Lithium Wyckoff positions. The projection of the Li-network is taken from Wagner et al.[186]

3.3.5. Frustration

Geometric frustration is a phenomenon in condensed matter physics in which the geometric properties of a crystal lattice or the presence of conflicting atomic forces prevent the simultaneous minimization of all interaction energies at a given lattice point. This can lead to extremely degenerated ground states.

Frustration is often considered as favoring ionic conductivity[25,34], although the reasons are not fully understood.[94] The difference in the crystal structure of garnet and hy-

drogarnet LLZO possibly originates from a deformation of the La sublattice and thus a geometric frustration.[94] It is assumed, that a maximum of sublattice entropy in garnet-type structures could have an enhancing effect on the Li^+ conductivity.[25,64,94,95] Loss of symmetry due to modified multiplicities of the tetrahedral and octahedral sites and the resulting subgroups of the garnet structure are explained by Kozinsky, without giving specific examples.[94] Düvel et al. identify free volume and aliovalent substitution with lower valence as cause for frustration.[34] Substitution with higher valence cations however can lead to a higher local mobility of ions.[3]

3.3.6. Impedance spectrocopy

The "left" semicircle (higher frequencies) is considered to represent the total conductivity of the bulk phase. It can be seen in literature that the formation of distinct semicircles can be suppressed either by an "atmospheric attack" or because the excitation frequencies of the electrical components are too similar as presented in Fig. 17. Using Li electrodes
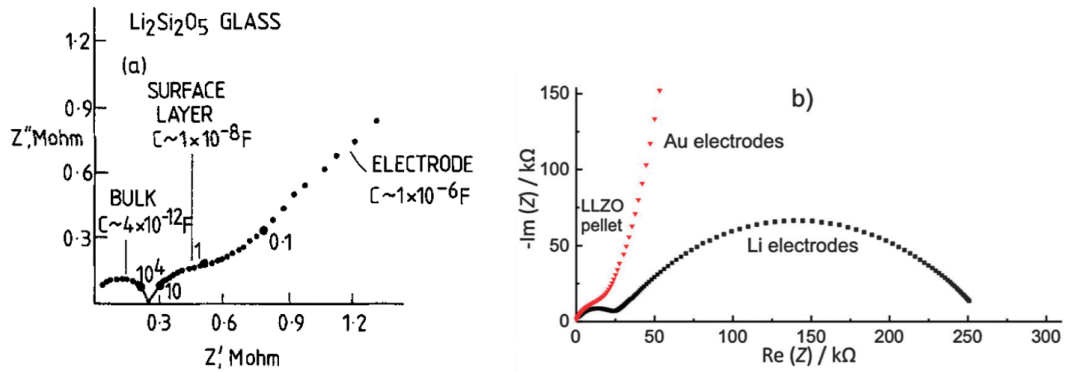
Figure 17 – a) Different contributions to impedance spectrum at 130 °C, blocking electrodes (steel) presence of a surface layer caused by "atmospheric attack" , schematically; from West, Irvine et al.[76], b) Impedance spectrum of LLZO pellet at room temperature with Au and Li contact; from Janek et al.[16]

one can observe a current in phase leading to an intersection with the x-axis at lower frequencies (Fig. 17 b)). Typical conductivities and calcining conditions are listed in Tab. 3.

3.3.7. H^+/Li^+ exchange

A Li^+ / H^+ exchange in LLZO was first described by Nyman et al.[128] It is supposed to happen in the LLZO when it is exposed to moisture. The exchange can be forced by stirring LLZO in a low pH medium, such as benzoic or acetic acid.[48,50,128] The observation of splitted reflections in a diffractogram and an enlargement of the unit cell

Table 3. – Comparison of bulk ionic conductivities for Al^{3+}-, Nb^{5+}, Ta^{5+}, W^{6+}-substituted LLZO synthesized from Li_2CO_3, La_2O_3, ZrO_2, Nb_2O_5, Ta_2O_5, WO_3 and Al_2O_3.

Stoichiometry	Calcination steps	Conductivity / bulk / S cm^{-1}	Ref.
1 wt-% Al as Al_2O_3 between 2. and 3. calcination	1. 900 °C, 5h 2. 950 °C, 12h 3. 1180 °C, 36h	$4.4 \cdot 10^{-4}$, 25 °C	[169,185]
$Li_{6.5}La_3Zr_{1.5}Nb_{0.5}O_{12}$	1. 900 °C, 8h 2. 1230 °C, 15h	$6.6 \cdot 10^{-4}$ 21 °C	[47]
$Li_{6.675}La_3Zr_{1.625}Ta_{0.375}O_{12}$ starting from LiOH	1. 950 °C, 12h 2. 1000 °C, 12h 3. 1000 °C, 12h	$5.0 \cdot 10^{-4}$, 25 °C	[15]
$Li_{6.3}La_3Zr_{1.65}W_{0.35}O_{12}$	1. 900 °C, 12h 2. 1200 °C, 12h	$8.0 \cdot 10^{-4}$, 25 °C	[108]

for $Li_7La_3Sn_2O_{12}$ is decribed by Galven et al.[48,49] An overview of tested garnet compositions against H^+/Li^+ exchange is listed in Le Berre et al.[48] Goodenough et. al. claim in an XPS study that the protons can be removed out of the crstal structure at 700 °C. However, no distinct Li_2CO_3 reflections are found in the diffraction pattern in this study.[107] The exchanged lithium is supposed to react with CO_2 to form Li_2CO_3 or water to form LiOH.

Zeier et al. also criticize the fact that in corresponding studies of Galven and Motoyama[48,49,122] no increased Li_2CO_3 or LiOH was observed in the diffraction patterns.[200] The incorporation of the proton in the crystal structure is not supposed to worsen the conductivity, which Galven and Le Berre et al. show with ^7Li relaxation.[48] Orera at al. suspect that H^+-exchange causes the transformation from garnet to hydrogarnet.[130]

3.4. Polymer composite electrolytes

The dependency of ionic conductivity in the two-phase system polymer-salt from low-salt to polymer-in-salt electrolyte (PISE) is depicted in Fig. 18 from Forsyth et al.[42] The example is chosen for Polytrimethylene carbonate (PTMC) but the principle of percolation is applicable to other polymers, too. Zaman et al. specify a maximum conductivity for a Al-LLZO- PEO composite with 15 Vol-% Al-LLZO due to a maximum surface area.[199] Lithium bis(trifluoromethanesulfonyl)imide (structure is shown in Fig. 18) and lithium perchlorate are commonly used salts in composite electrolytes. A drawback of the latter is its flammability. Polyethylene oxide is often preferred as polymer matrix among other polymers due to its capability as complexing agent. Polycarbonates, polyesters, polyni-
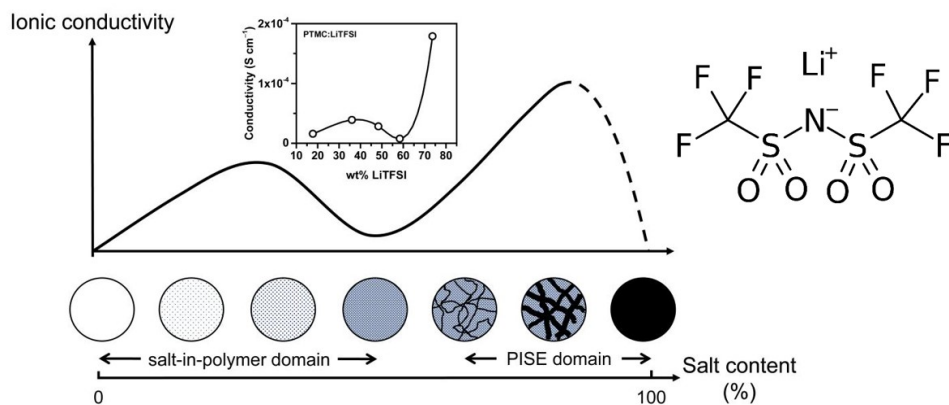
Figure 18 – Variation of the ionic conductivity (top) and suggested model for the morphology of polymer-in-salt electrolytes (bottom) as the salt concentration is increased from the low-salt (left) to the PISE concentration regime beyond the percolation threshold (right). Adapted from Forsyth et al.[42] Right: Structure of LiTFSI; from wikipedia article "Lithium bis(trifluoro-methanesulfonyl)imide", 18.11.2020

triles, polyalcohols and polyamines as alternatives should be mentioned.[119]

The question, how each component in a polymer-ceramic composite contributes to the conductivity is addressed by Li et al. by TEM measurements.[109] They could observe the formation of a space charge layer with a high lithium conductivity. The layer thickness approximately corresponds to the Debye length. Zheng et al. were able to demonstrate that about 20% of the Li ions are located in a disordered interface with ^{6}Li isotope exchange und neutron topography.[206]

Table 4 lists reported values of ionic conductivities of LLZO-polymer electrolytes. The chain length is an important characteristic of a polymer. It is therefore noticeable that the studies mainly use PEO with a uniform molecular weight of 10^6 g mol^{-1}. Yet, the fact that reported values of conductivity scatter between 10^{-4} S cm^{-1} [188,193,201] to 10^{-6} S cm^{-1} [85,157] at 25 °C shows the lack of understanding.

Recently, it was suspected that the long-range transport of lithium ions is hindered in the frustrated hydrogarnet structure which forms after harsh mechanical treatment of LLZO. However, sintering of hydrogarnet pellets ahead of impedance measurements transforms the structure back to garnet so they were not able to measure the long-range transport of lithium ions in the hydrogarnet structure.[44] The question how a difference in LLZO applies to the overall conductivity of the composite electrolyte is addressed by Keller and Gu.[85] They measured the ionic conductivity of 30 wt-% of P(EO)$_{15}$LiTFSI, 70 wt-% LLZO composite electrolytes with pristine and annealed LLZO and observed a slightly lower conductivity for the pristine LLZO. One could suspect that the diffraction pattern shows a reflection that could stem from the hydrogarnet structure as shown in Fig. 19.

Srivastava et al. report, that 10-15 wt-% of crystalline filler lead to an improved conductivity through prevention of the crystallization of PEO, the bulk conductivity of the

34

Table 4. – Reported ionic conductivities in LLZO-PEO ceramic-polymer composite electrolytes.

Composition	Conductivity / Activation energy	Ref.
PEO/Li+(LiTFSI) = 8, LLTZO 5-25 vol-% $Li_{6.4}La_3Zr_{1.4}Ta_{0.6}O_{12}$ PEO Mv = 10^6 g mol^{-1}	$2.1 \cdot 10^{-4}$ S · cm^{-1} at 30 °C	[201]
PEO/16 vol % Ga-LLZO $Li_{6.25}Ga_{0.25}La_3Zr_2O_{12}$ PEO M_v = 600 000 g mol^{-1}	$7.2 \cdot 10^{-5}$ S · cm^{-1} at 30 °C	[109]
30 wt% of P(EO)$_{15}$LiTFSI, 70 wt-% LLZO (1) Pristine LLZO (2) Annealed LLZO PEO M_v = 4 ·10^6 g mol^{-1}	(1) $5 \cdot 10^{-6}$ S · cm^{-1} (2) $8 \cdot 10^{-6}$ S · cm^{-1} 21°C	[85]
LLZO, PEO/Li= 16 PEO M_v = 600 000 g mol^{-1}	$2.39 \cdot 10^{-4}$ S · cm^{-1} at 25 °C	[188]
Al-LLZO, PEO M_v = 600 000 g mol^{-1}	$1.12 \cdot 10^{-4}$ S cm^{-1} 25°C	[193]
(1) Neat polymer electrolyte (2) LLZO + polymer (3) LLZO scaffold + polymer $Li_{6.25}Al_{0.25}La_3Zr_2O_{12}$, acrylic emulsion binder, ammonium polymethacrylate salt dispersant	$3.6 \cdot 10^{-6}$ S cm^{-1} $5.3 \cdot 10^{-6}$ S cm^{-1} $2.0 \cdot 10^{-5}$ S cm^{-1} at 25 °C	[157]
PEO, LiTFSI, LLZO	$0.5 \cdot 10^{-3}$ S cm^{-1} at 45°C, 0.65 eV	[176]

ceramic playing a subordinate role.[161] For SiO_2 and TiO_2 ceramics, enhancing effects on the ionic conductivity have been described.[86,113,172,197] Lian and Ketabi report the incorporation of SiO_2 or TiO_2 enhances the ionic conductivity by a factor of two by reducing the crystallinity of the polymer.
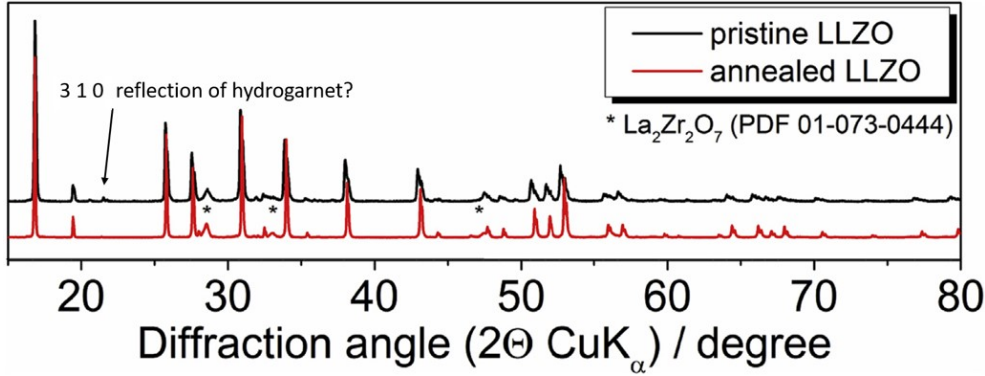
Figure 19 – X-ray patterns of pristine and annealed LLZO, modified from Keller et al. [85].

3.5. Lithium nickel manganese cobalt oxides as cathode active material in ASSB

Lithium nickel manganese cobalt oxides (NCM) are mixed oxides with a stochiometry of $LiNi_xCo_yMn_zO_2$ (x+y+z=1). Their structure derives from $LiCoO_2$ as a layered structure. Nowadays they are the most important cathode active material (CAM) for Li-ion batteries. Often used compositions are NCM111 ($LiNi_{0.33}Mn_{0.33}Co_{0.33}O_2$) and NCM622 ($LiNi_{0.6}Mn_{0.2}Co_{0.2}O_2$) or NCM811 ($LiNi_{0.8}Mn_{0.1}Co_{0.1}O_2$). Their synthesis is proceeded via coprecipitation and high-temperature lithiation reaction. [70,205] The lithium storage principle is the reversible oxidation of the transition metal oxides.

$$LiNi_xMn_yCo_{1-x-y}O_2 \longrightarrow Li_{1-k}Ni_xMn_yCo_{1-x-y}O_2 + k\ Li + k e^-,\ k{\leq}1 \qquad (24)$$

Charging voltage is limited to 4.2 V to prevent a decomposition of the cathode. Not all lithium can be extracted from the NCM. Using nickel and manganese brings a cost advantage over the expensive cobalt.

Wang and Randau give an overview of the latest reported electrochemical performances of solid batteries with LLZO electrolytes and NCM as CAM. [138,189] On average, Wang gives a C-rate of 0.1.

3.5.1. Interface of LLZO and NCM622

LLZO is reported to be thermodynamically unstable against NCM from theoretical calculations, but the reaction is kinetically hindered. [118,189] Liu et al. synthesized catholyte material based on Ta-doped LLZO and NCM111 with ball milling and subsequent co-sintering at 873 K and examined the morphology of the particles with TEM. [202] They observed the formation of core-shell particles with LLZO covering NCM particles as Sun et al. Co-sintering reduces the layer thickness of LLZO. [190] However, co-sintering introduces the formation of $La_2Zr_2O_7$ and $LaNiO_3$ which results in a poor cycling performance of the resulting material. Therefore, Liu et al. suggest further studies to improve the

coating layer. Goodenough et al. found that a thermally annealed (973 K) Al-doped LLZO-LiCoO$_2$ mixture forms tetragonal LLZO caused by cross-diffusion of Al, observed with TOF-SIMS.[132] Contradictory, Ohta et al. assembled a LLZO-NCM interface with PLD observing no chemical reactions or increased interface resistance which they determined to $5 \cdot 10^{-3}$ S cm^{-1}.[129] Goodenough et al. observed a decay of lithium ion conductivity at a LiCoO$_2$/LLZO interface.[132] They explained this with the migration of the dopant and the formation of tetragonal LLZO, but could not assign any clear peak splitting in the XRD pattern. Another aspect is the air sensitivity of LLZO, which easily reacts with CO$_2$ to form Li$_2$CO$_3$.

Zeier et al. observe an increasing impedance due to the formation of an interface layer and redox activities with an Li$_3$PS$_4$-NCM811 catholyte.[91] In their case the redox instability can be traced back to the thiophosphate electrolyte. This observation highlights the importance of these studies on the cathode-electrode interface.

3.5.2. Thermal stability

Tab. 5 lists previous studies about the temperature stability of cathode-solid electrolyte systems. This is important for the manufacturing of a battery that may include co-sintering of both components. High temperature studies are also suitable to address the formation of interfaces as very thin layers. Those may form at room temperature, but are to thin to be detected. The interfaces grow with rising temperature to crystalline domains that are detectable with XRD. Many studies agree on the formation of La$_2$Zr$_2$O$_7$ and Lanthanum Cobalt oxide although the reported temperatures spread from 773 to 973 K.[82,87,180,190]

3.6. Lithium Aluminum Titanium Phosphate

The Li$_{1.3}$Al$_{0.3}$Ti$_{1.7}$(PO$_4$)$_3$ (LATP) electrolyte is a Li-conductive ceramic with a NASICON-type structure. The NASICON structure was discovered in 1976 for Na$_{1+x}$Zr$_2$Si$_x$P$_{3-x}$O$_{12}$ by Hong and Goodenough.[55,68] It consists of a network of edge-sharing ZrO$_6$ octahedra and PO$_4$ tetrahedra. It gained interest due to its high ionic conductivity of 10^{-3} S cm^{-1}.[4,125] A small thermal expansion makes it useful for fabrication. A common route for preparation is via a Sol-Gel approach starting from Lithium acetate, AlNO$_3$, Titanium isopropoxide and phosphoric acid.[14,92]

Its crystal structure is trigonal with the space group $R\bar{3}c$ (No. 167).

Table 5. – Cathode-solid electrolyte composites and their thermal stability reported in literature, LCO: Lithium Cobalt oxide, n.s.: not specified, PLD: pulsed laser deposition, parts originate from Stöffler[164].

System: CAM + SE and processing	Temp. / K	Impurity phase formation	Atmosphere	Heating	Method	Ref.
LLZO + LCO, PLD 100 nm	937	La_2CoO_4	Air	2h	EDS, TEM	[87]
LLZO + LCO, PLD 150 nm	873	La_2CoO_4	Air	n.s.	HAADF-STEM, EDS	[82]
Nb-LLZO + LCO, PLD 500 nm	873	none	n.s.	n.s.	EDS	[129]
Al-LLZO + LCO, 20-500 nm RF-Sputtering	773	$La_2Zr_2O_7$, Li_2CO_3, $LaCoO_3$	Air	4 h	Synchrotron XRD XAS	[180]
LLZO + NCM (PLD)	973	Li_2CO_3, $La_2Zr_2O_7$	Air	4 h	XRD (Co K_α)	[90]
Al-LLZO + LCO, 4:1 (wt-%)	973	tetragonal LLZO	Air	1 h	XRD (Cu K_α)	[132]
Ta-LLZO + NCM111, mortared 1:1 (vol-%)	973	$LaCo_{1-x}Mn_xO_3$, $La(Mn, Ni)O_3$ LCO und NCM	Air	1 h, 10 h	Raman, XRD (Cu K_α)	[140]
Ta-LLZO + LCO, mortared 1:1 (vol-%)	1358	$LaCoO_3$	Air	2 h	XRD (Cu K_α)	[178]
NMC622 + Li_3BO_3 + Ta-LLZO, LLZO sintered pellet,	873	$La_2Zr_2O_7$, $LaNiO_3$ Ni diffuses into LLZO	Air	1h	XRD (Cu K_α), XAS	[190]
LLZO + NCM 1:1 (wt-%)	973	$LaMnO_3$	Vacuum	n.s.	Synchrotron XRD	[164]

4. Sulfidic sodium-based thiophosphate electrolytes: Structural elucidation of amorphous Na$_2$P$_2$S$_6$

The development of all-solid-state sodium-ion batteries as an alternative energy storage system to lithium based techniques demands for sodium conducting solid electrolytes and an understanding of the sodium conduction mechanism governed by the local structure of these glass-ceramic materials.

A promising class of solid electrolytes are thiophosphates and it was recently demonstrated that they can operate in full battery cells as electrolytes[173] or electrodes.[38,69] A use as electrocatalyst for water splitting is also intensely studied.[32,111] Despite these promising results, the reproducibility for the synthesis of amorphous materials remains challenging. One reason is the lack of understanding of structural peculiarities of these glasses. Therefore, detailed investigations of these materials are necessary. Without a full-scale understanding of the structural aspects the impact on ionic conductivity remains speculative.[37]

As a result, significant differences in the microstructure and conductivity of solid state electrolytes are observed.[8,127,165] Nevertheless, the use of amorphous materials could be seen as a future trend in further enhancing battery performance. Amorphous thiophosphates, compared to their crystalline analogues, are supposed to offer a better bulk conductivity because of a larger free volume for the conducting species and lower interfacial resistance.[37,203] It has recently been demonstrated that amorphous Li$_3$PS$_4$ shows a better performance than crystalline Li$_3$PS$_4$, that has been synthesized via subsequent crystallization of the amorphous Li$_3$PS$_4$.[165] Huang et al. proposed a high amount of disorder to be crucial for the high mobility of Na-ions in amorphous Na$_2$Si$_2$O$_5$.[106] However, in crystalline Li$_{10}$GeP$_2$S$_{12}$ Li conductivity is higher compared to (Li$_2$S)(Ge$_2$2)(P$_2$S$_5$) glass which can be attributed to a lower activation energy for diffusion along the Li-pathways in the crystal.[121] These contrary results emphasize the necessity for detailed investigations of solid state electrolytes.

4.1. Aim of the work

The structure of amorphous and crystalline Na$_2$P$_2$S$_6$ is investigated by means of X-ray diffraction (XRD), pair distribution function analysis (PDF), Raman spectroscopy and ^{23}Na and ^{31}P magic-angle spinning (MAS) nuclear magnetic resonance (NMR) spectroscopy.

Na$_2$P$_2$S$_6$ was synthesized in an amorphous state with subsequent crystallization. The change of the local structure before and after crystallization was analyzed in detail re-

garding the presence of structural building blocks such as $[P_2S_6]^{2-}$, $[P_2S_6]^{4-}$, $[P_2S_7]^{4-}$, and $[PS_4]^{3-}$. The structure of the crystalline phase differs markedly compared to the corresponding amorphous phase.

This chapter contains results of the published manuscript *Mechanochemical synthesis of amorphous and crystalline $Na_2P_2S_6$ – Elucidation of local structural changes by X-ray total scattering and NMR* by Fritsch et al.[43]

4.2. Glass formation: chemical reaction through P–S bond breaking in P_2S_5

The time-dependent evolution of crystalline phases within the milled sample of Na_2S and P_2S_5 was determined by XRD as shown in Fig. 20 a). The reflections of the two starting materials Na_2S and P_2S_5 are initially superimposed after 0.5 h and 2 h of ball milling. After 20 h, the reflections disappeared completely. No additional reflections could be observed during the whole process of ball milling. In contrast to the sodium ortho-thio-phosphate Na_3PS_4, $Na_2P_2S_6$ does not form a crystalline phase during ball milling.[63]

Based on Raman spectroscopy results the appearance of new modes depending on the milling time can be observed, indicating the formation of amorphous $Na_2P_2S_6$. After 1 h of milling, the Raman spectrum is still very similar to that of the starting substance P_2S_5 (Fig. 20 b)). At this time, we also still observe large crystalline fractions of the starting materials Na_2S and P_2S_5 in the diffraction patterns (Fig. 1). After 8 h and 20 h ball milling time, signals from P-S vibrational modes occur in the Raman spectra which we attribute to the formation of $Na_2P_2S_6$.

In a previous work about glassy $Na_2P_2S_6$ synthesized by melt-quenching, the vibration mode 421 cm^{-1} was assigned to ν_{ring} P-S-P-S from $[P_2S_6]^{2-}$ and 578 cm^{-1} to ν_{as} PS$_3$ from the $[P_2S_6]^{4-}$ building block.[11]

The synthesis route of amorphous sodium thiophosphates through ball milling has been established by Hayashi et al.[127] for stoichiometries with high Na_2S contents of x = 0.67, 0.70, 0.75 and 0.80 in $xNa_2S + (1-x)P_2S_5$. Surprisingly, no attempt was made to synthesize $Na_2P_2S_6$ in this study. Lotsch et al. described the synthesis of crystalline $Na_2P_2S_6$ starting from elements Na, P and S in vacuum-sealed silica glass tubes by heating at 1070 K for 10 h.[101]

4.3. Structure of crystalline $Na_2P_2S_6$

The structure of crystalline $Na_2P_2S_6$ was refined using the Rietveld method based on the crystal structure published in 2014 by Lotsch et al.,[101] ISCD no. 426906. The corresponding X-ray diffraction pattern is shown in Fig. 21. $Na_2P_2S_6$ crystallizes in the

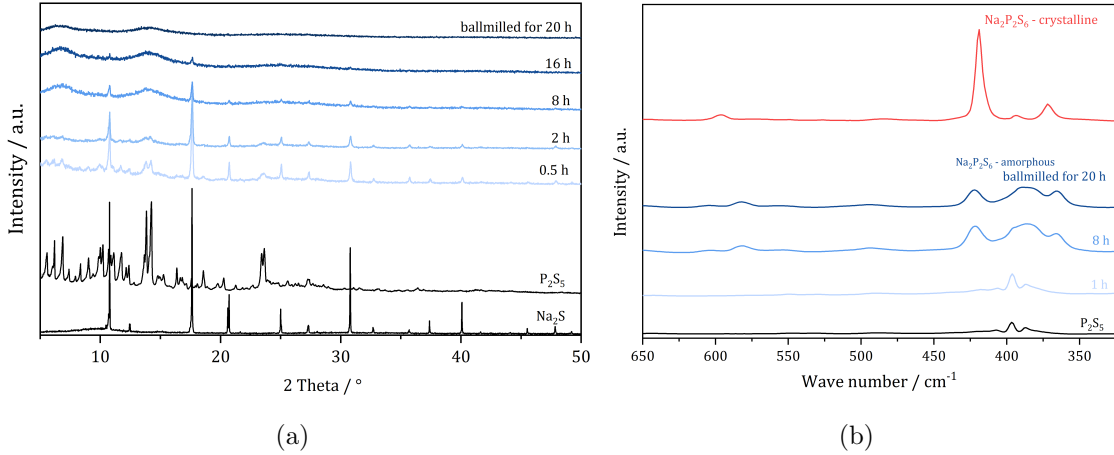**Figure 20** – a) Powder XRD patterns (Mo $K_{\alpha 1}$ radiation) of the binary starting materials Na_2S and P_2S_5, and of amorphous $Na_2P_2S_6$ after different milling times, b) Raman spectra of P_2S_5 and $Na_2P_2S_6$ after different milling times and after calcination.

monoclinic space group $P2_1/m$ (No. 11). The lattice parameters were refined to $a = 6.686(3)$ Å, $b = 7.831(4)$ Å, $c = 9.042(4)$ Åand $\beta = 90.22(4)°$. The results of Rietveld Refinement are given in Table 6. The main building blocks of this crystal structure are *meta*-thiophosphate anions, i.e. two edge-sharing PS_4 tetrahedra (depicted in Fig. 21). No reflections from impurity phases could be detected. The PDF based on total scattering data collected at the high energy beamline P02.1 (DESY) could be fitted well up to at least 50 Å(Fig. 4).[170] Nevertheless, some peculiarities were encountered during the fitting process. The low r part of the PDF, especially the peak around 3.4 Å, could not be fitted well, when the fitted region exceeded 20 Å, i.e. the intensity of the observed peak was higher than the one in the model. Most likely this is caused by a certain amount of local structural disorder, as often observed in structures built up by isolated polyhedral species. This peak belongs to S–S distances (detailed assignments are given in Fig. 24) of the edge-sharing tetrahedra. This disorder could be covered by using anisotropic displacement factors, but only up to 20 Å. When the short range (<5 Å) is omitted in the fitting the resulting displacement factors become more isotropic, supporting the assumption that the disorder is a local phenomenon, which is averaged out on the global scale. Both models are compared in Fig. 22. The results of both refined structure models based on XRD and PDF, respectively, were compared using the program *Compstru* provided by the Bilbao Crystallographic Server.[6,23]

The crystal structures coincide very well, indicated by a measure of similarity $\Delta = 0.016$, taking the lattice parameters and atomic coordinates into account.[9] The maximum deviation of atomic positions corresponding to the sodium ions yields a max. distance of 0.12 Å.

Table 6. – Refined structural parameters obtained from powder diffraction of crystalline $Na_2P_2S_6$ at room temperature compared to those of a single crystal measurement from Lotsch et al.[101]

	$Na_2P_2S_6$ synthesized by ball milling and annealing	$Na_2P_2S_6$ synthesized by solid state reaction
Space group	$P2_1/m$ (No. 11)	$P2_1/m$ (No. 11)
Lattice parameters		
a / Å	6.6861(3)	6.6752(3)
b / Å	7.8314 (4)	7.7968(4)
c / Å	9.0418 (4)	9.0379(4)
β / °	90.223 (4)	90.151(1)
Cell volume / Å^3	473.44 (4)	470.38(4)
Atomic coordinates Na		
x	0.2829 (0.0028)	0.2863(2)
y	0.0136 (0.0017)	0.01241(9)
z	0.7130 (0.0016)	0.71003(7)
Structural strain $dD/D\cdot 10^{-4}$	34.34 (0.12)	-
GOF	2.458	1.09
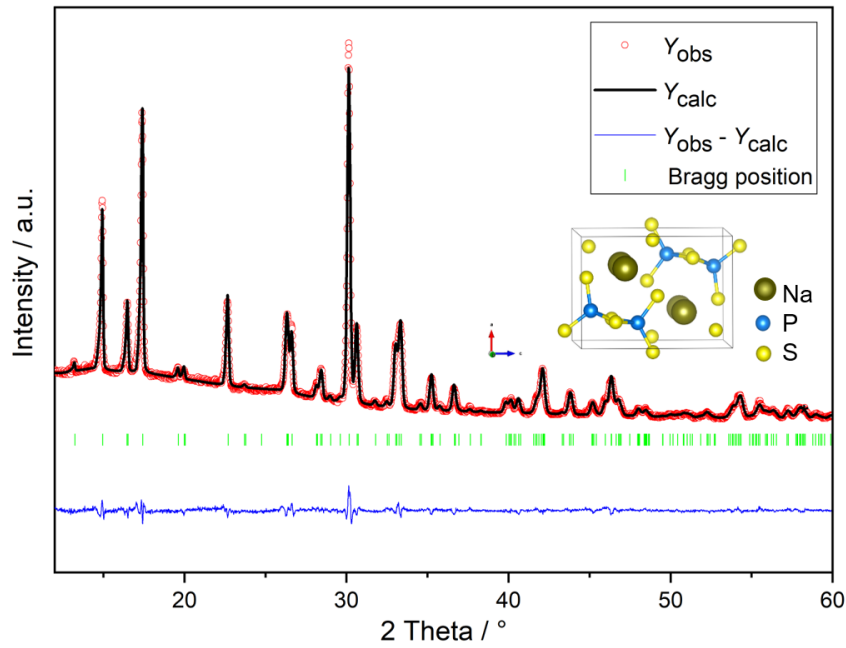
Figure 21 – Rietveld analysis of the powder diffraction pattern (Cu $K_{\alpha 1}$ radiation) of $Na_2P_2S_6$ and its crystal structure drawn with Vesta.[120]
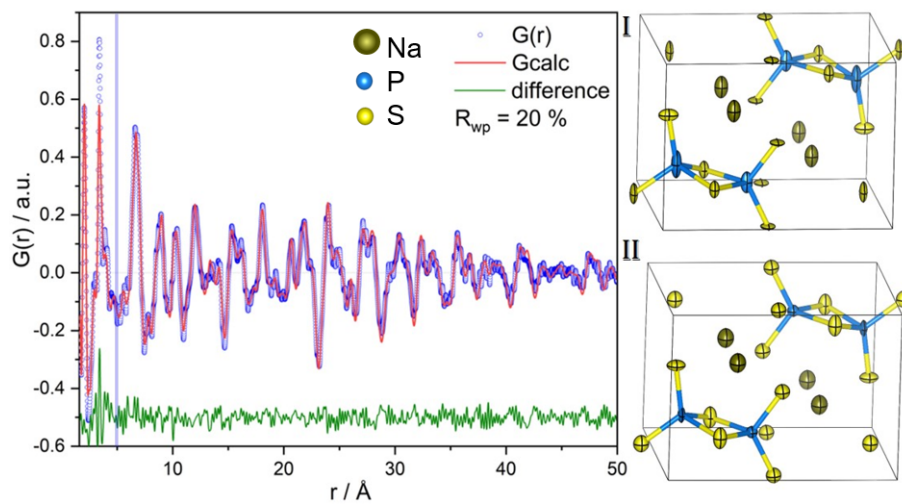
Figure 22 – Left: Real space Rietveld-like least squares fitting of a calculated PDF based on $Na_2P_2S_6$ structural models given on the right. I: Result of fitting the whole range in real space 1.7–50 Å; II: Resulting structural model, when short range (i.e. 1.7–5 Å) is not included in the fit. Atoms are displayed by anisotropic displacement ellipsoids (probability of 50%).

4.4. Structure of amorphous $Na_2P_2S_6$

Since glasses are X-ray amorphous, synchrotron total scattering measurements were performed to calculate the corresponding pair distribution functions (PDF).The normalized PDFs of the amorphous and crystalline sample are depicted in Fig. 23. No intensity can be observed in the PDF of the amorphous sample above 20 Å, indicating a fully random arrangement of the constituents. In the medium range 5-18 Å, the broad sinusoidal oscillation of the PDF, without distinct peaks, reveals that only a certain structural order, sometimes referred to as a kind of pre-ordering of the main building units, but no strong correlations are present. The nature of these units can be discussed by having a closer look on the short-range order given in Fig. 24, which indicates both, agreements and disagreements with the local structure of the crystalline phase. The distances being present in $meta - P_2S_6$ are included as a reference. The most obvious difference is the absence of sodium related peaks in the PDF of the amorphous sample, marked by red lines in Fig. 24. This indicates a high amount of sodium disorder within the glassy structure. Comparing the PDF of the amorphous sample with modeled PDFs of different thiophosphate anions, namely ortho-, meta-, pyro- and hypo-thiophosphate (Fig. 25), reveals the difficulty to unambiguously determine the anionic species. However, due to the increased intensity of only the first peak at 2.1 Å, which can be assigned to P-S bonds, it can be assumed, that a higher amount of single $[PS_4]^{3-}$ tetrahedra is present in the sample.
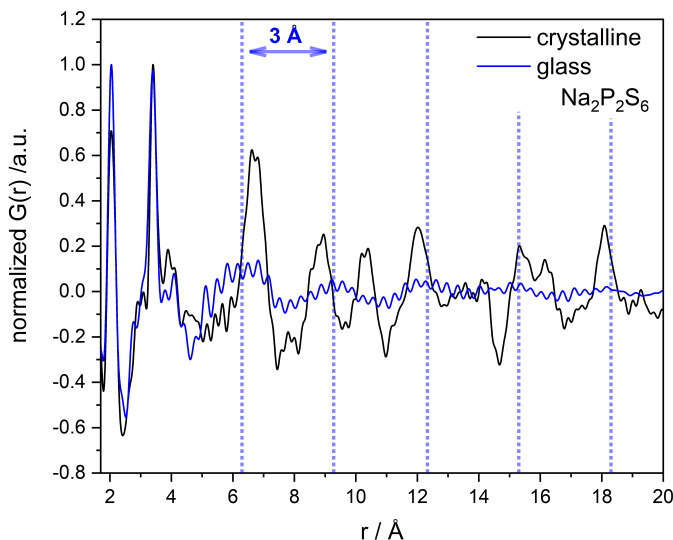
Figure 23 – Comparison of normalized PDF of amorphous (blue) and crystalline (black) $Na_2P_2S_6$. Dotted blue lines mark maxima of medium range modulations to emphasize the periodicity of 3 Å.
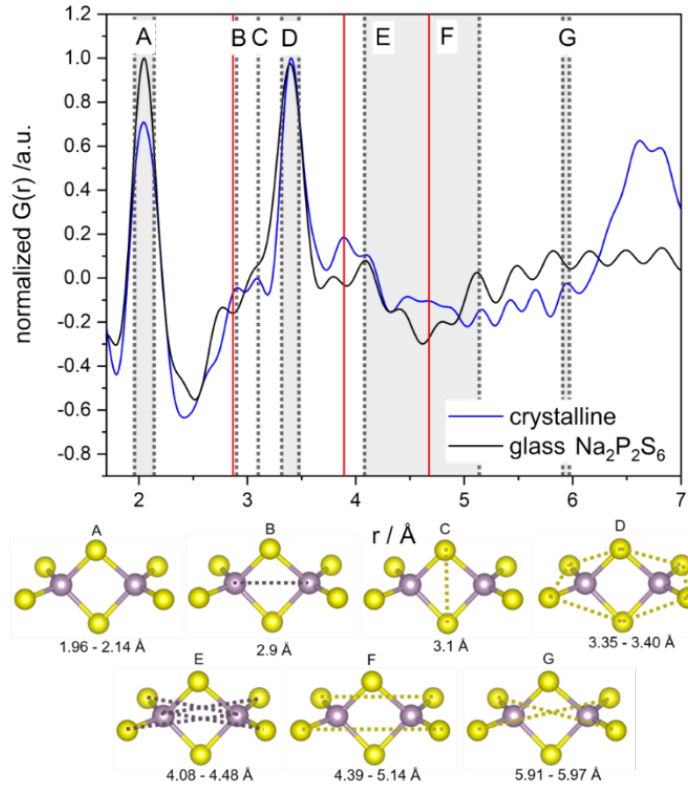
Figure 24 – Top: Comparison of short range of normalized PDF of amorphous (blue) and crystalline (black) $Na_2P_2S_6$. The corresponding distances based on literature reference $Na_2P_2S_6$ (ICSD 426906) are marked. Dotted grey lines correspond to distances occurring in metathiophosphate anion as depicted below. A represents P–S bond. Red lines correspond to sodium related distances, which are markedly less intense in the PDF of the amorphous material.

Furthermore, the presence of P-P linked $[P_2S_6]^{4-}$ can most likely be excluded. At 3.8 Å, a pronounced signal is calculated for $[P_2S_6]^{4-}$ that can be assigned to the Gauche conformation of sulfur atoms along the P-P axis. This signal cannot be observed in the PDF. Therefore, the presence of this unit is contradicted, in contrast to amorphous Li_3PS_4.[165]

With ^{23}Na and ^{31}P MAS NMR spectroscopy shown in Fig. 26, the changes in the local environment around sodium and phosphorus atoms are studied and compared with known chemical shifts of similar structures, enabling a distinction between the differently linked P-S tetrahedra. The signal at 86.5 ppm in the ^{31}P MAS NMR spectra of crystalline Na_3PS_4 is assigned to isolated $[PS_4]^{3-}$ tetrahedra, in agreement with the well-known structure of Na_3PS_4.[10,28] This peak is very sharp for crystalline Na_3PS_4, revealing highly uniform $[PS_4]^{3-}$ tetrahedra in this highly crystalline structure. The two peaks observed for crystalline $Na_2P_2S_6$ at 44.3 and 51.5 ppm can be assigned to the two different phosphorus positions in this crystal structure belonging to two edge-sharing tetrahedra of the structural building block $[P_2S_6]$.[38] Both phosphorus atoms occupy a

45
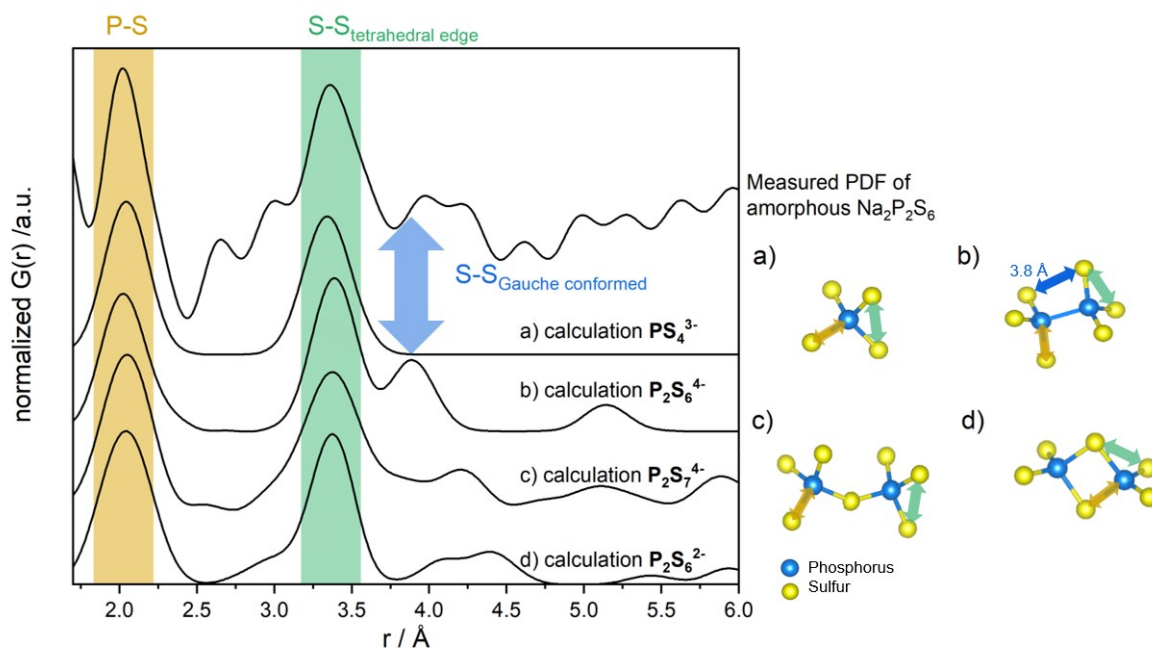
Figure 25 – Zoom into the short range region of the pair distribution functions of amorphous $Na_2P_2S_6$ compared with modeled PDFs of a) single $[PS_4]^{3-}$, b) $[P_2S_6]^{4-}$, c) $[P_2S_7]^{4-}$ and d) $[P_2S_6]^{2-}$ structural building blocks. Atomic distances are marked with yellow, green and blue arrows.

2e position but are not crystallographically equivalent which was determined from the crystal structure of the Rietveld refinement. The intensities of these two peaks are very similar when all spinning sidebands are used for integration. That is also in agreement with the structural information from Rietveld refinement: both P-atom positions are equally occupied.

The signal belonging to the isolated $[PS_4]^{3-}$ tetrahedra at 86.5 ppm is also observed for the amorphous $Na_2P_2S_6$ sample. Therefore, it is assumed that this sample contains single tetrahedra and no corner-sharing tetrahedra like in the crystalline structure, since the chemical shifts of ^{31}P in the amorphous sample are different from those in the crystalline sample. The large width of this peak reflects strong variations in the bond angles and thus a distribution of resonance frequencies for this amorphous structure. The signal at 130.0 ppm of the amorphous sample can be assigned to corner-sharing tetrahedra.[28]

4.5. Sodium disorder

The ^{23}Na MAS NMR spectra reveal a signal at -4.4 ppm for all samples. The same position of the signal indicates that the chemical environment of sodium in the three thiophosphates is very similar, maybe also caused by the high mobility of Na in these materials. Again, the very narrow signal observed for crystalline $Na_2P_2S_6$, with clear indications of quadrupolar powder lineshapes (nuclear spin $I(^{23}Na) = 3/2$), reveals a
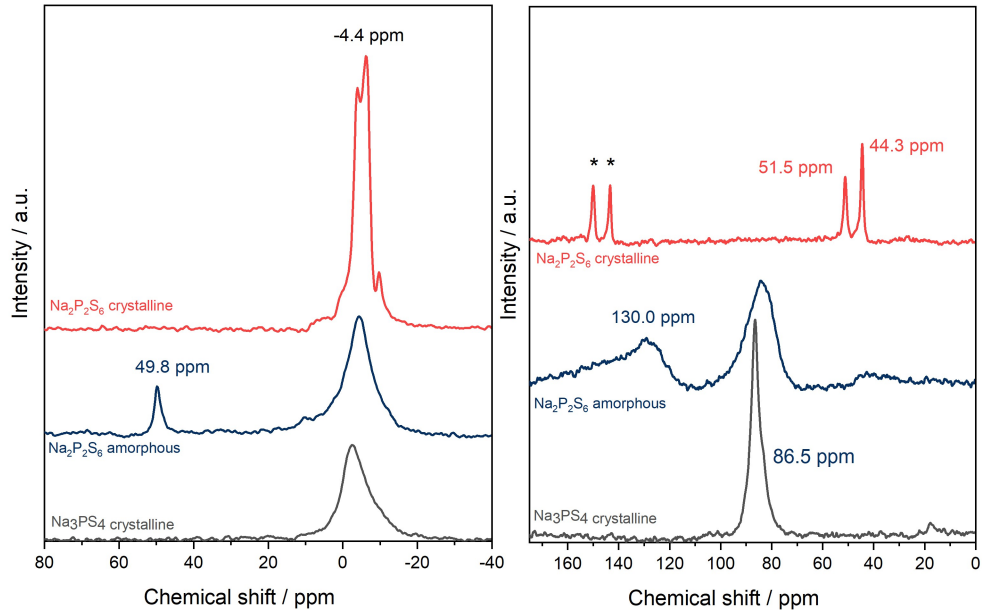
Figure 26 – Left: ^{23}Na and right: ^{31}P MAS NMR spectra of amorphous and crystalline $Na_2P_2S_6$ and Na_3PS_4. Spinning sidebands are marked with an asterisk.

well-defined local structure around Na in the well-crystalline sample while the broad peak observed for amorphous $Na_2P_2S_6$ is caused by local fluctuations in the environments around Na in the amorphous phase. The signal at 49.8 ppm in the amorphous $Na_2P_2S_6$ is assigned to a small amount of residual Na_2S educt.[100]

4.6. Ionic conductivity

A ionic conductivity of $5.7 \cdot 10^{-8}$ S cm^{-1} for amorphous $Na_2P_2S_6$ and $2.6 \cdot 10^{-11}$ S cm^{-1} for crystalline $Na_2P_2S_6$ is deduced from the Nyquist plot depicted in Fig. 27 at 25 °C. To the best of my knowledge, no ionic conductivity data is available in the literature on
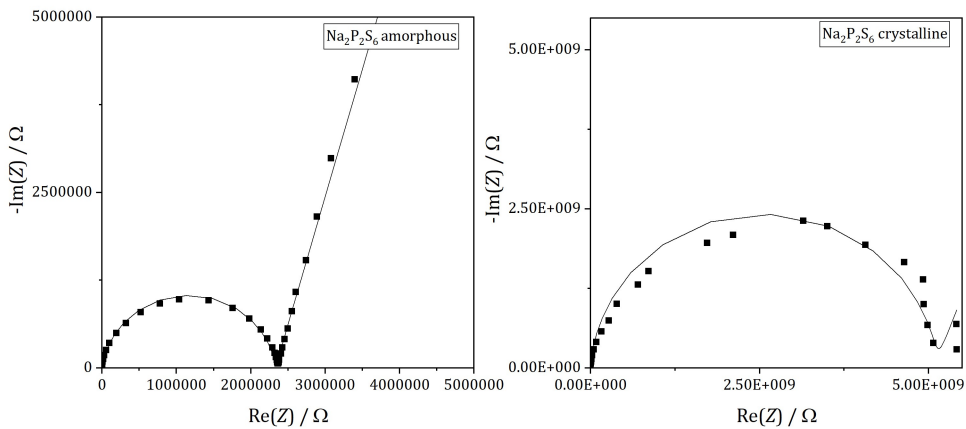
Figure 27 – Nyquist plot of electrical impedance measurement of amorphous and crystalline $Na_2P_2S_6$.

$Na_2P_2S_6$. Zeier et al. determined an ionic conductivity of $7.8 \cdot 10^{-11}$ S cm^{-1} for crystalline

$Li_2P_2S_6$ at room temperature.[29] The ionic conductivity of the amorphous $Na_2P_2S_6$ is significantly higher. The improved ionic conductivity of $Na_2P_2S_6$ can therefore possibly be attributed to a higher degree of disorder of the Na ions, as indicated by PDF results.

4.7. Morphology

Fig. 28 shows the particle morphology as measured with scanning electron microscopy (SEM). The surface of amorphous $Na_2P_2S_6$ appears smooth whereas that of crystalline $Na_2P_2S_6$ looks more edged. Defined crystallites can be recognized. A marginal effect of grain boundaries on the ionic conductivity can be suspected.

(a)   (b)

(c)   (d)
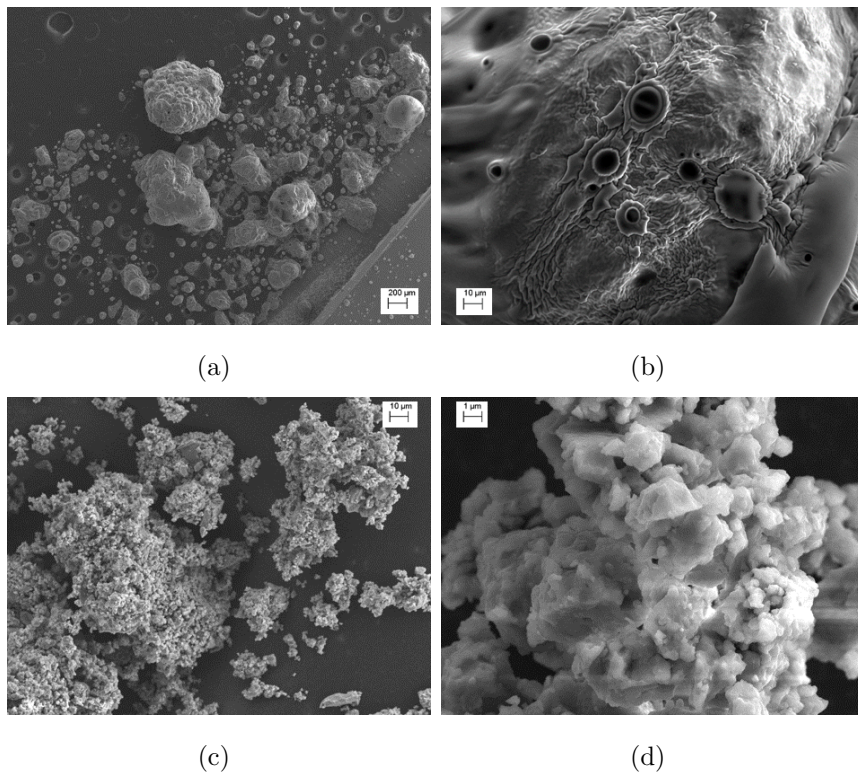
Figure 28 – SEM micrographs of a),b) amorphous and c), d) crystalline $Na_2P_2S_6$.

4.8. Structure of crystalline $Na_2P_2S_6$ after ball milling

The process of thermal crystallization can be reversed by ball milling as shown by the ^{31}P MAS NMR spectra in Fig. 29. Reflections of crystalline $Na_2P_2S_6$ vanish in the diffraction measurement after 8 minutes of ball milling. The reaction procedes in a way that single and corner-sharing tetrahedra are formed. The reversibility of this process can also be confirmed by PDF measurements. A high ionic conductivity of 9.3 $\cdot 10^{-8}$ S cm^{-1} comparable to that of amorphous $Na_2P_2S_6$ is obtained after ball milling, too. The corresponding impedance spectrum can be found in the appendix in Fig. 75.

These results are partially included in the master thesis of Adam Reupert[144] and the manuscript *Structural changes during synthesis of $Na_2P_2S_6$ and Na_3PS_4 and their influence on conductivity* by Adam Reupert, Charlotte Fritsch et al.
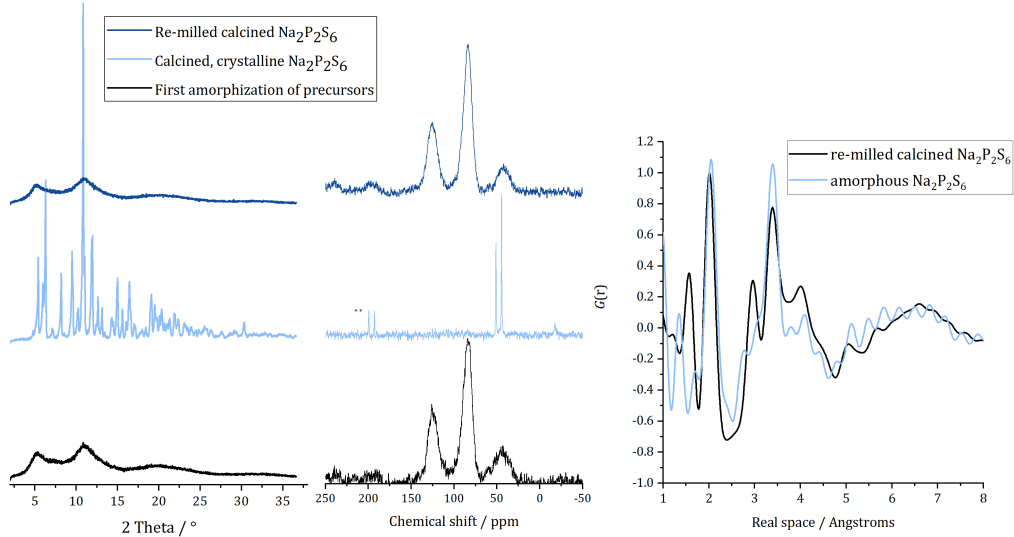

Figure 29 – Left: X-ray diffraction pattern (Ag $K_{\alpha 1}$), middle: ^{31}P MAS NMR spectra of amorphous, crystalline and remilled crystalline $Na_2P_2S_6$. Spinning sidebands are marked with an asterisk. Right: PDF of amorphous and re-milled calcined $Na_2P_2S_6$.

4.9. Conclusion

The long-range and local structures in amorphous and crystalline $Na_2P_2S_6$ and also their changes during synthesis have been observed by XRD, XRD-PDF analysis, Raman spectroscopy, and $^{23}Na/^{31}P$ MAS NMR spectroscopy. From the Raman spectrum, no distinction between the different P–S structures is possible. The NMR spectrum of crystalline $Na_2P_2S_6$ shows two P signals that are in good agreement with the crystalline structure of $Na_2P_2S_6$ determined by Rietveld refinement. ^{31}P MAS NMR also shows a difference in the chemical shifts of crystalline and amorphous $Na_2P_2S_6$ revealing the presence of different local building blocks in these materials. The measurements indicate that single PS_4^{3-} tetrahedra and corner-sharing tetrahedra are transformed to edge-sharing-tetrahedra during crystallization of amorphous $Na_2P_2S_6$ to crystalline $Na_2P_2S_6$.

Through this complementary use of material characterization techniques, the difference between an amorphous and crystalline structure of equal stoichiometry could be proven.

The difference in molecular structure with the same stoichiometry causes a difference in the material characteristics, which was demonstrated here by the ionic conductivity. Interestingly, ball milling is adding enough energy to destroy the adamantane-like P_4S_{10} structure and for the nucleophilic attack of the sulfide anion to the phosphorus atom. But this process only happens for sulfide atoms stemming from Na_2S via cleavage of the P_2S_5-molecule. To make the intramolecular nucleophilic attack happen and thus form $P_2S_6^{2-}$ units, the sample apparently has to be thermally annealed.

A re-amorphization of the crystalline $Na_2P_2S_6$ can be observed after ball milling with XRD, XRD-PDF analysis, and ^{31}P MAS NMR spectroscopy. In terms of structural conversion, the process of milling and thermal annealing can be considered as opposed in this work.

5. Hydrogarnet-to-garnet conversion: Suppression of lithium diffusion barriers in the solid-state ion conductor LLZO with Al^{3+}, Nb^{5+}, Ta^{5+} and W^{6+} as cationic substituents

The garnet-type structure $La_3Li_5M_2O_{12}$ (M=Nb, Ta) is first described by Mazza[117] and Hyooma[74] in 1988. Substitution of Nb, Ta with Zr yielded remarkably high Li^+ conductivities ($3 \cdot 10^{-4}$S cm^{-1} at 25 °C) and made the ceramic a candidate as solid state Li-ion conductor[123] To improve the ionic conductivities, high mobility and high density of charge carriers must be achieved. Among other methods, substitution in the cation lattice has been proven to increase the ionic conductivity in LLZO materials.[194] Aliovalent substitution of the cations is on the one hand required for the stabilization of the cubic structure at ambient conditions, which yields much higher conductivities as compared to tetrahedral counterparts. On the other hand, it can induce disorder into the structures, which is known to be beneficial for ionic conductivities.[64,94,95] Substitution with higher valence cations can lead to a higher local mobility of ions.[3] It is assumed, that a maximum of sublattice entropy in garnet-type structures could have an enhancing effect on the Li^+ conductivity. Thorough choice of the substituents allows tuning the materials properties and gaining more efficient sintering conditions and thus economic fabrication for industrial application.

5.1. Aim of the work

We investigated why commercial $Li_7La_3Zr_2O_{12}$ (LLZO) with Nb- and Ta substitution shows a dramatically decreased mobility on a local scale, as observed with temperature-dependent NMR techniques, compared to Al and W substituted samples, although impedance spectroscopy on sintered pellets suggests the opposite: conductivity values do not show a strong dependence on the type of substituting cation.

The influence of the four different substituents Al^{3+}, Nb^{5+}, Ta^{5+} or W^{6+} on the crystal structure and local distortions of LLZO is examined by means of X-ray and neutron powder diffraction (XRD/NPD) as well as by ^6Li and ^{27}Al magic-angle spinning (MAS) nuclear magnetic resonance (NMR) spectroscopy. A total scattering pair distribution function analysis (PDF) provides an explanation for the local structural differences. The formation of geometric frustration induced by ball milling and its reversal by temperature treatment is investigated with XRD and PDF. The short-range Li^+-ion dynamics are studied using temperature-dependent static ^7Li NMR lineshape measurements and

^{7}Li NMR spin-lattice relaxation experiments (T_1). We show that the thermal treatment induces the hydrogarnet-to-garnet transformation. This has an effect on the bulk Li^+ conductivity, which becomes that much enhanced that it can be assessed by [7]Li pulsed field-gradient (PFG) NMR and impedance measurements on sintered pellets.

LLZO reference compounds were synthesized according to the composition specified by the manufacturer by a high temperature route. Their cubic structure is revised by XRD. Their local structure is observed with [6]Li and ^{27}Al MASS NMR and compared to the commercial samples. With ^{7}Li NMR lineshape and spin-lattice relaxation experiments, the results of the commercial LLZO samples are reproduced and thus verified.

Thermal expansion of LLZO with Al^{3+}, Nb^{5+}, Ta^{5+} or W^{6+} substituent is assessed with diffraction and its chemical stability against various solvents is also examined. A treatment with acetic acid is aimed to force an H^+/Li^+ exchange.

5.2. Crystal structure

XRD and NPD patterns for commercial Al-, Nb- Ta-, and W-substituted LLZO together with corresponding Rietveld refinements are shown in Figure 30 to Figure 31. The results of the refinements are listed in Tab. 7. The refinement reveals LLZO in garnet-type

Table 7. – Results of the Rietveld refinement of commercial Al-, Nb- Ta-, and W-substituted LLZO.

Substituent: Stoichiometry	Crystal structure	Lattice parameter a / Å	Cell volume V / Å³	Structural strain /dD/D·10^{-4}
Al: $Li_{6.25}Al_{0.25}La_3Zr_2O_{12}$	Garnet / hydrogarnet	12.993	2193.4	16.28
Nb: $Li_{6.5}La_3Zr_{1.5}Nb_{0.5}O_{12}$	Hydrogarnet/ hydrogarnet 48.93 wt-% /46.27 wt-%	13.107 / 12.988	2251.9/ 2190.7	37.93 / 64.50
Ta: $Li_{6.6}La_3Zr_{1.4}Ta_{0.6}O_{12}$	Hydrogarnet/ hydrogarnet 43.18 wt-% /56.82 wt-%	13.082 / 12.985	2237.8 / 2189.5	50.74/50.74
W: $Li_{6.3}La_3Zr_{1.65}W_{0.35}O_{12}$	Garnet	12.935	2178.1	26.09

structure with symmetry Ia$\bar{3}$d (space group No. 230, based on a structural model from Awaka et al.[7]) as the main phase for W-substituted LLZO with lattice parameter a = 12.935 Å. Both Li positions 24d and 96h are refined to low occupancy in a free refinement.

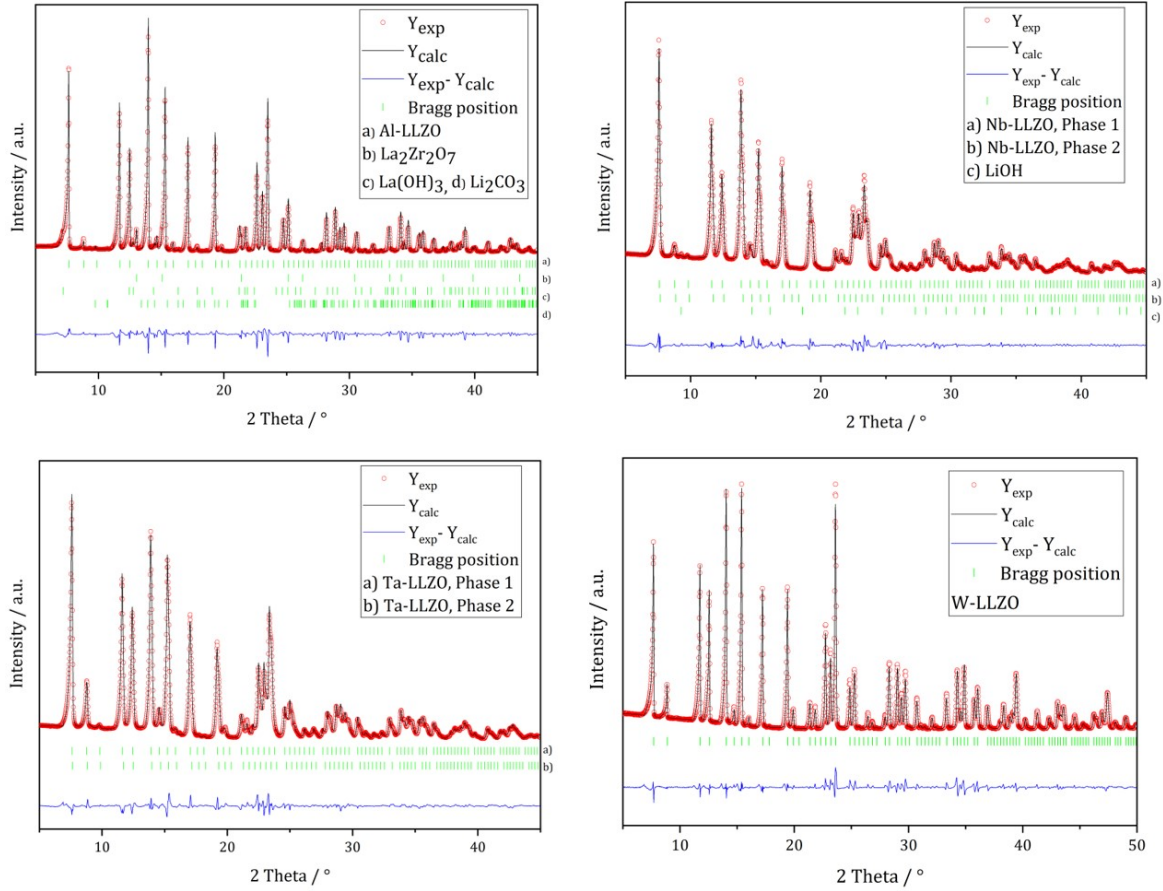When refining against the diffraction data of Nb- and Ta-LLZO, a garnet-type structure

Figure 30 – Rietveld analysis of diffraction patterns (Mo K$_{\alpha 1}$) of commercial Al-, Nb-, Ta-, and W-substituted LLZO.

model was initially applied. However, a Rietveld refinement with the garnet model could not accurately reproduce the data. In additon, the reflection 310 at $2\theta = 9.9°$ could not be assigned. Eventually, a refinement with a hydrogarnet I$\bar{4}$3d structure (space group No. 220, based on a structural model from Wagner et al.[186]) and two different lattice parameters describes the diffraction data precisely. The lattice parameters are refined to a = 13.107 Å and c = 12.988 Å for Nb-LLZO, and a = 13.082 and c = 12.985 Å for Ta-LLZO. Additionally, a superposition of reflections with the same crystal structure but different lattice parameters in the X-ray diffraction data of Nb- and Ta-LLZO is observed. This could be attributed to a chemical inhomogeneity as suspected by Yamada et al. for Ta-substituted LLZO.[196] A similar superposition could be refined with a model with two different lattice parameters by Zeier et al.[200] In both cases the hydrogarnet phase with a smaller lattice parameter is refined with a higher microstrain, corresponding to a higher relative amount of substituting Nb^{5+} resp. Ta^{5+} for Zr^{4+}. This can be derived from the cation radii listed in Tab. 2 in chapter 3.2.2.

For the example of Ta-LLZO, the substituent Ta is localized on the Zr site 16c in the
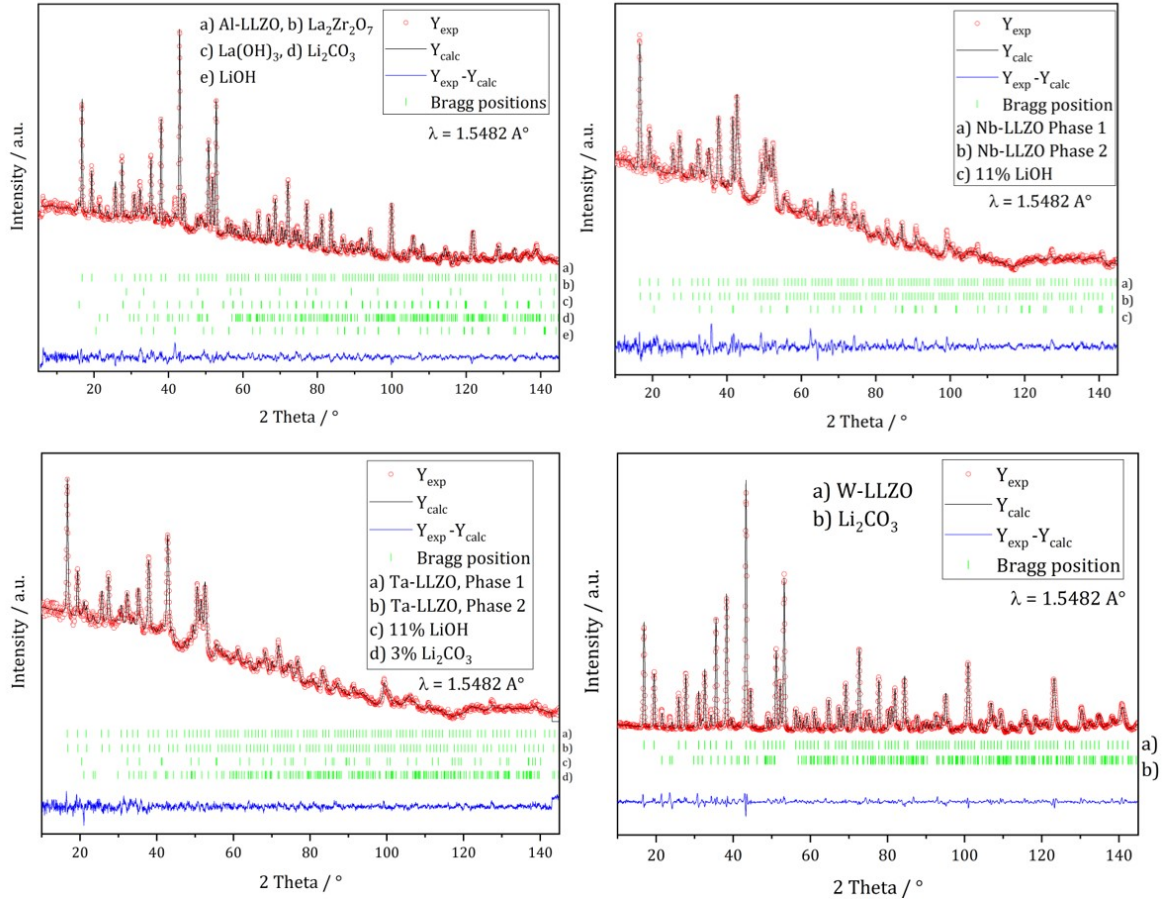
Figure 31 – Rietveld analysis of neutron diffraction patterns of commercial Al-, Nb-, Ta-, and W-substituted LLZO.

phase with the smaller lattice parameter. Based on the scattering factors, it can be assumed for the phase with the larger lattice parameter, that Ta is localized on the La site 24d. La is distributed on the "La site" 24d and "Zr site" 16c. An occupation of the same crystallographic site by both Zr and La can be found in the oxide $La_2Zr_2O_7$, too.[137] Details about the structural model can be found in the ESI in Tab. 15. This difference in the occupation of the crystallographic positions of La and Ta could be the reason for the discrete formation of two structures with different lattice parameters instead of an even distribution.

Both general Lithium positions 12a and 12b are refined to very low occupancy values, whereas the special Li position 48e is refined to full occupancy in a free refinement. A fully occupied Li3 position can be regarded as a bottleneck for long-range Li transport, as depicted in Fig. 32. Diffraction data of Al-LLZO can be described with both types of structures with a lattice parameter of a = 12.993 Å. Based on the crystallographic hydrogarnet structure published by Wagner and Rettenwander et al.[186], Al^{3+} is located on both a tetrahedrally coordinated position of Li1 and an octahedrally coordinated position of Zr. The total occupancy of the position is constrained to the defined stoichiometry
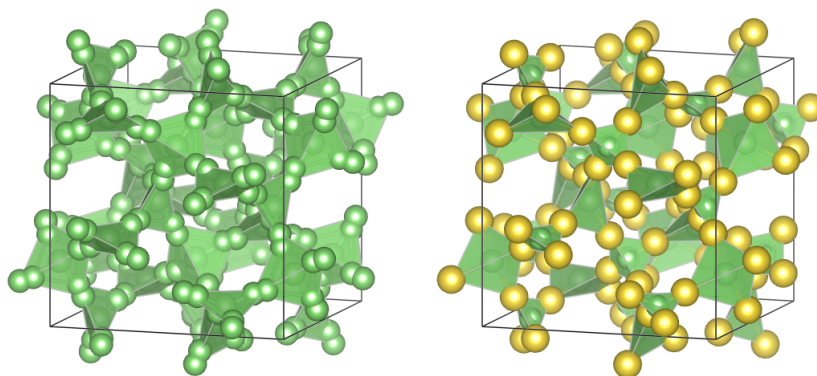
Figure 32 – Lithium distribution within a) Garnet and b) Hydrogarnet. Green: Li1 and Li2, yellow: Li3.

found with ICP-OES. In contrast, Nb^{5+}, Ta^{5+} and W^{6+} are located on the octahedrally coordinated position of Zr^{4+} and the total occupancy of the position is constrained to the stoichiometry as described above.

Traces of anhydrous LiOH have also been noticed in NPD datasets for Al-LLZO (1 wt-%), Nb-LLZO (11 wt-%) and Ta-LLZO (11 wt-%). Reflections of crystalline Li_2CO_3 are detectable in NPD data of Al-LLZO (1 wt-%), Ta-LLZO (3 wt-%), and W-LLZO (2 wt-%). 2 wt-% crystalline $La_2Zr_2O_7$ are found in Al-LLZO.

LLZO with the same stoichiometry as the commercial samples was synthesized as a reference. The results of the Rietveld refinements can be found in the appendix in Tab. 16 and Fig. 76. The synthesized Al-, Nb-, and W-LLZO samples crystallize in the garnet structure. Synthesized Ta-LLZO is a mixture of garnet and hydrogarnet LLZO.

5.3. Local structure

Fig. 33 presents the ^{6}Li MAS NMR spectra of commercial and synthesized Al-, Nb-, Ta-, and W-LLZO. Strong differences can be observed in the line width of the spectra. The spectra of the hydrogarnet samples are broader, which points at stronger variations in the local environment around the Li site. In addition, the spectra of commercial Ta-, Nb- and Al-LLZO (hydrogarnet) represent at least two chemically inequivalent Li positions/environments. In contrast, all synthesized samples and the commercial W-LLZO show a clearly different structural arrangement – a narrow ^{6}Li peak is located at 1.12-1.30 ppm. This signal includes resonances from the Li sites in octahedral and tetrahedral environments between which fast exchange can occur. A similar chemical shift for unsubstituted garnet-type LLZO has been observed and discussed by Larraz et al. [104]

Two lithium sites in commercial Nb- and Ta-substituted LLZO can be distinguished. It can be assumed that the signal at 0.2 ppm stems from the additional highly occupied Li3 site featured in the hydrogarnet structure. The ^{6}Li signals of the hydrogarnet structure
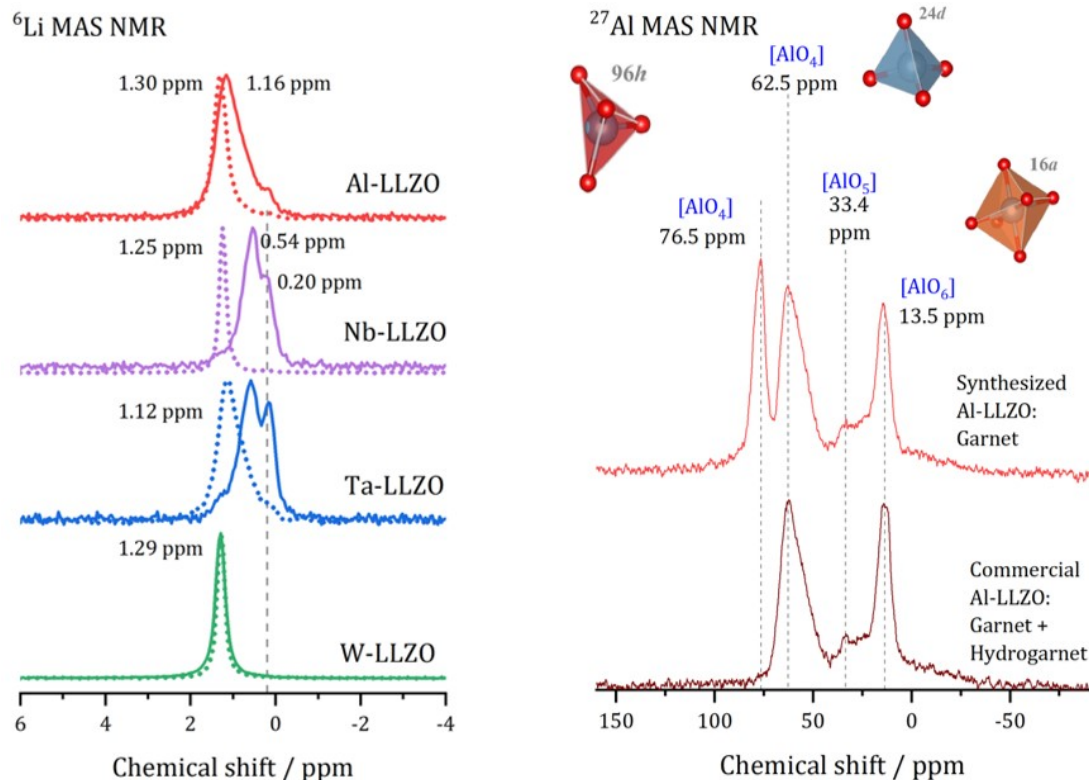
Figure 33 – Left: ^{6}Li MAS NMR spectra of LLZO, solid lines: commercial samples, dashed lines: synthesized samples, right: ^{27}Al MAS NMR spectra of Al-substituted LLZO samples. Tetrahedra taken from [141]

in Nb-and Ta-LLZO (commercial samples) are shifted upfield compared to those of the garnet signals and occur at 0.54 and 0.58 ppm. The corresponding signals of Nb- and Ta-LLZO with garnet structure (synthesized samples) occur at 1.25 and 1.12 ppm. Synthesized Ta-LLZO shows a shoulder comparable to that of commercial Al-LLZO so the presence of both garnet and hydrogarnet structure is assumed. The assignment of the upfield signal to the tetrahedral and the low-field signal to the octahedral coordination made by van Wüllen is contradictive to the refinement in this work, according to which these two positions are calculated to low values of occupancy.[179] It is assumed that Li$^+$, apart from the special Li3 site in the hydrogarnet structure, is highly mobile and occupies two not clearly distinguishable sites. The appearance of the ^{6}Li NMR spectra correlates very well with the conclusions deduced from structural studies with XRD and neutron diffraction. However, no LiOH and Li$_2$CO$_3$ signals are observed with NMR spectroscopy. The reason can be that the intensity of these signals are very small due to the low abundance and are superimposed by the main phase resonances. The spectrum of lithium hydroxide and lithium carbonate can be found in the appendix in Fig. 83. The ^{27}Al MAS-NMR spectra allow to gain a further insight into the structure of Al-LLZO. The ^{27}Al spectra of commercial and synthesized LLZO are depicted in Fig. 33.

(a) Ta-LLZO: Hydrogarnet   (b) Ta-LLZO: Hydrogarnet
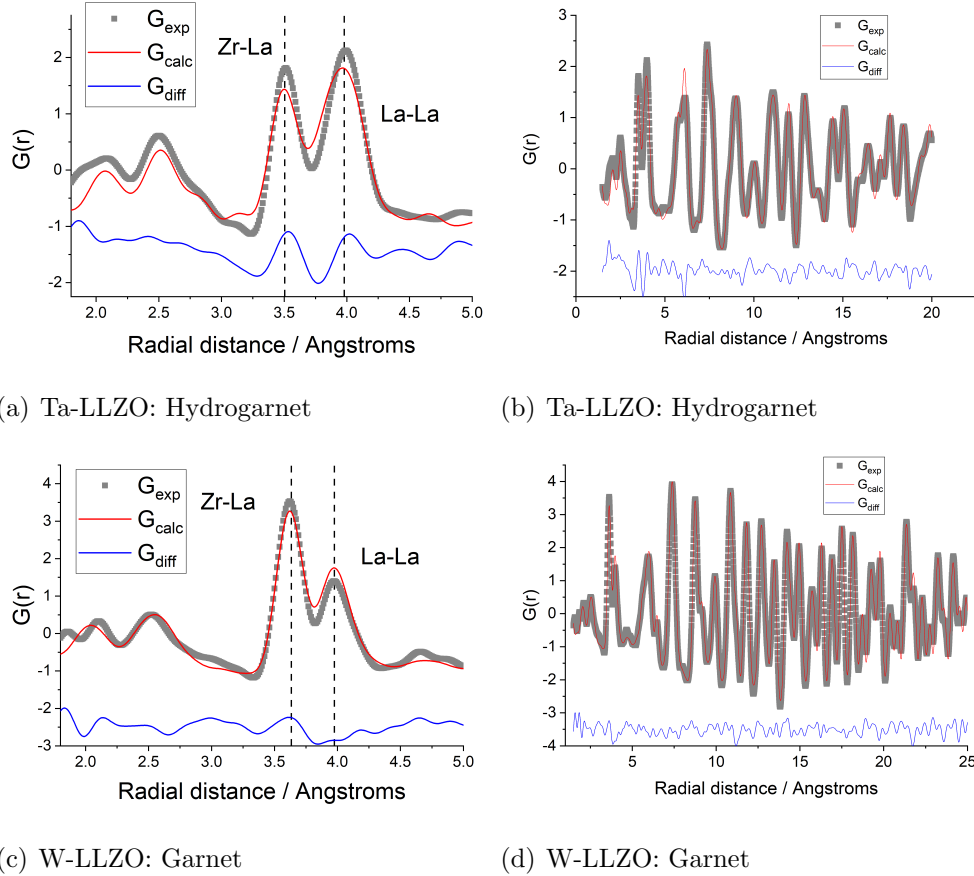
(c) W-LLZO: Garnet   (d) W-LLZO: Garnet

Figure 34 – Pair distribution functions and fittings of commercial Ta- and W-substituted LLZO.

The commercial sample exhibits Al in three signals that can be assigned to different coordinations: 13.5, 33.4 and 62.5 ppm. An additional signal at 76.5 ppm is observed for the the synthesized Al-LLZO. ^{27}Al NMR studies on Al-substituted LLZO have been presented by Rettenwander et al. and Geiger et al. They assigned a signal at 65.9 ppm to the 24d position and a signal at 79.5 ppm to the 96h position which are both tetrahedrally coordinated by oxygen.[52,141,142] The 96h position is a distorted tetrahedron.[141] The signal at 33.4 ppm represents Al in fivefold and 13.5 ppm in octahedral coordination.[143] The octahedrally coordinated site is occupied by Zr at a 16a position. There are no significant indications for Al-containing impurity phases, so a multiple substitution of Li1 24d, Li2 96h, and Zr16a by Al is assumed.

It was not possible to locate the octahedrally coordinated Al in the crystal structure with the diffraction data from this study. Buschmann et al. and Geiger et al. were trying to locate Al in a refinement, too. They stated it cannot be localized due to the heavier scatterers La and Zr.[16,52]

The commercial Al-LLZO sample is supposed to be a mixed phase of hydrogarnet and garnet LLZO. There is no 96h position for Li in the hydrogarnet structure. This can be seen in the ^{27}Al MAS-NMR spectrum: The 96h position is not occupied by Al.
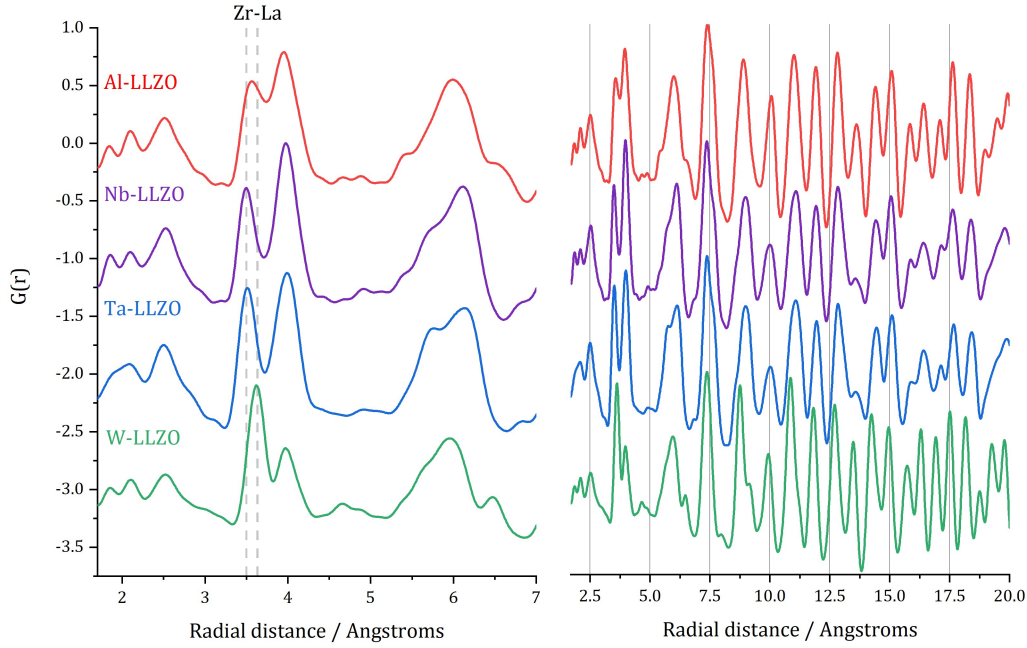
Figure 35 – Pair distribution functions of commercial LLZO with Al-, Nb-, Ta-, W substituent.

XRD-PDF is a versatile tool to analyze the local structure based on atomic distances. It can be used to reveal local distortions which may come from frustration as Kozinsky suspects for the La sublattice.[94] A cutout of a PDF analysis and fit of Ta- and W-LLZO is depicted in Fig. 34. A garnet-type model is used for W-LLZO whereas Ta-LLZO can be described using two hydrogarnet models with different lattice parameters, as observed with XRD. Though the occurrence of two different lattice parameters blurs the signal positions, one can distinguish between the two structures as expected from a calculation of the radial distribution function (see Fig. 78 and 79 in the appendix). The most striking feature is the position of the Zr-La signal at 3.5 Å in the hydrogarnet structure and 3.6 Å in the garnet structure. The symmetry reduction turns the fixed Zr^{4+} position into a special position and causes a frustrated La sublattice.

The PDF of Al-LLZO proves the suspection that this material is a mixture of both garnet and hydrogarnet-structured LLZO. A PDF comparison of all Al-, Nb-, Ta-and W-substituted samples is depicted in Fig. 35. The Zr-La signal of commercial Al-LLZO is a superposition between 3.5 an 3.6 Å.

Note that the ratio of intensity of the Zr-La signal at 3.5/3.6 Å and the following at 4.0 Å is also different for garnet and hydrogarnet. However, this can be superimposed by the different scattering intensities of the substituting atoms which is not taken into account in the calculation of the radial distribution function.

5.4. Structural conversion

Commercial W-LLZO and all of the synthesized reference samples crystallize in the garnet structure as demonstrated by XRD, NPD and NMR. This indicates that not the substitution of aliovalent cations itself leads to the observed symmetry reduction, but an additional treatment of the samples. Therefore, a closer look will be taken on the ball milling and sintering process.

5.4.1. Mechanical treatment by ball milling

The commercial LLZO samples were ball milled in 2-propanol for 1 h. The recorded X-ray diffraction patterns of the dried, ball milled materials are depicted in Fig. 36. No
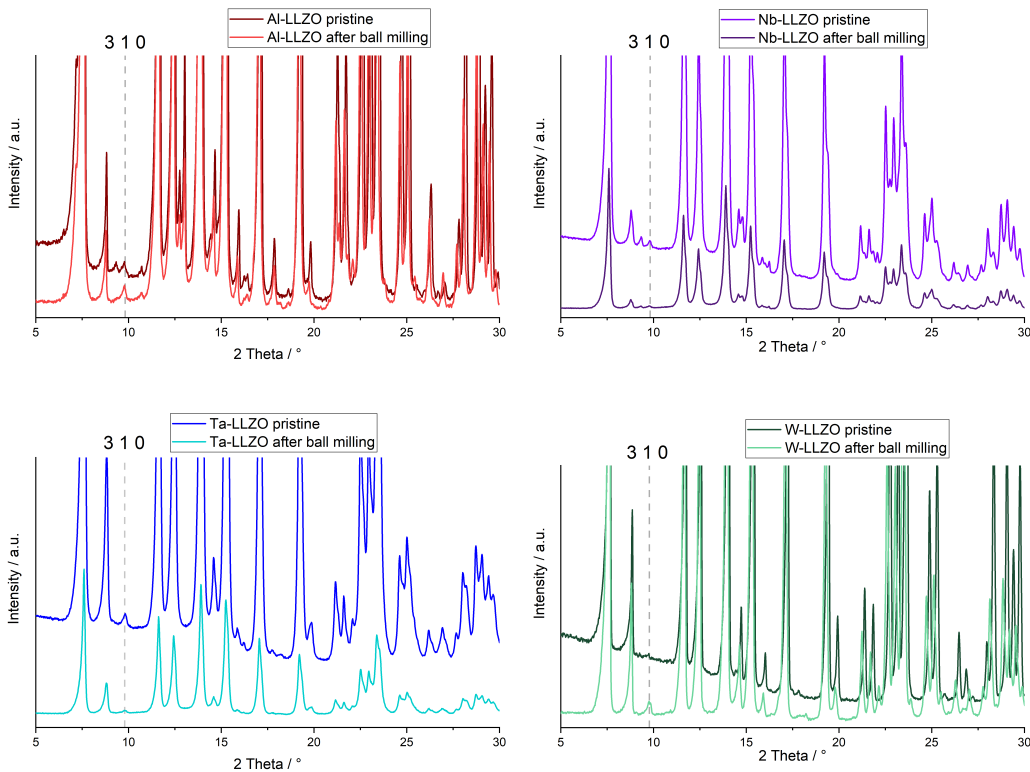
Figure 36 – Mo $K_{\alpha 1}$ diffraction patterns of commercial Al-, Nb-, Ta- and W-LLZO pristine and after ball milling.

additional reflections are observed with XRD after ball milling of Nb- and Ta-substituted LLZO. A decrease in the reflection intensities is due to a loss of crystallinity after the harsh mechanical treatment. Additionally, no distinct separation of the two cubic phases in each material can be noted. The characteristic hydrogarnet reflection of 310 is observed after ball milling for all samples. This leads to the conclusion that the commercial Nb- and Ta-LLZO samples have been milled by the supplier.

A Rietveld refinement against a ball milled W-LLZO diffraction pattern with a hydrog-

arnet model is depicted in Fig. 37 and confirms the structural transformation.

No clear statement about a phase transition between garnet and hydrogarnet of Al-LLZO is possible with the data displayed in Fig. 36. Besides the missing assignment of the pristine phase to either garnet or hydrogarnet, the determination of the phase is additionally hindered by superimposing signals of Li_2CO_3.
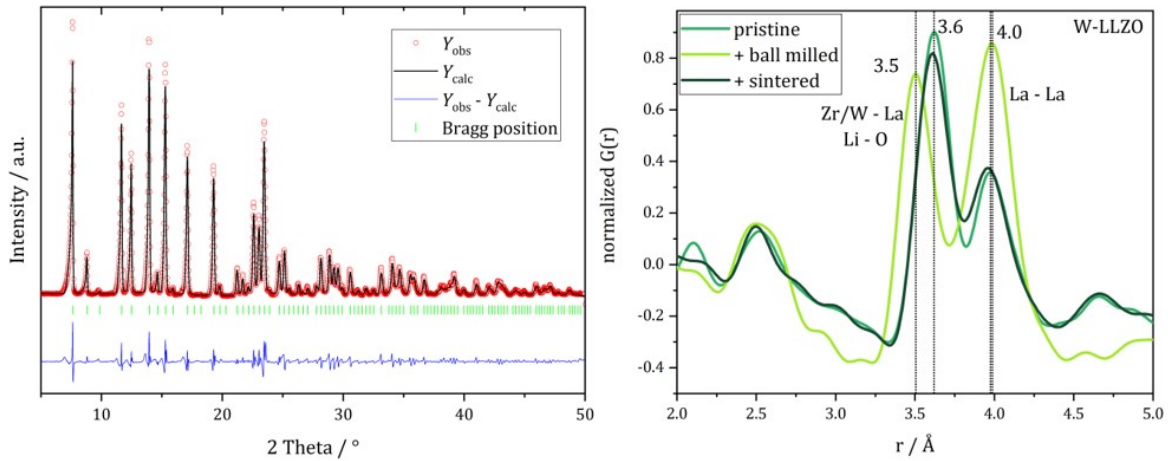

Figure 37 – Left: Rietveld-refined diffraction data (Mo $K_{\alpha 1}$) of commercial W-substituted LLZO after 1h ball milling with a hydrogarnet model. Right: Pair distribution functions of commercial W-LLZO: pristine, ball milled and sintered.

5.4.2. Thermal treatment by sintering

XRD measurements were performed on sintered commercial samples as collected in Fig. 38. It can be concluded, that sintering procedure results in a complete conversion to the garnet structure independent from the pristine state (hydrogarnet or garnet), crystallinity, or substituting element. The impurity of Al-LLZO results in a large number of secondary phases after sintering. A Rietveld-refined diffraction pattern is exemplary shown in Fig. 38 for sintered commercial Ta-LLZO using a garnet structure model.

5.4.3. Symmetry reduction

A full cycle of conversion is observed for W-LLZO. Garnet W-LLZO is ball milled for 1h as mentioned above and subsequently sintered. While the symmetry reduction causes only minor changes in the XRD pattern, with the risk of being overlooked, the local structural changes are more obvious. In Fig. 37, the low r (< 5 Å) region of the PDFs of all three synthesis steps (pristine, ball milled and sintered) are displayed. The differences below 3 Å are small and the corresponding distances are hard to distinguish from each other. The two peaks corresponding to [Zr/W – La] and [La – La] distances, however,
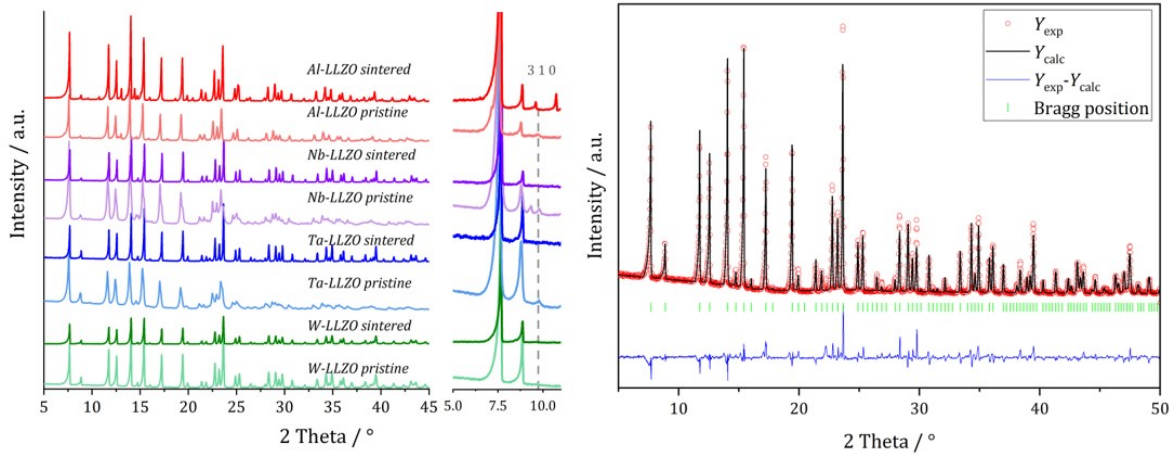
Figure 38 – Left: Mo K$_{\alpha 1}$ diffraction patterns of commercial Al-, Nb-, Ta- and W-LLZO pristine and after calcining, right inset shows a zoom into the region were the additional 310 reflection of the hydrogarnet structure shows. Right: Rietveld refinement against diffraction data of sintered commercial Ta-LLZO with a garnet model.

differ clearly in the PDF of the ball milled sample. The shift of the Zr-La distance from 3.6 Å in the pristine material to 3.5 Å after ball milling proves that the hydrogarnet structure is formed. The conversion from hydrogarnet back to garnet during sintering can be observed with the Zr-La distance shifting back to 3.6 Å.

In the garnet structure, Zr/W and La occupy the special Wyckoff sites 16a (0,0,0) and 24c (1/8, 0, 1/4), respectively. Therefore, the [Zr/W – La] distance can only be reduced by a reduction of the symmetry, where the atoms occupy mobile positions. This is the case in the hydrogarnet structure, where the 16c becomes (x, x, x) and 24d (x, 0, 1/4), respectively.

5.5. Local Li ion hopping

The local hopping of Li ions on time scales of ns is investigated by temperature-dependent measurements of the so-called spin-lattice relaxation rate T_1^{-1} and motional line narrowing. Fig. 39 shows the temperature dependence of T_1^{-1} (T^{-1}) for all LLZO samples. In the case of commercial W-LLZO and synthesized Nb-LLZO and W-LLZO, a clear maximum is observed and a fit according to Bloembergen, Purcell and Pound (eq. 13) and Arrhenius (14) is added as solid line. From the hopping rate of the Li ions, a diffusion coefficient D can be estimated via the Einstein-Smoluchowski equation 17 (chapter 2.1.3.) again assuming uncorrelated jumps: The extracted parameters of Li mobility are summarized in Tab. 8. These three samples reveal similar local dynamics with estimated Li conductivities in the range between 0.23 and 0.50 mS cm^{-1}. For the other samples, the maximum in T_1^{-1} (T^{-1}) occurs at higher temperatures outside the experimentally accessible temperature range, indicating slower local dynamics of the Li ions.

Table 8. – Motional parameters for local hopping estimated from T_1^{-1} relaxation studies (25°C).

Sample	E_A / eV	τ^{-1} / s^{-1}	D / m^2 s^{-1}	σ / S cm^{-1}
Commercial W-LLZO	0.22 ± 0.04	3.1·10^7	1.6·10^{-13}	2.3·10^{-4}
Synthesized Nb-LLZO	0.23 ± 0.01	2.5·10^7	1.3·10^{-13}	1.8·10^{-4}
Synthesized W-LLZO	0.23 ± 0.01	1.4·10^7	7.1·10^{-14}	1.0·10^{-4}

Further insights into the dynamics of the Li ions on time scales of some ms can be obtained by the temperature dependence of static ^{7}Li NMR spectra (nuclear spin I = 3/2). Fig. 40 shows exemplary the spectra of commercial W-LLZO and Nb-LLZO for temperatures between 243 K and 553 K.

At 243 K, a broad contribution is visible for W-LLZO around 50 kHz corresponding to the quadrupolar satellites, i.e. the nuclear spin transitions $|+3/2\rangle \leftrightarrow |+1/2\rangle$ and $|-1/2\rangle \leftrightarrow |-3/2\rangle$. On top of this broader contribution, a narrower signal is visible with a width of about 8 kHz corresponding to the central transition $|+1/2\rangle \leftrightarrow |-1/2\rangle$. With increasing temperature, a so-called motional narrowing is visible, i.e. a reduction of the width of both contributions to the spectrum. This narrowing occurs when the average hopping rate of the ions/nuclei exceeds the width of the spectral components resulting in temporal averaging of the local environments around the Li nuclei on time scales of the inverse line width. The line width (FWHM) is shown for all samples in Fig. 41, again for temperatures between 243 K and 553 K. For some samples, e.g. commercial and synthesized Ta-LLZO, a clear step-like behavior is observed. At low temperatures, a plateau is visible with a width of about 7 kHz, representing the strength of interactions of the ^{7}Li nuclei with their environment. At temperatures between 350 K and 450 K the motional narrowing can be observed. Above 450 K, a high temperature plateau with a width of about 0.5 kHz is visible which just reflects the inhomogeneity of the external magnetic field.

Corresponding fits to the Hendrickson and Bray eq. 15 (chapter 2.1.3.) are shown in Fig. 41 as solid lines. The extracted activation energies are 0.47 eV for synthesized Al-LLZO, 0.38 eV for commercial Nb-LLZO and 0.33 eV for commercial and synthesized Ta-LLZO. It should be noted that for commercial/synthesized W-LLZO and for synthesized Nb-LLZO the low-temperature plateau is not accessible in this temperature range, i.e. the motional narrowing starts already at lower temperatures. This again indicates fast local diffusion for these three garnet-structured samples, fully consistent with the T_1^{-1} NMR results described above. MLN and T_1^{-1} relaxation are examined in Wagner et al. The results for Ga-substituted LLZO in garnet structure correspond to those in our experiment in terms of reaching the narrowing regime at 273 K. It is described that a shift of the motional narrowing curve to higher temperatures is observed in one LLZO
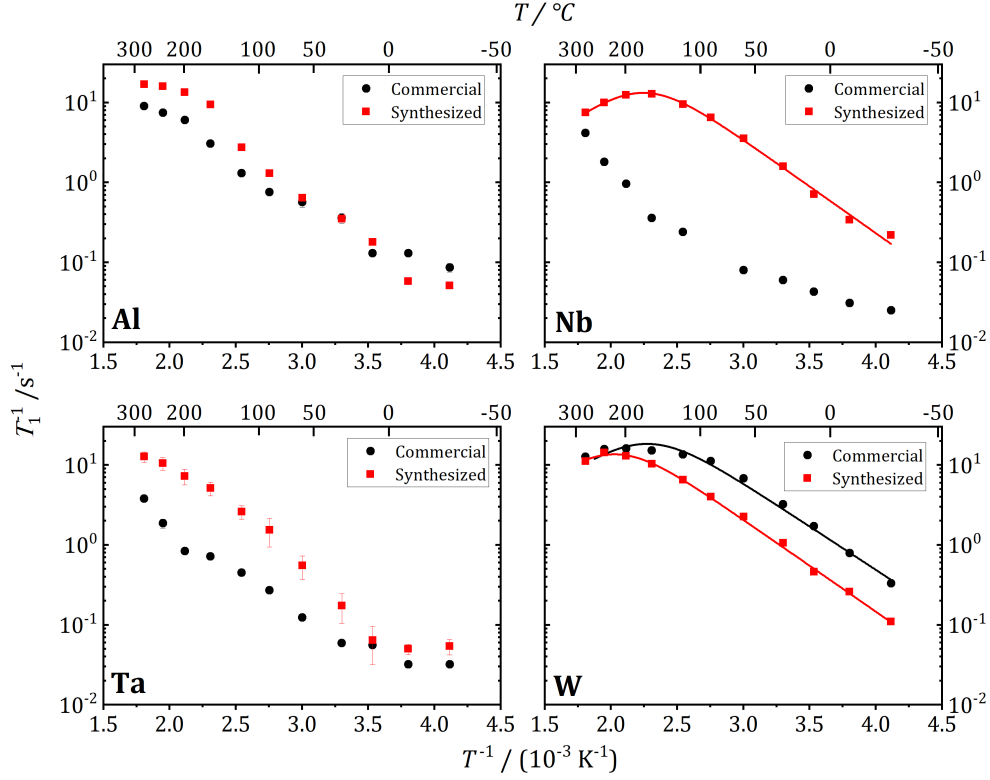
Figure 39 – ^{7}Li NMR relaxation rates T_1^{-1} vs inverse temperature for commercial and synthesized Al-, Nb-, Ta- and W-substituted LLZO. Solid lines show fits according to eq. 14

sample, which is linked to a lower local mobility of Li$^+$ (see Fig. 15 in chapter 3.3.3.). The activation energy extracted from T_1^{-1} measurements is quantified to 0.13 eV for Al-substituted LLZO and 0.14 eV for Ga-substituted LLZO.[186] The activation energies reported from Wagner et al. are lower compared to the experiments in this study. This could possibly be attributed to the different substituents.
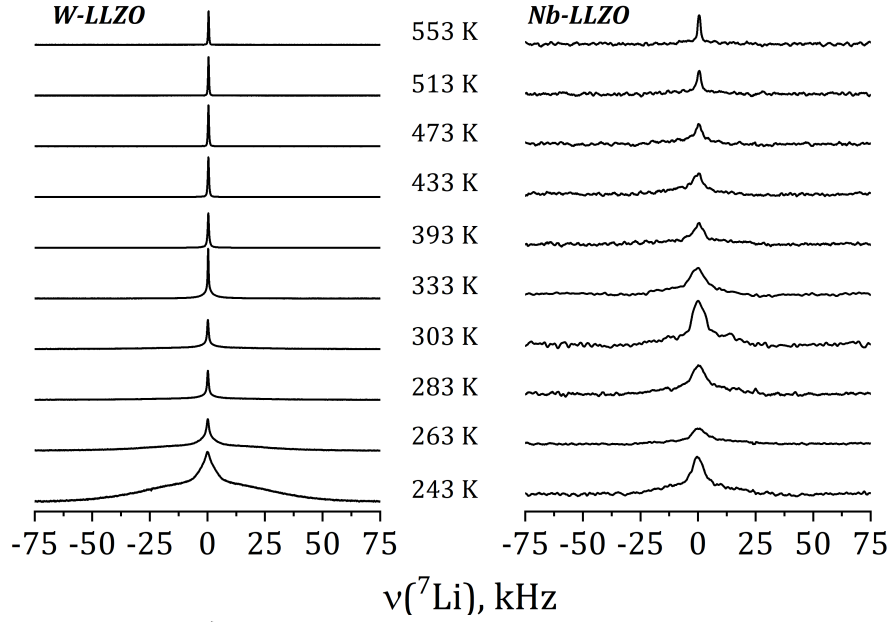
Figure 40 – Static ^{7}Li NMR spectra of commercial samples from 243 to 553 K.
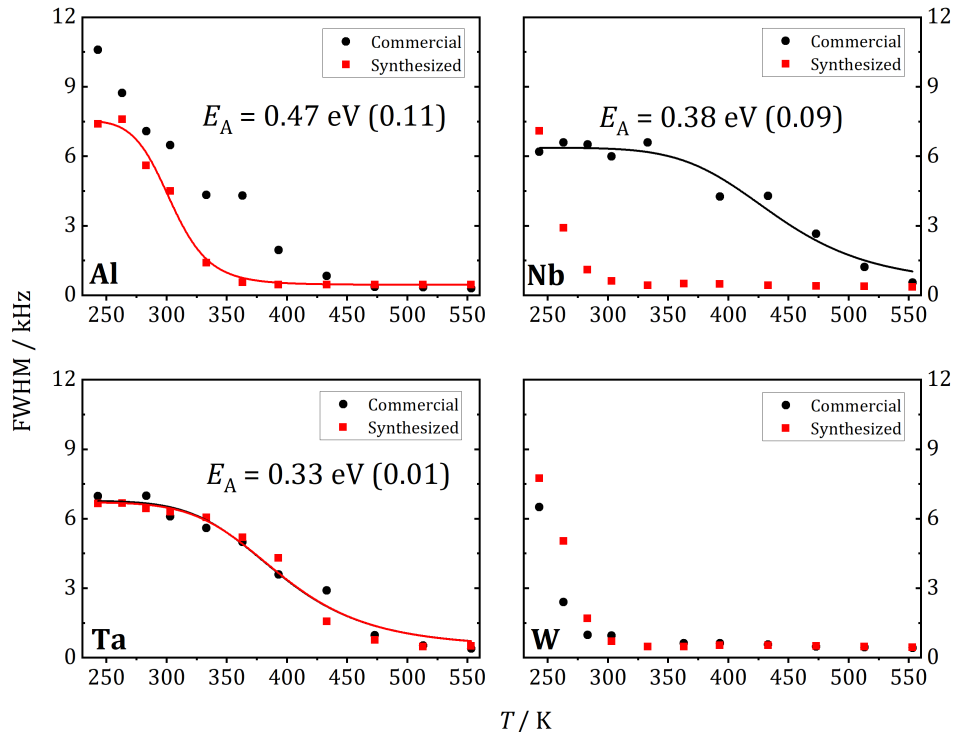
Figure 41 – Linewidth vs. temperature of commercial and synthesized Al-, Nb-, Ta- and W-substituted LLZO and extracted activation energies (same value for both commercial and synthesized Ta-substituted LLZO), standard deviation in brackets.

5.6. Li$^+$ conductivity

The long-range transport of the Li ions was investigated by ^{7}Li PFG NMR measurements on these three samples. For the other samples, diffusion was not fast enough to get meaningful signals. Fig. 42 shows exemplary the results for commercial W-LLZO for temperatures between 313 K and 343 K. The echo damping I/I_0 as a function of the gradient strength g can be well described with a Gaussian function, as expected from the Stejskal-Tanner equation.[162] The extracted diffusion coefficients are listed in Tab. 9.
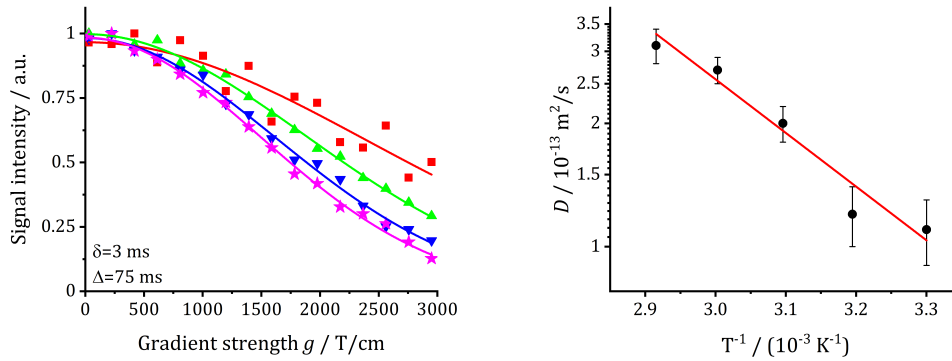
Figure 42 – Echo damping vs gradient field strength g and extracted diffusion coefficients for commercial W-LLZO.

The Li conductivity can again be calculated from the diffusion coefficients according to eq. 18. Overall, faster Li mobility for commercial/synthesized W-LLZO and synthesized Nb-LLZO is observed in comparison to the other samples. A good agreement is obtained for the Li conductivity and the activation barriers when comparing T_1^{-1} measurements (ns time scale) with motional narrowing (ms) and PFG NMR (0.1 s). These three samples are also the ones that have a garnet structure and show very similar narrow peaks at about 1.25-1.29 ppm in the ^{6}Li MAS NMR spectra (Fig. 33). Using the approach described in the relaxation studies section, the diffusion coefficients can be transformed into conductivities. These values are also included in the table and can be compared

Table 9. – Diffusion coefficient D, activation energy E_A, and Li conductivity σ, as derived from the PFG NMR experiments in garnet-structured LLZO.

Sample	D / m^2 s^{-1}	E_A / eV	σ / S cm^{-1}
Nb-LLZO synthesized	$(0.28 \pm 0.16) \cdot 10^{-13}$	0.45 ± 0.15	$4.0 \cdot 10^{-5}$
W-LLZO commercial	$(0.78 \pm 0.11) \cdot 10^{-13}$	0.35 ± 0.05	$1.1 \cdot 10^{-4}$
W-LLZO synthesized	$(0.96 \pm 0.69) \cdot 10^{-13}$	0.26 ± 0.23	$1.4 \cdot 10^{-4}$

Table 10. – Results of Li$^+$ conductivity and activation energy of sintered pellets as measured by impedance spectroscopy.

Sample	σ/ S cm^{-1}	E_A / eV
Al-LLZO, commercial	-	-
Nb-LLZO, commercial	$1.3 \cdot 10^{-4}$	0.33
Nb-LLZO, synthesized	$8.4 \cdot 10^{-5}$	0.37
Ta-LLZO, commercial	$1.8 \cdot 10^{-4}$	0.39
W-LLZO, commercial	$6.1 \cdot 10^{-5}$	0.33

with the data obtained by impedance spectroscopy.

Impedance measurements at 25, 35, and 45 °C of sintered Nb-, Ta-, and W-LLZO pellets and equivalent circuits are depicted in Fig. 43 to 45. The Li$^+$ conductivity is extracted from an extrapolation of the first semicircle to the x-axis intersection and listed in Tab. 10. A capacitance can be calculated from the value of the resistance in the maximum of the first semicircle using eq. 20. The values for the capacitance for each material are 4.3 · 10^{-10} F for Nb-LLZO, 8.4 · 10^{-10} F for Ta-LLZO and 3.3 · 10^{-10} F for W-LLZO. This is assigned to a grain boundary diffusion according to Irvine[76], see Tab. 1 in chapter 2.2.1. No data could be measured for sintered Al-LLZO, probably due to the high degree of La$_2$Zr$_2$O$_7$ impurity.

An activation energy for Lithium diffusion is calculated with an Arrhenius approach according to eq. 25.

$$\ln\left(\frac{\sigma}{\sigma_0}\right) = -\frac{E_A}{RT} \tag{25}$$

The conductivities are lower than the highest conductivities reported for each substituent: Nb-LLZO[47], Ta-LLZO[15], W-LLZO[108], which is attributed to the relatively shorter sintering time and lower sintering temperature. Based on the same sintering procedure, a slightly lower conductivity for W-LLZO and a slightly higher activation energy of Li-diffusion in Ta-LLZO is estimated compared to literature values. The comparison of the conductivities obtained with two independent techniques shows good agreement. The activation energies and conductivities are of the same order of magnitude, despite a higher experimental error due to the data scattering in PFG-experiments. The majority of the particle sizes are observed bigger than the distance covered during the PFG signal decay Δt = 75 ms corresponding to several micrometers[166] with SEM as pictured in Fig. 46. Note that the EIS results of Nb-LLZO and Ta-LLZO refer to the garnet structure due to the phase transition during sintering. A lower activation energy for Li diffusion in Nb-substituted LLZO in comparison with Ta-substitution has also been measured by Weppner et al.[175]
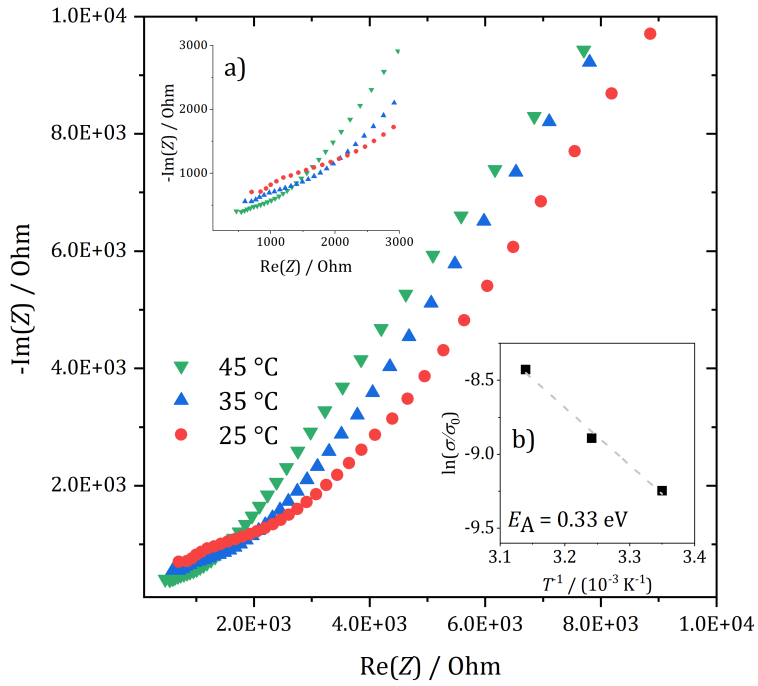
Figure 43 – Nyquist Plot of impedance spectroscopy measurement of a sintered Nb-LLZO Pellet, a) Zoom, b) Arrhenius approach, dashed line shows a fit according to eq. 25.
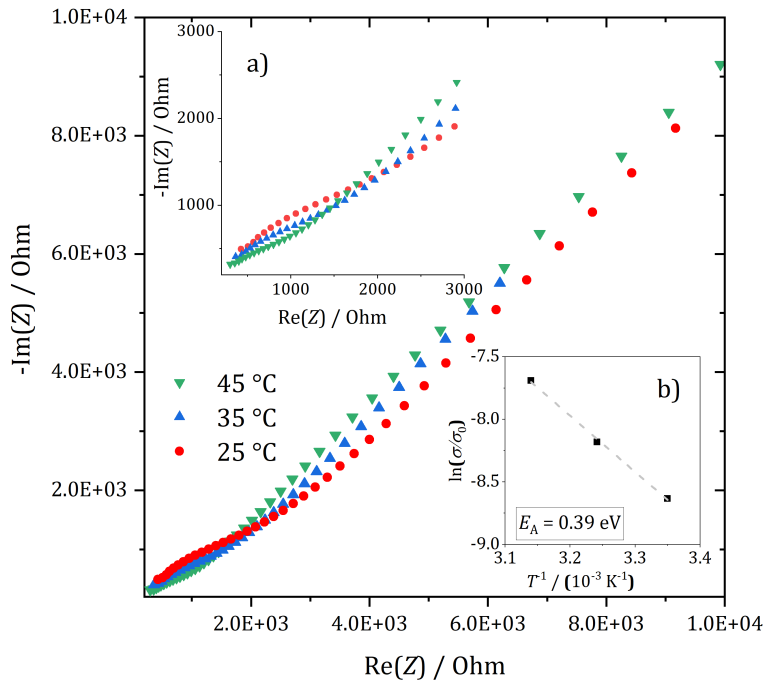

Figure 44 – Nyquist Plot of impedance spectroscopy measurement of a sintered Ta-LLZO Pellet, a) Zoom, b) Arrhenius approach, dashed line shows a fit according to eq. 25.
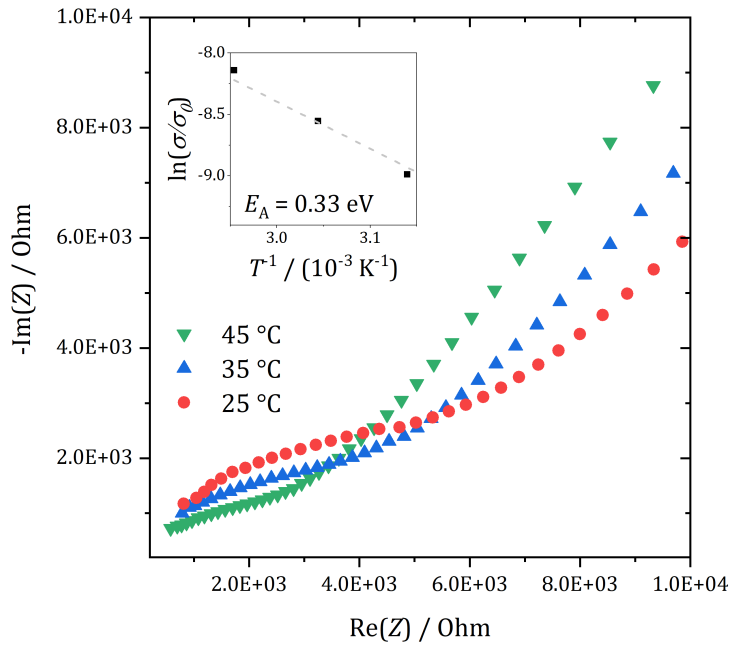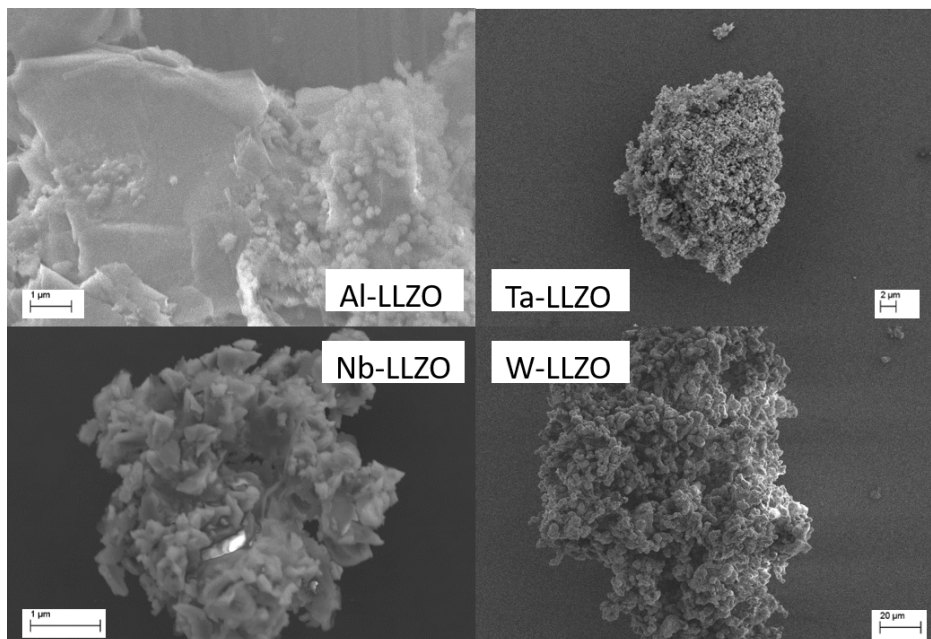
Figure 45 – Nyquist Plot of impedance spectroscopy measurement of a sintered W-LLZO Pellet, a) Zoom, b) Arrhenius approach, dashed line shows a fit according to eq. 25.

Figure 46 – SEM micrographs of commercial Al-, Nb-, Ta-, and W-substituted LLZO samples.

5.7. Surface and morphology

Raman spectroscopy is utilized to evaluate the surface since LLZO is prone to Li_2CO_3 passivation. The Raman spectra are depicted in Fig. 47. Small signals of Lithium carbonate appear at 1100 cm^{-1}. The signals at 769 and 789 cm^{-1} from Al- and Nb-LLZO can be assigned to the ZrO_6 tetrahedra.[177].
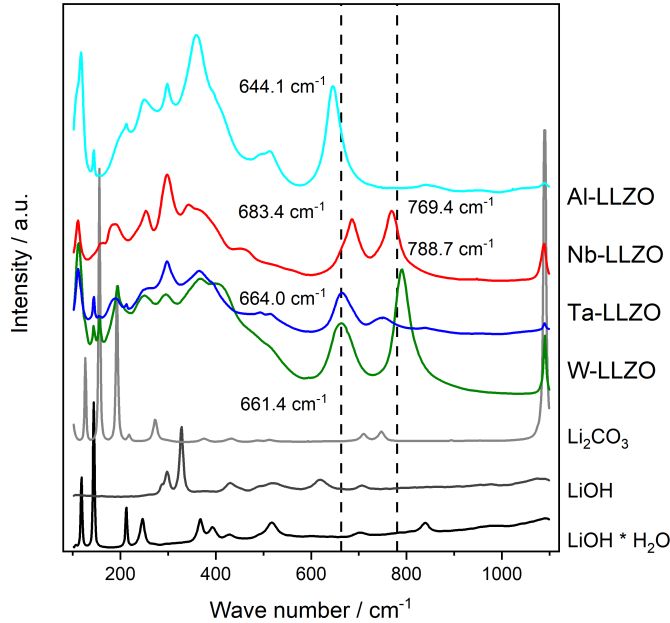
Figure 47 – Raman spectra of Al-, Nb-, Ta- and W-substituted LLZO, LiOH, LiOH·H_2O, and Li_2CO_3.

SEM micrographs of the commercial and synthesized LLZO samples are depicted in Fig. 46 (see previous chapter) and 48. All materials show homogeneous particles.

5.8. Thermal expansion

Temperature stability of commercial LLZO samples was assessed with high temperature in-situ diffraction. Figure 49 illustrates the expansion of the unit cell from 25 to 800 °C. The raw data can be found in the appendix in Fig. 80. Both a garnet and a hydrogarnet LLZO were used to model Al-LLZO. Two hydrogarnet models were used for Nb- and Ta-LLZO. A moderate expansion is observed for Al-LLZO. Surprisingly, the cell volume hydrogarnet phase with the larger lattice parameter is declining in Nb- and Ta-LLZO whereas the cell volume of the phase with the smaller lattice parameter does not change. The data quality is impaired by the impurity phases contained in these samples.
W-LLZO is expanding during heating. With eq. 26 according to Hubaud et al., a thermal expansion coefficient α can be calculated as a function of the lattice parameter a and
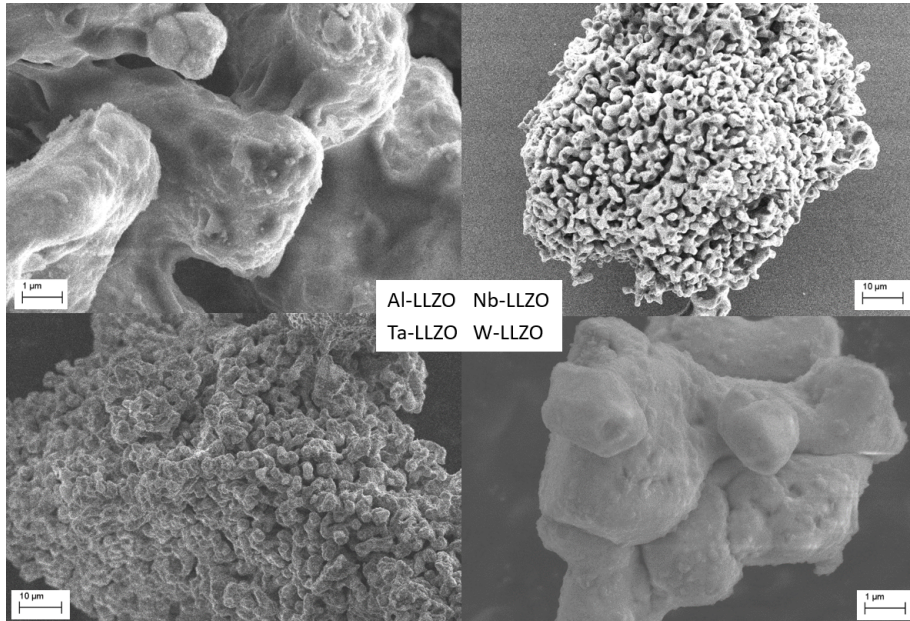
Figure 48 – SEM micrographs of of synthesized Al-, Nb-, Ta-, and W-substituted LLZO.
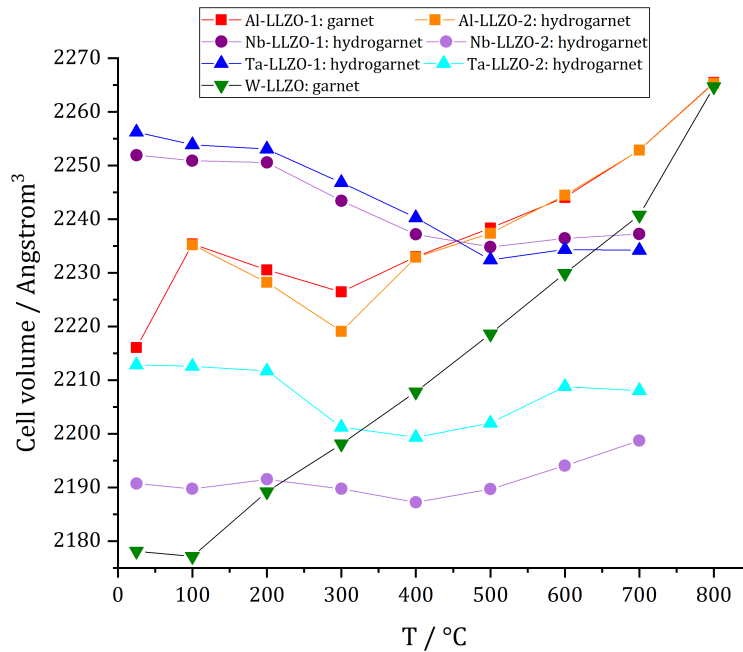

Figure 49 – Thermal expansion of Al-, Nb-, Ta-, W-substituted LLZO evaluated with Rietveld refinement.

the temperature T.[71]

$$\alpha = \frac{\Delta a/a}{\Delta T} \tag{26}$$

A thermal expansion of $16.66 \cdot 10^{-6}$ K^{-1} is calculated from 25 to 700 °C for W-LLZO. Hubaud et al. report $15.498 \cdot 10^{-6}$ K^{-1} for Al- substituted LLZO. Compared to other garnet materials as $Y_3FeGa_4O_{12}$ and $Ca_2LaZr_2Ga_3O_{12}$, the thermal expansion of LLZO is twice as high.[71]

Al-LLZO is stable up to 700 °C, Nb- and Ta-LLZO up to 500 ° C and W-LLZO up to 600 °C. The thermal stability of the material is presumably reduced in the capillary measurement by diffusion of the Li into the glass.

5.9. Chemical stability against solvents

Chemical stability of LLZO regarding processing with different solvents was investigated with powder diffraction. The results are shown in Fig. 50. The following solvents were tested to see, if LLZO undergoes a chemical reaction: Acetic acid, Aceton, 2-Propanol, Ethanol, Ethyl acetate, hexane, acetonitril, water. Apparently, LLZO is stable against all
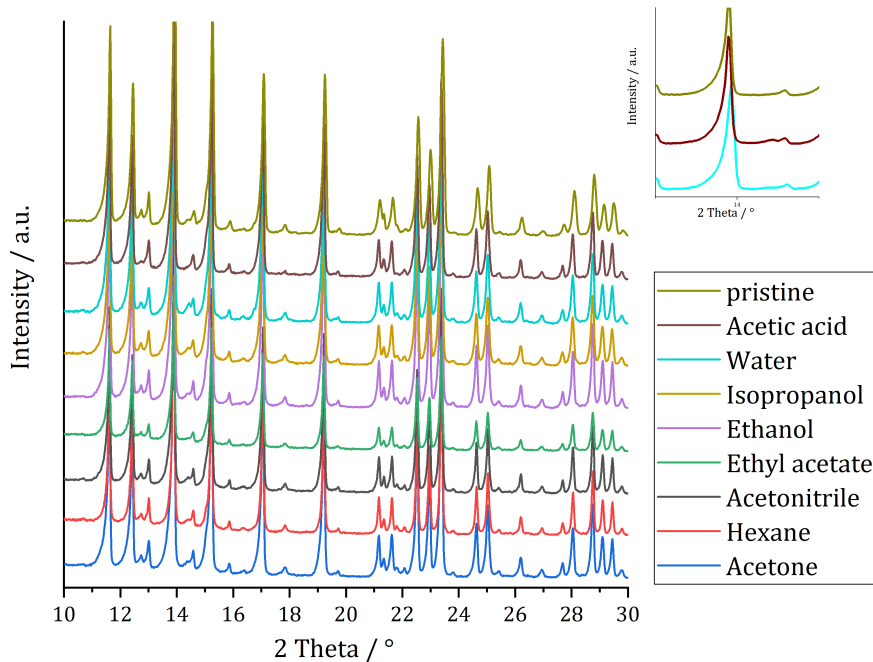

Figure 50 – Powder diffraction patterns of commercial Al-LLZO after treatment with different solvents for 1h and 60 °C, and pristine for comparison.

tested sovents as there are no shifts of reflections observed and no reflections of impurity phases appear. The material did not undergo a forced H$^+$- exchange with acetic acid which would cause a change of the lattice parameter.[102] A Li$^+$-exchange is therefore

excluded as a reason for the observed peak superposition with X-ray diffraction in the commercial Nb- and Ta- substituted hydrogarnet samples.

The storage time and temperature in the solvent is comparably low in this study. Kun et al. observed a change of the lattice parameter of cubic Al-LLZO after treatment with polar protic and aprotic solvents after two weeks storing LLZO in the solvent.[102] They conclude that acetonitrile is the best choice as dispersion medium for LLZO.

5.10. Conclusion and Outlook

The formation of a hydrogarnet structure starting from garnet LLZO with Al, Nb, Ta, and W substitution is investigated with XRD, NPD, total scattering PDF, ^{6}Li and ^{27}Al MAS NMR. Ball milling transforms the higher symmetric garnet structure to the hydrogarnet structure and thermal annealing causes the reverse effect. The formation of the hydrogarnet structure does not seem to depend on the substituting cation. The two crystal structures can be distinguished by diffraction methods due to the symmetry reduction $Ia\bar{3}d$ to $I\bar{4}3d$, i.e. a loss of the threefold inversion axis in the hydrogarnet structure. PDF analysis shows a distortion of the octahedral MO_6 (M = Al, Zr, Nb, Ta, W) coordination in the hydrogarnet. With ^{6}Li MAS NMR, two different local environments of Li in the hydrogarnet structure are observed, and one in the garnet, as expected from the XRD and NPD results. The hydrogarnet structure offers an additional Li site that is highly occupied and therefore is supposed to slow down the long-range Li transport. The mobility of Li in the hydrogarnet structure was measured on different time/length scales from single local jumps to bulk and long-range conductivity with ^{7}Li NMR and impedance spectroscopy. Both T_1 relaxation and motional line narrowing demonstrate that the hydrogarnet structure causes a lower mobility of Li on short time scales. PFG NMR indicates a lower long-range mobility in the hydrogarnet structure.

The criteria of chemical stability against solvents, temperature stability and expansion, which are important for processing, were examined with diffraction. No impurity phase formation occurs with polar protic solvents during stirring at 60 °C for 1 h. There is no evidence of an H^+ exchange. The thermal expansion of the W-LLZO is in good agreement with literature values for Al-LLZO.

In order to evaluate the long-range conductivity of Li in the hydrogarnet structure, an approach without a sintering step is required to exclude the conversion of $I\bar{4}3d$ to $Ia\bar{3}d$. For this purpose, the LLZO could be incorporated into a polymer matrix. This is examined in the following chapter.

6. Long-range Li$^+$ transport in LLZO-based polymer composite solid electrolytes

Composite electrolytes can combine the advantages of single electrolyte materials. This is particularly useful to embed an inorganic electrolyte with a high ionic conductivity into a polymer matrix and renounce the sintering step of the former.

It has been described in the previous chapter that LLZO undergoes a phase transformation from hydrogarnet to garnet structure during sintering. Because of this phase transformation, it was not possible to measure the long-range ionic transport with impedance spectroscopy. Further, it was not possible to measure the diffusion coefficient of hydrogarnet samples with PFG-NMR.

6.1. Aim of the work

In this chapter, a composite is introduced that combines the high ionic conductivity of LLZO with the facile fabrication to thin films with polyethylene oxide without thermal treatment.

The long-scale mobility in the hydrogarnet structure is to be investigated via incorporation of the material into a polymer matrix. A composite electrolyte with the same composition is fabricated with garnet-structured LLZO for comparison.

Additionally, the question is addressed whether any ceramic particles in a polymer composite without bulk Li conductivity would enhance the conductivity of a composite. The contributions to charge transfer at heterogeneous polymer-ceramic interfaces were tested with of temperature-dependent NMR spectroscopy and impedance spectroscopy. For comparison, tests were also carried out on commercial LLZO-containing and purely polymer-based composite electrolytes.

6.2. X-ray powder diffraction

Crystalline cubic Nb-substituted LLZO in garnet and hydrogarnet structure is previously described in chapter 5.2. The lattice parameter changed from 13.107 (49 wt-%) and 12.988 (46 wt-%) Å of the (unsintered) hydrogarnet sample to 12.927 Å after sintering. The hydrogarnet structure converts into garnet. The refinement of the sintered sample is shown in Fig. 51. The refinement of the unsintered sample is depicted in Fig. 30 in chapter 5.2.
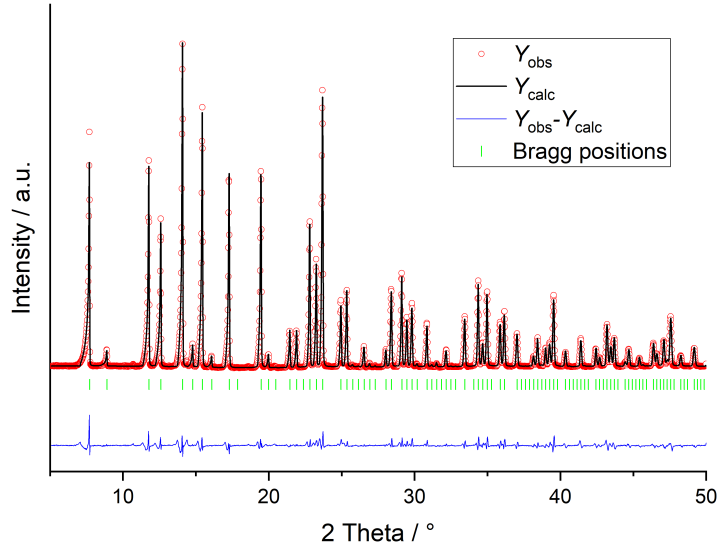
Figure 51 – Rietveld refinement against diffraction pattern (Mo K$_{\alpha1}$) of sintered commercial Nb-LLZO.

6.3. Ionic mobility and conductivity

Fig. 52 a) shows impedance spectra of the hydrogarnet-composite electrolyte recorded in a temperature range from 5 to 65 °C and a 10 degree interval. The electrolyte resistance was determined by extrapolation of the left semicircle to the x-axis. The ionic conductivity was calculated using eq. 19. The temperature dependent ionic conductivities were plotted against the inverse temperature in Fig. 52 b).

Conductivities of $1.2 \cdot 10^{-6}$ S·cm^{-1} at 25 °C were measured for the hydrogarnet-composite and $3.4 \cdot 10^{-6}$ S·cm^{-1} at 25 °C for the garnet-composite with impedance spectroscopy, as shown in Fig. 52 and 53. The thickness of the electrolytes was 0.01125 mm for the hydrogarnet-composite and 0.02725 mm for the garnet-composite.

The values are comparable with those reported in literature given that many specifications for conductivity are measured at higher temperatures. [85,109,188,193]

With pulse-field gradient ^{7}Li NMR measurements (Fig. 54), diffusion coefficients of $6.1 \cdot 10^{-14}$ m^2 s^{-1} for the LLZO-garnet composite electrolyte at 25 °C and $1.1 \cdot 10^{-14}$ m^2 s^{-1} for the LLZO-hydrogarnet composite electrolyte were measured at 25°C. Since the concentration of Li ions in the composite cannot be quantified precisely, no ionic conductivity can be calculated as for a crystalline compound. Though, the diffusion coefficients can be directly compared: The Li diffusion coefficient is higher in the garnet-composite. The activation energy of Li diffusion in the garnet composite is measured with impedance spectroscopy and PFG NMR. An activation energy of Lithium diffusion is calculated with an Arrhenius approach according to equation 25. The activation energy is calculated to 1.0 eV for the garnet and 1.1 eV for the hydrogarnet structure.

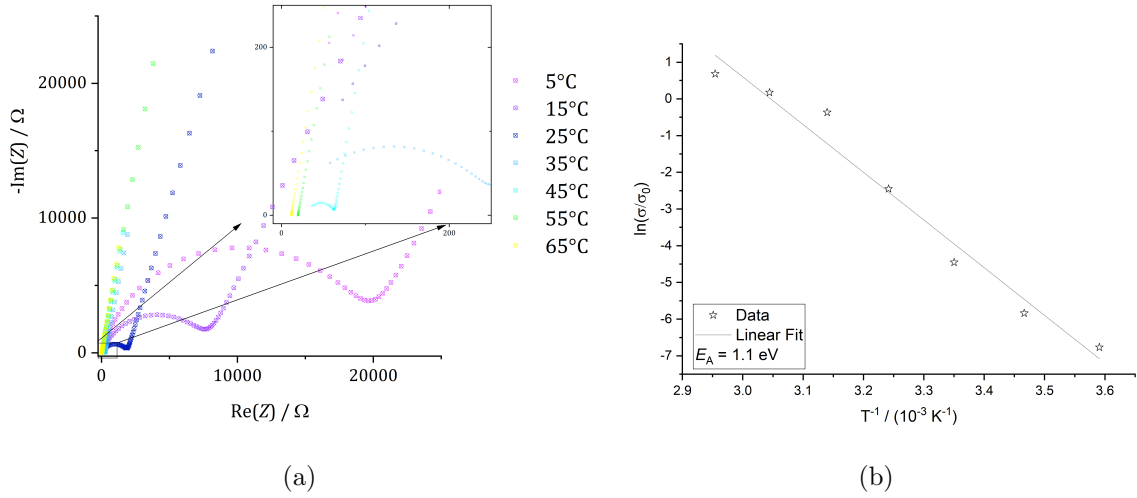In case that diffusion through the polymer predominately controls the ion movement,

74

Figure 52 – a) Nyquist plot of impedance spectra of LLZO-hydrogarnet composite electrolyte from 5 to 65 °C, b) Arrhenius fit of conductivities. The gray line shows a linear fit according to equation 25.

the temperature dependency can be better described with the Vogel-Fulcher-Tamman equation 23. The curve of the hydrogarnet composite is flattened, so we use an VTF approach, too.[36] Eq. 23 is linearized to eq. 27.

$$\ln\left(\frac{\sigma}{\sigma_0}\right) = -\frac{E_A}{k_B \cdot (T_V - T_0)} \tag{27}$$

The temperature dependence of the LLZO composite can be mapped with an Arrhenius approach. The fact that this no longer applies to the hydrogarnet composite can be seen as an indication that the hydrogarnet does not contribute to the conductivity of the composite, in consequence the conductivity of the hydrogarnet can be suspected to be lower. The same can be seen in PFG-NMR. The activation energy determined with the VTF-approach lies significantly below at 0.78 eV. This number refers mainly to ion transport through the polymer and not the composite or the ceramic.

In addition to the impedance measurements, the lithium mobility is evaluated with PFG-NMR for both composites as depicted in Fig. 54. The echo damping I/I_0 as a function of the gradient strength g can be well described with a Gaussian function, as expected from the Stejskal-Tanner equation.[162] The activation energy of the garnet-based electrolyte is quantified to 1.0 eV and that of the hydrogarnet-composite to 1.2 eV.
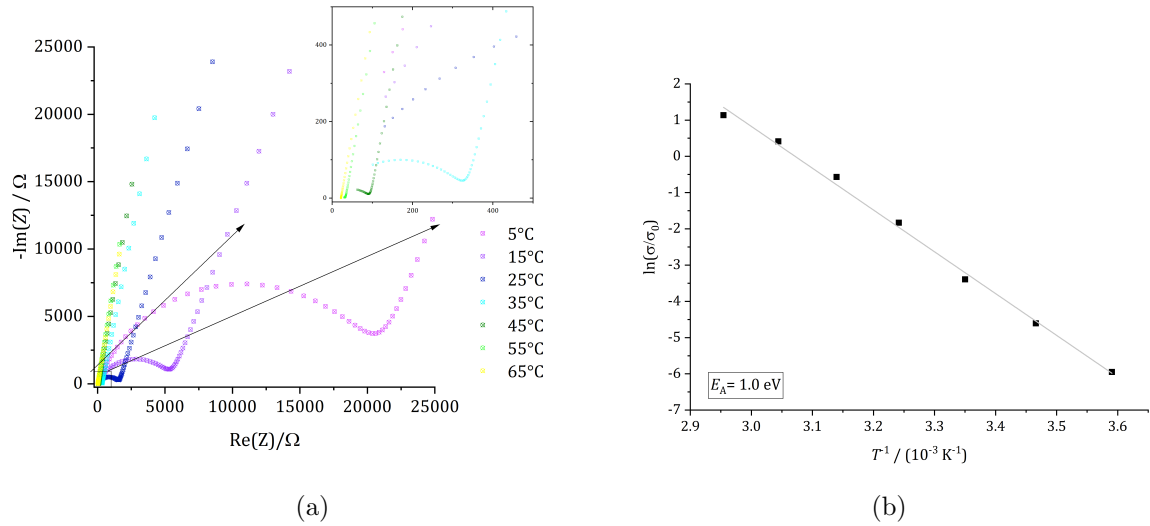
(a)

(b)

Figure 53 – a) Nyquist plot of impedance spectra of LLZO-garnet composite electrolyte from 5 to 65°C, b) Arrhenius fit of conductivities. The grey line shows a linear fit according to equation 25.
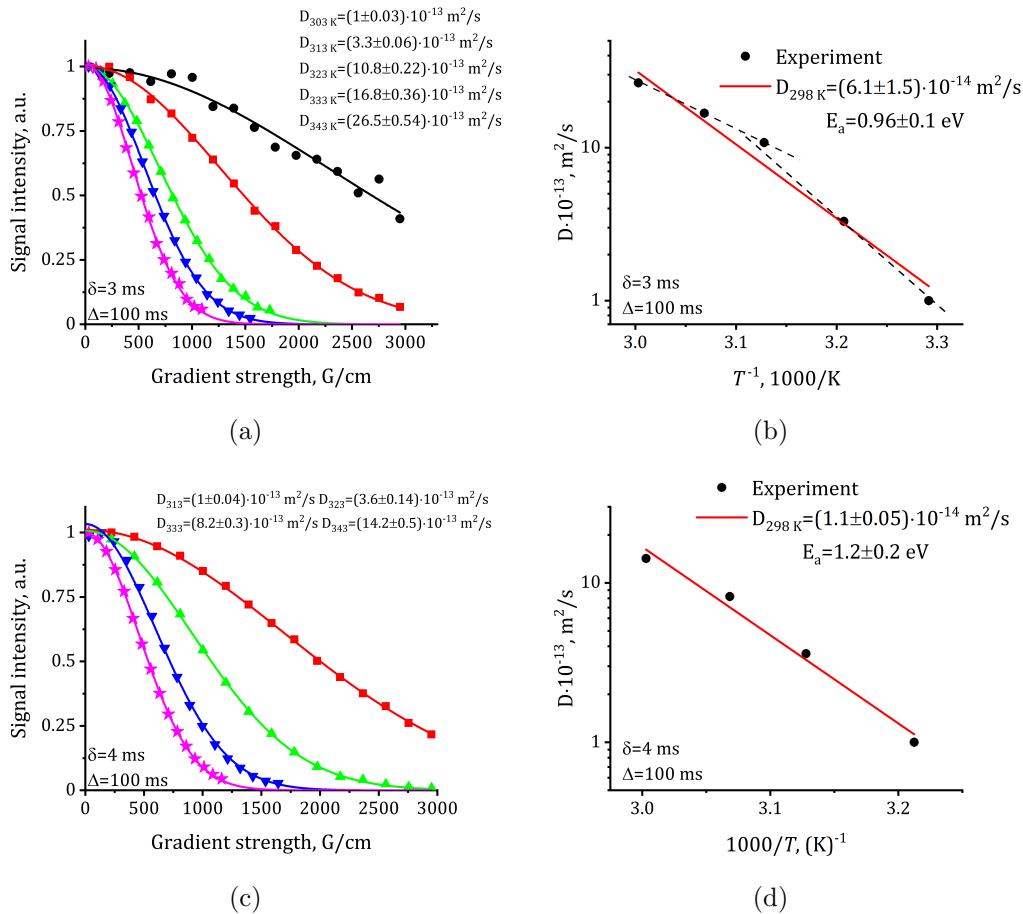

(a)

(b)

(c)

(d)

Figure 54 – a) Signal intensity vs. gradient strength for LLZO-garnet composite electrolyte, b) + d) Arrhenius fit of conductivities for garnet-based (b) and hydrogarnet-based (d) electrolyte. The red line shows a linear fit according to equation 25. c) Signal intensity vs. gradient strength for LLZO-hydrogarnet composite electrolyte

76

6.4. Blind tests without ceramic component and SiO$_2$ particles

A polymer-salt electrolyte PEO(LiTFSI) without a ceramic component is fabricated and a conductivity of $8.7 \cdot 10^{-7}$ S cm^{-1} (25 °C) is measured with impedance spectroscopy. The thickness of this electrolyte is 0.0795 mm. The corresponding Nyquist plots and Arrhenius fit are depicted in Fig. 55. Both conductivity but also activation energy of diffusion (0.8 eV) are lower than with LLZO ceramic. To evaluate the contribution of the ceramic to the conductivity, the impedance of a PEO-LITFSI composite with SiO$_2$ particles was measured, too, see Fig. 56. Here, the conductivity is determined to $1.17 \cdot 10^{-5}$ S cm^{-1} (25°C, layer thickness 0.0899 mm) with an activation energy of diffusion of 0.6 eV.

Tab. 11 gives an overview about the results of the conductivity measurements. The ceramic component has a significant influence on the conductivity.
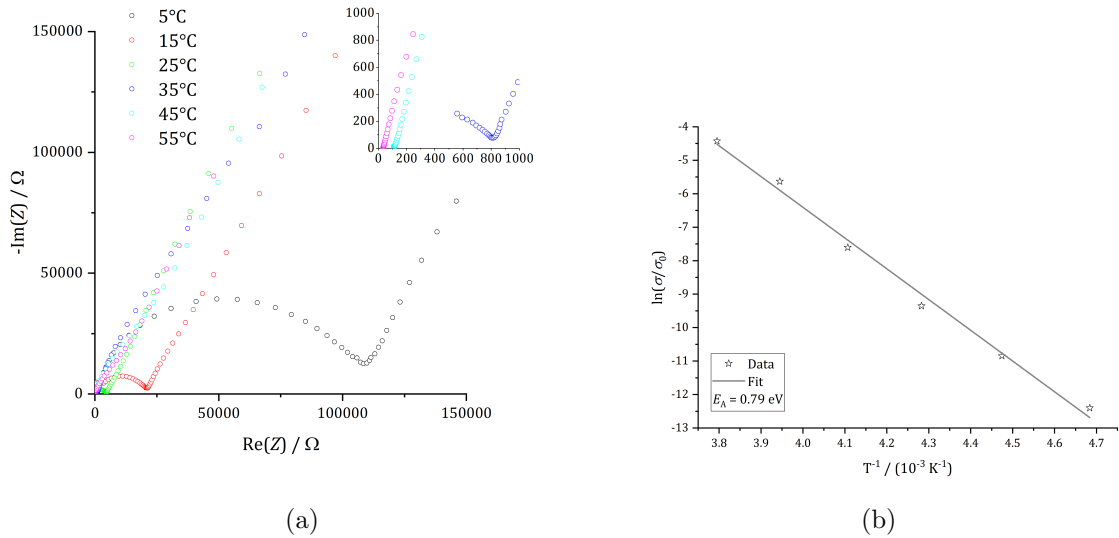

Figure 55 – a) Nyquist plots of impedance measurements at different temperatures of a PEO-LITFSI electrolyte, b) corresponding Arrhenius fit.

6.5. Commercial composite and polymer electrolytes

The LLZO-containing electrolyte nanomyte SE50 has a highly viscous and sticky texture. It is delivered as a white paste as photographed in Fig. 84 a). XRD proves that nanomyte SE50 contains crystalline LLZO although the manufacturer specifies its amorphous structure, see Fig. 57 a). It is also very likely that the sample contains LiTFSI which can be traced back by the Raman spectrum shown in Fig. 58. The polymer-component is very likely polyethylene-oxide. This can be deduced from the infrared spectrum shown in the appendix in Fig. 86. A thermogravimetric analysis is shown in Fig. 85. A conductivity of $5.8 \cdot 10^{-5}$ S cm^{-1} is measured at 25°C in nanomyte SE50 and

Table 11. – Total conductivities and activation energies of polymer composite electrolytes at 25 °C.

Sample	Total conductivity / S·cm^{-1}	Activation energy / eV
LLZO Garnet – PEO- LiTFSI	$3.4 \cdot 10^{-6}$	1.0
LLZO Hydrogarnet – PEO- LiTFSI	$1.2 \cdot 10^{-6}$	1.1 (Arrhenius) / 0.8 (VTF) 1.2 (PFG-NMR)
PEO-LiTFSI	$8.7 \cdot 10^{-7}$	0.8
SiO$_2$- PEO-LiTFSI	$1.2 \cdot 10^{-5}$	0.6
Commercial *nanomyte-SE50*	$5.8 \cdot 10^{-5}$	0.3
Commercial *H-Polymer*	$1.8 \cdot 10^{-6}$	0.6

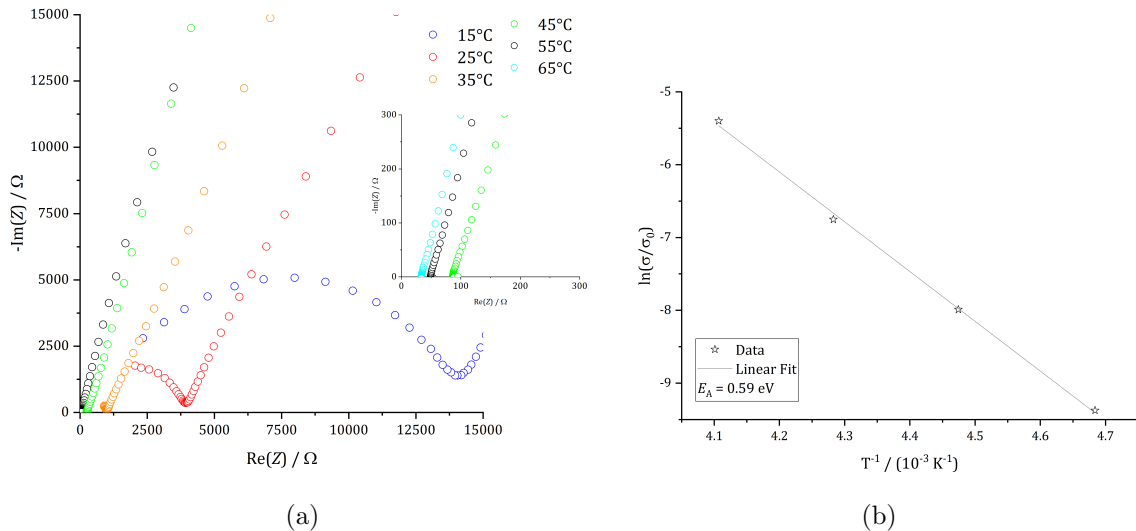(a)   (b)

Figure 56 – a) Nyquist plots of impedance measurements at different temperatures of a PEO-LITFSI electrolyte with SiO$_2$, b) corresponding Arrhenius fit.

an activation energy of diffusion of 0.3 eV with impedance spectroscopy. The activation energy of Li diffusion in nanomyte SE50 is quantified with PFG-NMR to 0.5 eV.

In a direct comparison of the SEM micrographs of the commercial and the garnet-composite electrolyte one can see a more homogeneous distribution of the ceramic in the polymer matrix for the commercial sample. Indeed, this could be an explanation for the lower conductivity of the in-house synthesized composite although they both are supposed to consist of the same components.

The commercial electrolyte H-Polymer is also specified to be amorphous which is confirmed with an XRD measurement, see Fig. 57. The Raman spectrum in Fig. 58 shows similarities with the spectrum of the PEO. However, reliable statements about the composition cannot be made. Its structure is sticky and highly viscous, too. It exhibits a

conductivity of $1.8 \cdot 10^{-6}$ S cm^{-1} (25 °C) and an activation energy of 0.6 eV measured with impedance spectroscopy. PFG-NMR confirms the measured activation energy of 0.6 eV. The data of the PFG measurements of the commercial electrolytes are shown in the appendix in Fig. 81 and 82.

The Li diffusion coefficient of nanomyte SE50 is $2.6 \cdot 10^{-13}$ m^2 s^{-1} and the Li diffusion coefficient of H-Polymer is $5.3 \cdot 10^{-14}$ m^2 s^{-1} (both values at 25°C). Nanomyte SE50 which contains LLZO, exhibits a higher mobility of Li ions than H-Polymer. This confirms our results that the ceramic components enhances the conductivity significantly.
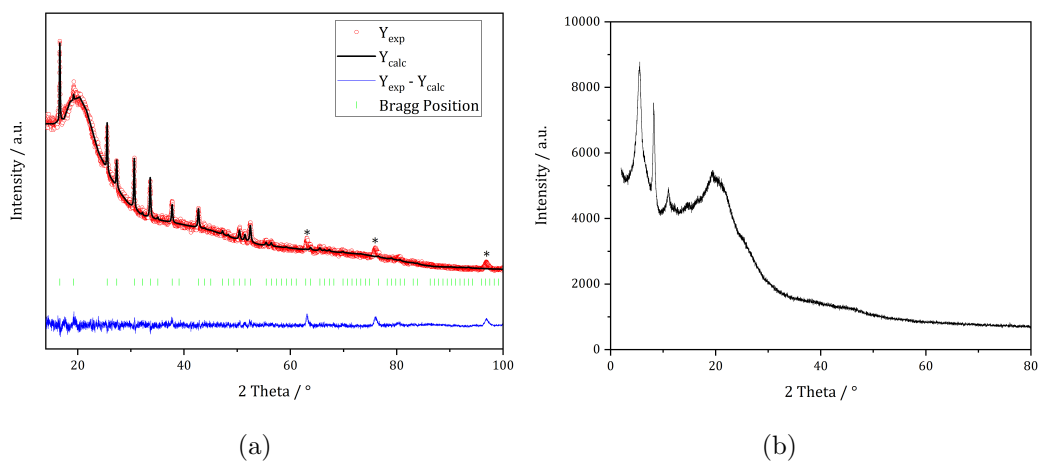

(a)   (b)

Figure 57 – a) Rietveld refinement against X-ray diffraction pattern (Cu K$_{\alpha 1}$) of the commercial electrolyte nanomyte SE50. The peaks marked with an asterisk stem from the sample holder. The high contribution of diffuse scattering can be attributed to the polymer content, b) X-ray diffraction pattern (Cu K$_{\alpha 1}$) of the commercial electrolyte H-Polymer.
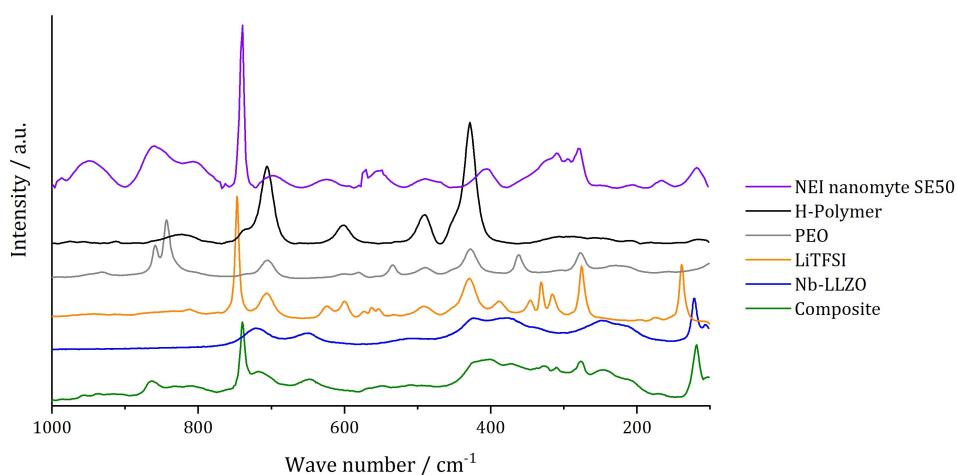

Figure 58 – Raman spectra of commercial electrolytes nanomyte SE50, H-polymer, composite electrolytes and PEO, LiTFSI, LLZO reference spectra.
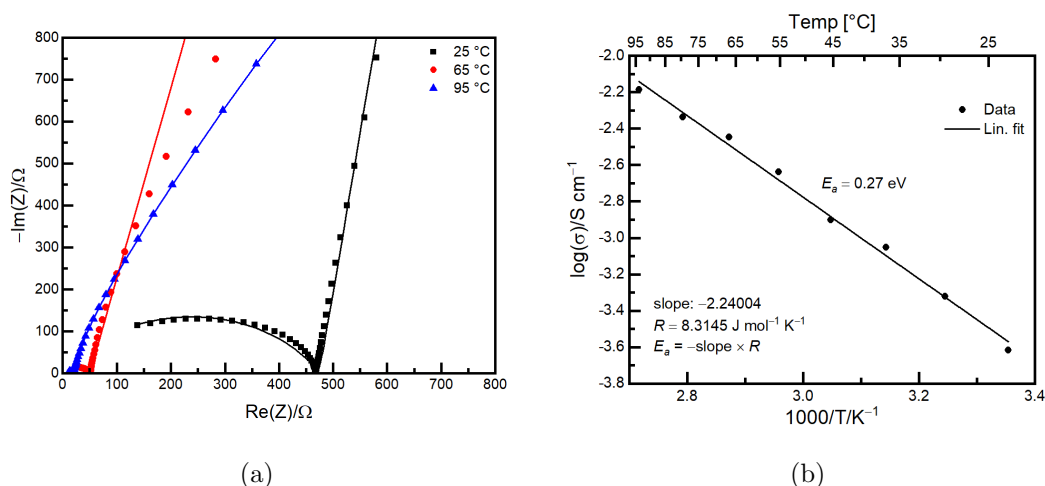
Figure 59 – a) Nyquist plots of impedance measurements at different temperatures of commercial electrolyte nanomyte SE50, b) corresponding Arrhenius fit.

6.6. Conclusion and Outlook

The facile synthesis of composite electrolytes starting with LLZO, polyethylene oxide and LiTFSI without thermal sintering could be demonstrated in this chapter. By using the polymer and the conductive salt, however, the conductivity is reduced by two orders of magnitude to 10^{-6} S cm^{-1} compared to pure LLZO.

The ionic conductivity of the hydrogarnet modification could be investigated and compared to the garnet modification incorporated in the same polymer matrix. With PFG-NMR and EIS it could be shown independently that the long-range Li$^+$ conductivity or diffusion in the hydrogarnet structure is subject to the garnet structure. These results are confirmed by measuring the activation energy of diffusion with both EIS and PFG-NMR. A higher activation energy of lithium diffusion of 1.1 eV is measured in the hydrogarnet composite, compared to 1.0 eV in the garnet composite. The temperature-dependent conductivity of the hydrogarnet composite shows predominant characteristics of a polymer, not of a crystalline electrolyte.

The conductivity of the garnet-based composite electrolyte and that of a commercial, purely polymer-based electrolyte H-Polymer is in the range of 10^{-6} S cm^{-1}. The conductivity is subject to an LLZO-containing commercial electrolyte which is $5.8 \cdot 10^{-5}$ S cm^{-1}. The difference can be traced back to morphological differences, as the various components in commercial electrolytes have smaller particle sizes. The characterization of the commercial electrolytes could be completed by DSC measurements, ^{1}H and ^{13}C NMR measurements.

High conductivities could also be achieved with a non-lithium-conductive ceramic SiO$_2$-based composite electrolyte, probably due to a decreased crystallinity of the ceramic as previously reported in literature[86,113,172,197].

7. Interface and morphology of LLZO-NCM catholytes

The development of solid-state batteries continues to advance. The focus is shifting from optimizing a single material to an entire cell, where compatibility plays an important role. This applies not only to the chemical compatibility of the two materials at the interface, but also to the processing where high temperatures or mechanical forces can be applied. Usually, the greatest possible contact of two materials is desired to improve the diffusion. Electrochemical barriers for diffusion route of the lithium should be prevented as far as possible. There are many different materials as candidates for cathode active materials for ASSB. Though being highly conductive for Li ions, thiophosphates have proven to be unstable towards the cathode material NCM.[20,91,204,208] LATP is also electrochemically unstable, as the titanium contained can be reduced on a Li metal anode. Therefore, we want to focus on LLZO as an electrolyte. Al and Nb are chosen as abundant and inexpensive substituents to stabilize the cubic structure of LLZO.

These studies are also necessary with a view to coating NCM with LLZO using a thiophosphate separator. A battery could be fabricated with LLZO-coated NCM and a thiophosphate electrolyte as separator.
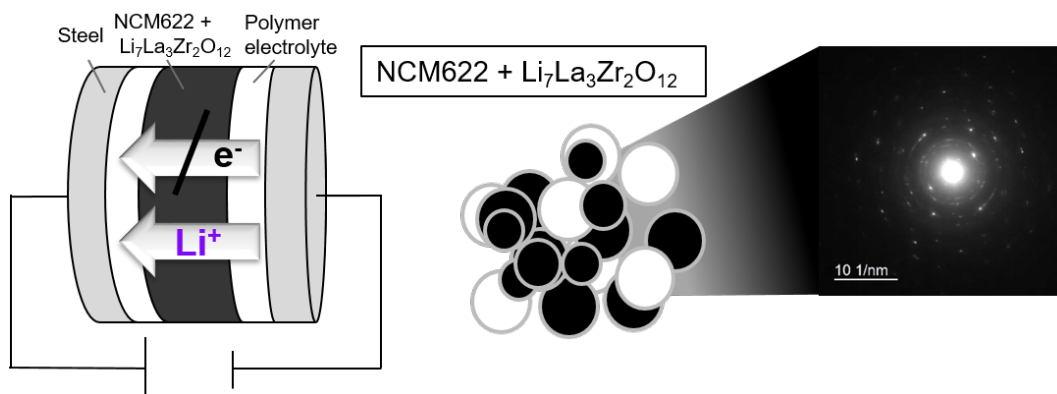

Figure 60 – Principle of measurement of the catholyte composite sandwiched between two layers of an auxiliary electrolyte to separate ionic from electrical conductivity extended by morphological investigations.

7.1. Aim of the work

With the chosen approach, a LLZO-NCM interface is examined concerning Li ion diffusion barriers. NCM is chosen as the cathode active material (CAM) because of its low cobalt content.[138]

X-ray diffraction and ^{6}Li MAS NMR are utilized to analyze the crystal on local structure and exclude impuritites. A closer look on the morphology of the composite is taken with

TEM. An impedance spectroscopy-based approach is used to access the Li diffusion. The use of an auxiliary electrolyte (a.e.) aims to separate the Li^+ from the total conductivity. The sandwiched catholyte is measured with impedance spectroscopy to extract a conductivity. These measurements are performed at different temperatures to calculate an activation energy of conductivity. Two differently substituted LLZO materials are used for the catholyte composites with the promising substituents Al and Nb. Each of them is examined in two ratios, LLZO:NCM 0.5:8 and 1:1. The 0.5:8 ratio is supposed to mimic a realistic catholyte composition based on ratios that have already been published.[176] In a 1:1 mixture the contributions of each phase can be examined better.

7.2. Structural analysis

The diffraction data of the catholyte composites is depicted in Fig. 61. The refinement confirms that the catholyte composite consists of cubic LLZO and NCM. No formation of impurity phases happens during ball milling. LLZO, however, as demonstrated in chapter 5, is prone to form the hydrogarnet modification by mechanically treatments such as ball milling. The formation of significant amounts as listed in Tab. 12 is observed, even though using small amounts of LLZO in the 0.5:8 ratio. More hydrogarnet forms for the Nb-substituted LLZO in comparison to Al-LLZO.

7.3. Local structure of Li

Fig. 62 presents the ^{6}Li MAS NMR spectrum of the ball milled catholyte composite Al-LLZO-NCM622 1:1. LLZO gives a signal at 0.6 ppm. The signal is broadened, so no contributions from garnet or hydrogarnet as for the pure LLZO can be evaluated (see chapter 5.3., Fig. 33).
NCM622 has a broad signal from -1100 to 100 ppm.

Table 12. – Hydrogarnet formation in catholytes as revised by Rietveld refinement.

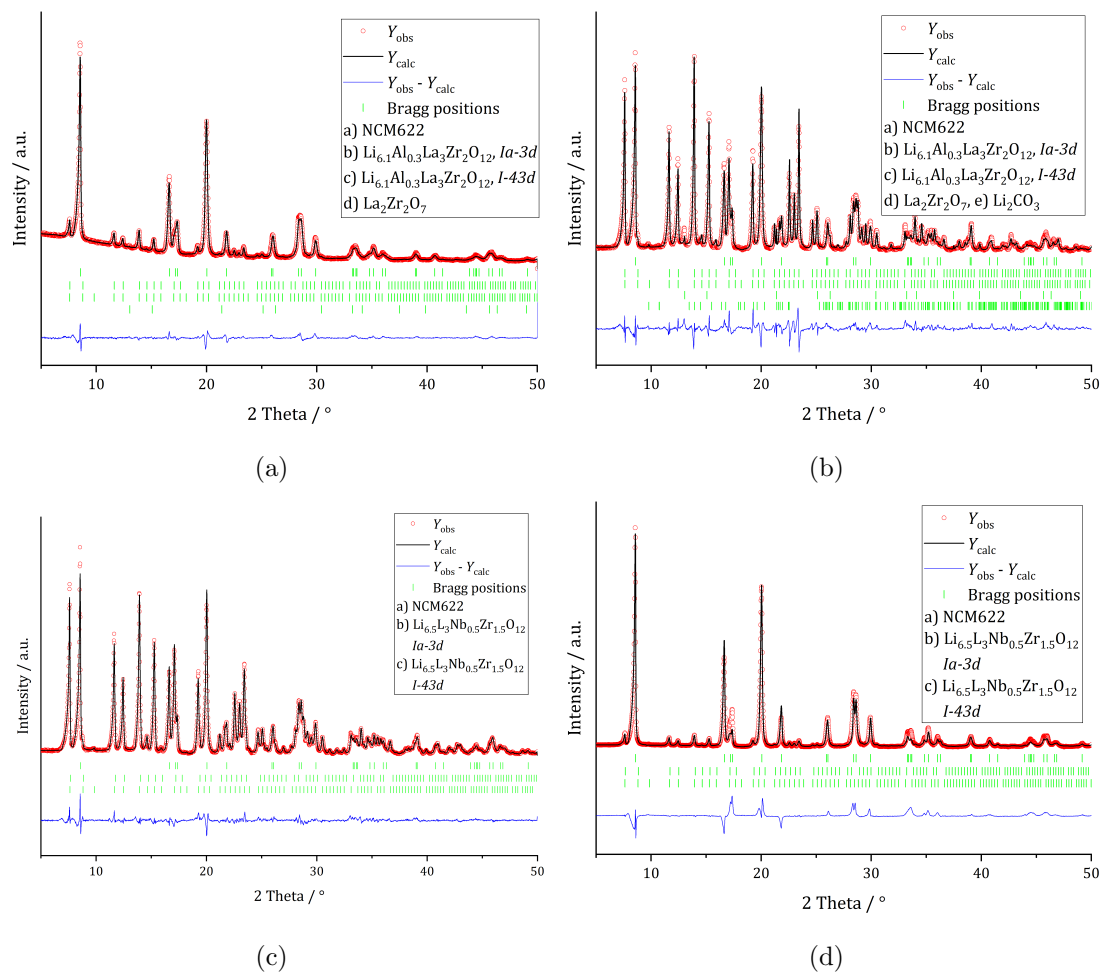| Sample	wt-% Hydrogarnet of total LLZO
Al-LLZO-NCM622 0.5:8	22%
Al-LLZO-NCM622 1:1	30%
Nb-LLZO-NCM622 0.5:8	88 %
Nb-LLZO-NCM622 1:1	67 %

Figure 61 – Rietveld refinements against Mo K$_{\alpha 1}$ diffraction patterns of a) 5.88 wt-% Al-LLZO/NCM b) 50.0 wt-% Al-LLZO/NCM c) 5.88 wt-% Nb-LLZO/NCM d) 50.0 wt-% Nb-LLZO/NCM at 25 °C.
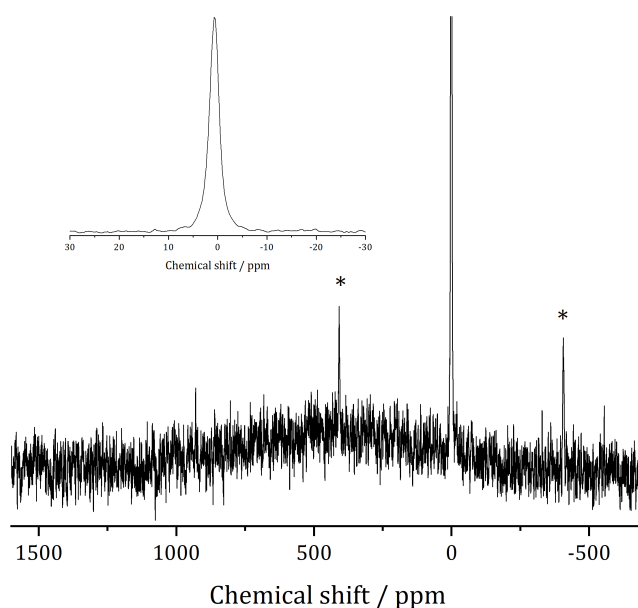
Figure 62 – ^{6}Li MAS NMR spectrum of the ball milled catholyte composite Al-LLZO-NCM622 1:1.

7.4. Morphology

The morphology of an Al-LLZO-NCM622 catholyte with a 0.5:8 (wt-%) composition is investigated exemplary with TEM, STEM and ED. SEM micrographs of pure NCM622 are used for a comparison.

Small LLZO particles form on the larger NCM particles as observed in Fig. 63 and 67. The formation of a core-shell like structure that is proclaimed to form after ball milling by Zhang et al. is contradicted.[112]

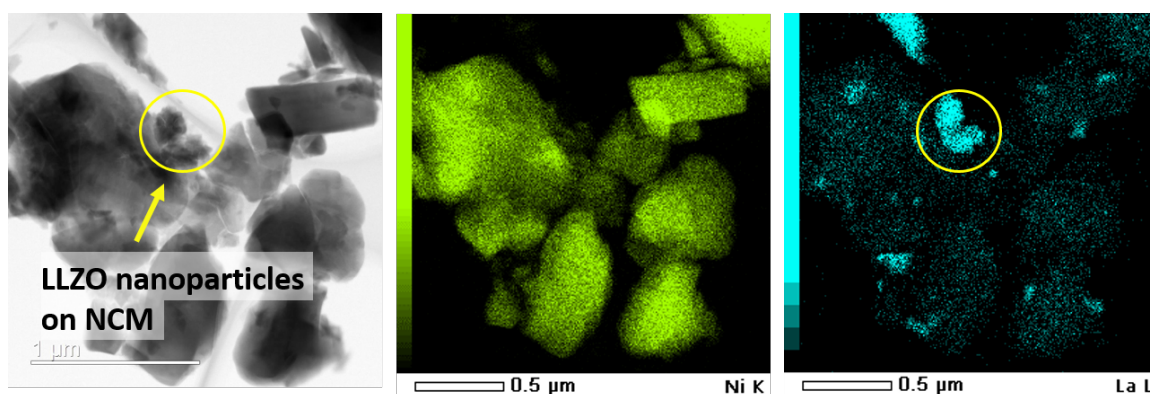NCM particles appear much larger with a smoother surface and the LLZO material a

Figure 63 – LLZO nanoparticles on NCM observed with STEM-TEM.

little more porous in comparison. The diameter of NCM particles is estimated to 1 µm and LLZO 0.2 µm. Thus, the particles size of LLZO shrinked during ball-milling com-
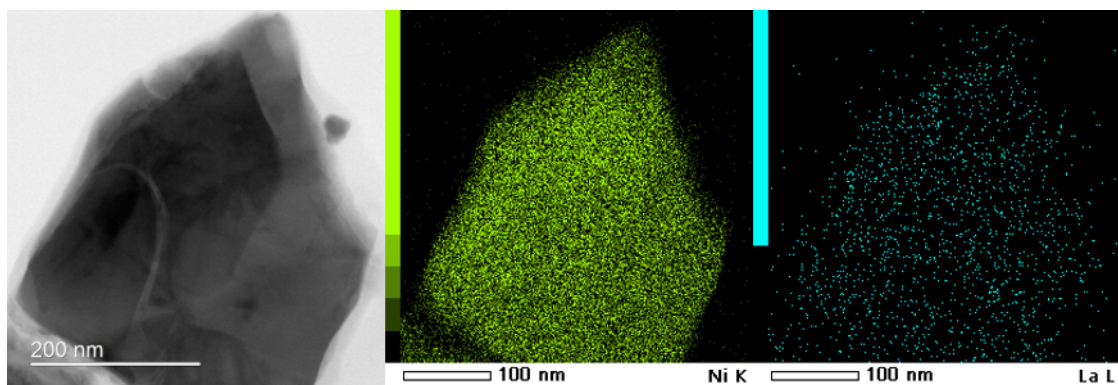
Figure 64 – NCM particle in LLZO-NCM catholyte
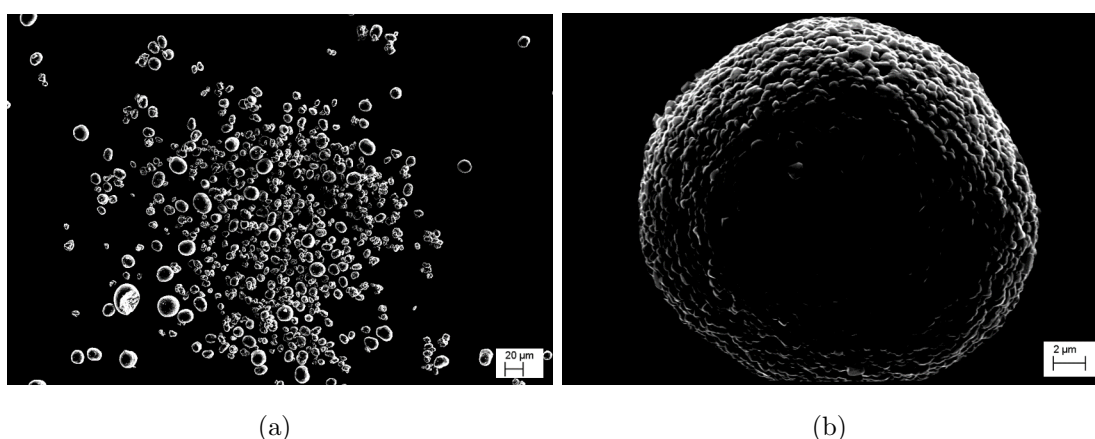

(a)   (b)

Figure 65 – Particle morphologies of NCM622 observed with SEM.

pared to SEM micrographs.

With SEM, striking spherical NCM622 particles are observed in the commercial material as in Fig. 65. Strauss et al. tested very similar spherical NCM particles with the result that particles with a diameter smaller than 10 µm yield the highest capacities.[167] With TEM micrographs after ball milling as shown in Fig. 64, the spherical shape of the particles cannot be observed anymore. This is suspected to be due to the harsh mechanical treatment or the higher resolution of the TEM compared to SEM. In Fig. 66, large area amorphous domains and two distinct interfaces can be observed, each of approximately 2.5 nm.

Fig. 67 shows that ball milling did not result in direct contact between the two materials. This must therefore be produced by external pressure. Relatively large voids can be seen.

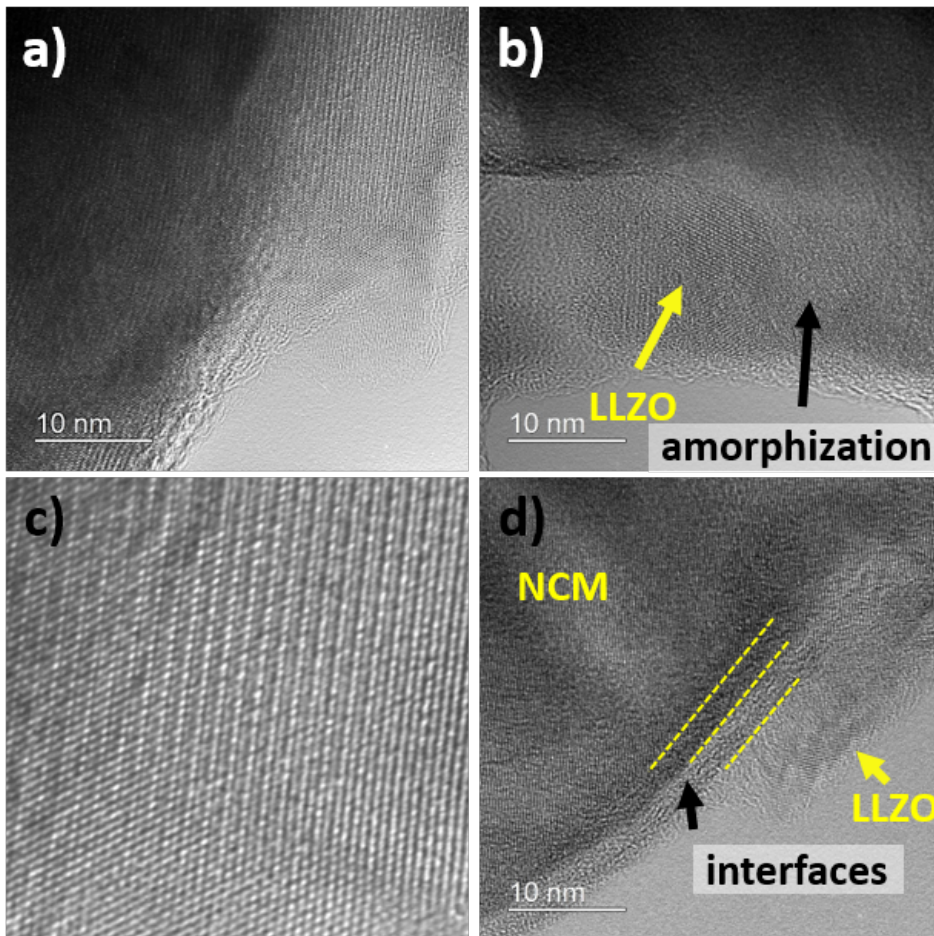The examined area can be assigned to NCM by simulating selected area electron diffraction (SAED).

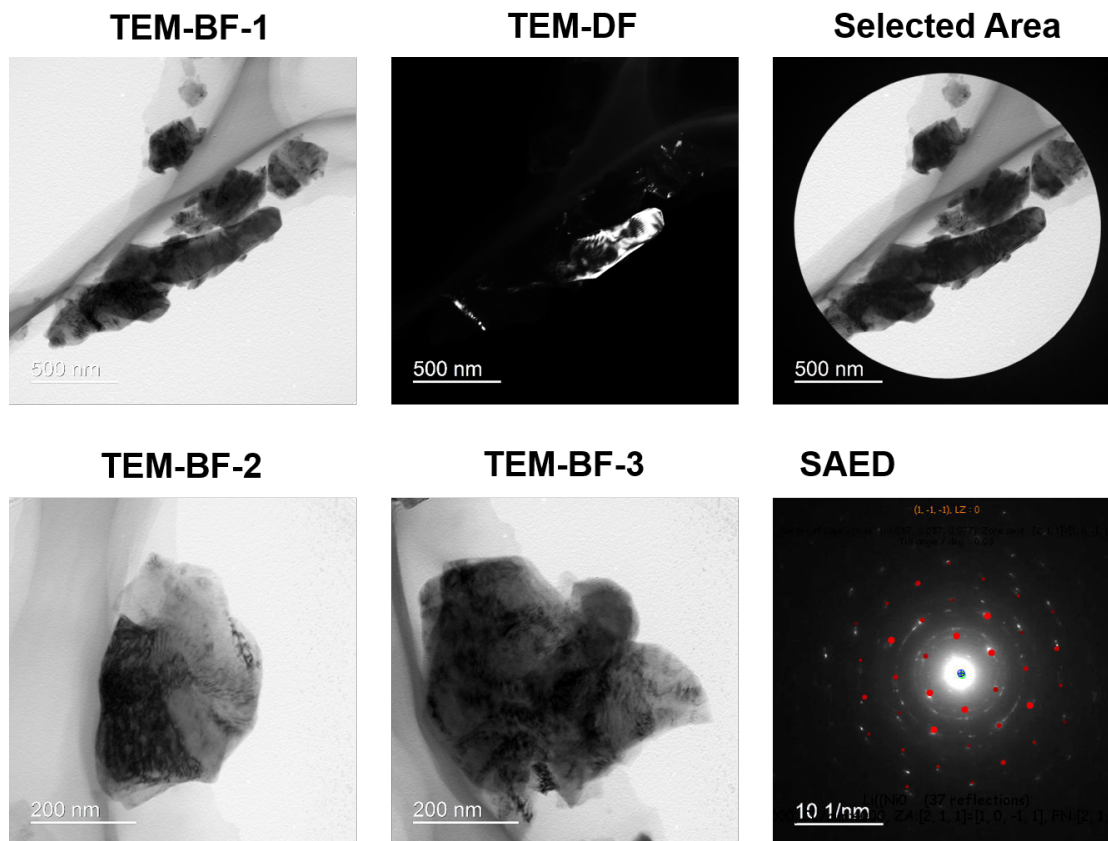**Figure 66** – Interfaces between LLZO and NCM observed with HR-TEM.

TEM-BF-1   **TEM-DF**   **Selected Area**

TEM-BF-2   **TEM-BF-3**   **SAED**

Figure 67 – Bright field, dark field and SAED micrographs. SAED simulation with NCM622.

7.5. Electrochemical characterization

The catholyte composites are pressed to pellets and sandwiched between two layers of an auxiliary electrolyte and measured with impedance spectroscopy, as illustrated in Fig. 60, to separate ionic conductivity from electrical conductivity. The auxiliary electrolyte is a LLZO-PEO-LiTFSI composite electrolyte that is characterized in chapter 6 and possesses a layer thickness of less than 0.03 mm. Its total conductivity is quantified with impedance spectroscopy to $3.4 \cdot 10^{-6}$ S cm^{-1}. The fabrication of this electrolyte is described in chapter 9.1.7.

Catholyte pellets without auxiliary electrolyte layers are used as a reference. Four different catholyte compositions are investigated in total; based on Al- or Nb-substituted, garnet-structured, LLZO with each two different compositions of 0.5:8 and 1:1 (wt-%). With this two different weight ratios, a realistic catholyte composition is modeled with 0.5:8 on the one hand, and the contributions of each component is investigated with 1:1, on the other hand. Further, the contribution of the electrical conductivity to the total conductivity is supposed to be higher for the 0.5:8 composition whereas the ionic conductivity is supposed to contribute more to the total conductivity of the 1:1 composition. NCM622 is pressed to a pellet and analyzed with impedance spectroscopy as a reference, too. The impedance of an NCM622 pellet with and without an auxiliary electrolyte
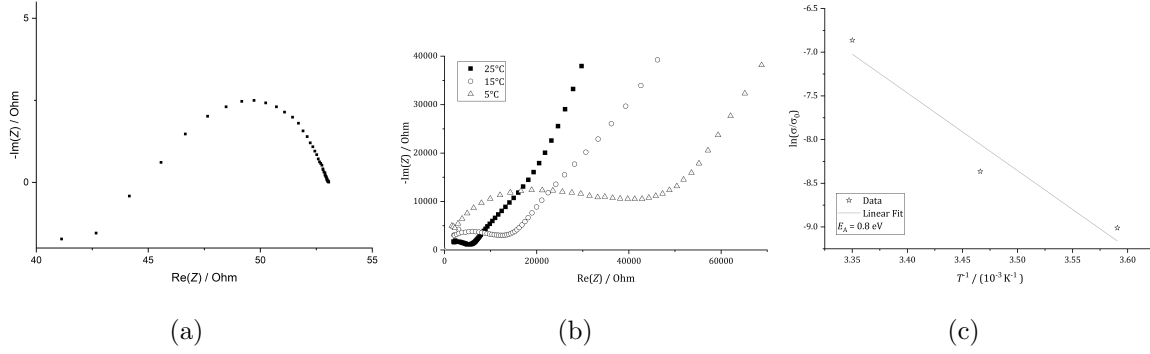
Figure 68 – Nyquist plot of a) NCM622 pellet, b) measured with auxiliary electrolyte, c) Arrhenius fit of impedance measurements of NCM + auxiliary electrolyte at different temperatures.

is measured. The resulting impedance spectra are shown in Fig. 68. Pure NCM622 features a total conductivity of 0.5 S cm^{-1}. With the use of an auxiliary electrolyte, $1.0 \cdot 10^{-6}$ S cm^{-1} are measured. That is approximately the conductivity of the polymer electrolyte itself ($7.4 \cdot 10^{-7}$ S cm^{-1}). The possibility that the ionic conductivity of NCM could be higher has to be admitted. The measured activation energy of diffusion of 0.8 eV determined with an Arrhenius approach (eq. 25), measured with the auxiliary electrolyte, as depicted in Fig. 68 c), is significantly lower as of the polymer electrolyte.

The Nyquist plots of impedance spectra of the catholyte mixtures are depicted in Fig. 69. The resistance at this point is 187 Ω for Nb-LLZO-NCM622 0.5:8 ($1.0 \cdot 10^{-3}$ S cm^{-1}) and 202 Ω for Al-LLZO-NCM622 0.5:8 ($9.4 \cdot 10^{-4}$ S cm^{-1}). They show capacitive features for higher frequencies before the signals get in phase. One can expect this shape in the Nyquist plot stems from the high electrical conductivity of NCM. The resistance is higher for the 1:1 catholyte pellets compared to 0.5:8. The resistance of the Nb-LLZO-NCM622 1:1 pellet is 46439 Ω ($4.1 \cdot 10^{-6}$ S cm^{-1}) and 46890 Ω ($3.7 \cdot 10^{-6}$ S cm^{-1}) for the Al-LLZO-NCM622 1:1 pellet, measured at the lowest frequency. The conductivities are listed in Tab. 13.

The impedance spectra of the catholyte pellets sandwiched between two layers of an auxiliary electrolyte are depicted in Fig. 69, too. Using an auxiliary electrolyte, the measured conductivity is one order of magnitude lower for the 1:1 mixtures. From the x-axis intersection, a value of $4.3 \cdot 10^{-5}$ S cm^{-1} and $2.7 \cdot 10^{-5}$ S cm^{-1} is calculated for Al-LLZO-NCM 1:1 and Nb-LLZO-NCM 1:1 with equation 19. The total conductivity drops by one order of magnitude for the 0.5:8 mixtures using an auxiliary electrolyte: Al-LLZO-NCM622 0.5:8 has a total conductivity of $1.1 \cdot 10^{-4}$ S cm^{-1} and $2.4 \cdot 10^{-4}$ S cm^{-1} for Nb-LLZO-NCM622 0.5:8. The shape of the impedance spectra with 0.5:8 compositions change to distinct semicircles. The shape of the Nyquist plots of the 1:1 compositions formed one semicircle without using an auxiliary electrolyte. Using the electrolyte, one
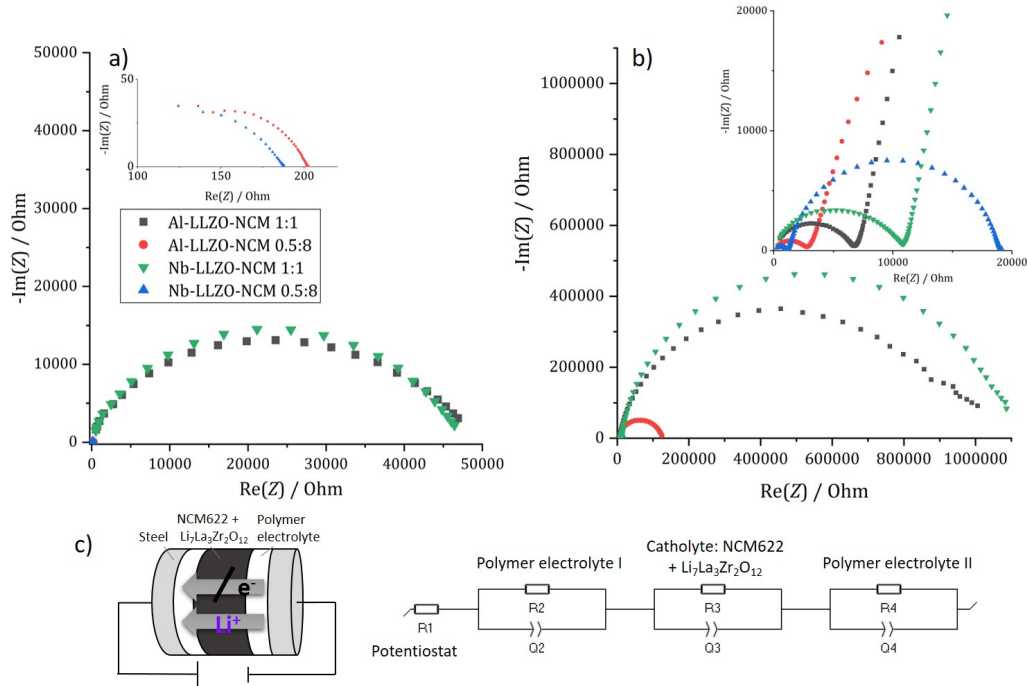
Figure 69 – Nyquist plots of impedance measurements of a): catholytes, b) catholytes with auxiliary electrolyte at 25°C, c) scheme of the cell setup with equivalent circuit.

additional semicircle appears for higher frequencies.

The assignment of the left semicircle in Fig. 69 b) to the resistance is discussable. Since two additional interfaces are introduced to the impedance measurement using the auxiliary electrolyte, one would expect to see a change in the impedance spectra in comparison to measuring simply a catholyte pellet. The conductivities were calculated using the left x-intersection. According to the laws of a serial circuit however, neither the total nor the electrical conductivity of the sandwiched catholytes is supposed to be higher than the composite electrolyte itself. This is the case for all total conductivity / impedance measurements. We must assume, that the electrolyte did not fully cover the catholyte and that some short-circuiting through the catholyte happened.

The direct current conductivity is lower using the auxiliary electrolyte so that this short-circuiting has only a minor effect. The electrical conductivity is at least partially suppressed with the use of the auxiliary electrolyte. Especially for the 0.5:8 compositions, the total conductivity is reduced using an auxiliary electrolyte. Comparing among the compositions, the resistance is higher for the 1:1 mixture for the measurements with auxiliary electrolyte. This is unexpected in a way that, following the idea of the experiment, a lower resistance can be assumed for the 1:1 composition due to the contribution of the LLZO to the ionic conduction on the one hand. On the other hand, the electric current is supposed to be blocked by the auxiliary electrolyte. This would lead to a higher resistance of the 0.5:8 compositions, again, following the concept just mentioned.

Table 13. – Activation energies, total conductivities and DC conductivities of pure catholytes and sandwiched between auxiliary electrolyte, and pure electrolyte at 25 °C, a.e.: auxiliary electrolyte.

Sample	E_A / eV		Total conductivity / S cm^{-1}		DC conductivity / S cm^{-1}	
	Catholyte	Catholyte with a.e.	Catholyte	Catholyte with a.e.	Catholyte	Catholyte with a.e.
Al-LLZO : NCM622 0.5:8	0.2	0.5	$9.4 \cdot 10^{-4}$	$1.1 \cdot 10^{-4}$	$9.4 \cdot 10^{-4}$	$2.5 \cdot 10^{-6}$
Al-LLZO : NCM622 1:1	0.2	0.5	$3.7 \cdot 10^{-6}$	$4.3 \cdot 10^{-5}$	$1.1 \cdot 10^{-5}$	$2.8 \cdot 10^{-7}$
Nb-LLZO : NCM622 0.5:8	0.2	0.3	$1.0 \cdot 10^{-3}$	$2.4 \cdot 10^{-4}$	$9.9 \cdot 10^{-4}$	$1.6 \cdot 10^{-5}$
Nb-LLZO : NCM622 1:1	0.2	0.4	$4.1 \cdot 10^{-6}$	$2.7 \cdot 10^{-5}$	$3.8 \cdot 10^{-6}$	$1.4 \cdot 10^{-7}$
Composite electrolyte	1.0		$3.4 \cdot 10^{-6}$		$7.4 \cdot 10^{-7}$	

The results of the impedance spectra demonstrate that this is not the case. Probably, the function of the auxiliary electrolyte to suppress electrical current is weakened by the relatively high electrical conductivity of the electrolyte of $7.4 \cdot 10^{-7}$ S cm^{-1}.

Impedance spectra of the catholyte compositions and catholyte compositions with auxiliary electrolytes measured at different temperatures are depicted in Fig. 87 and 89 in the appendix. With the extracted conductivities, an activation energy is calculated with an Arrhenius approach using eq. 25. The corresponding linearized data and Arrhenius fits are depicted in Fig. 88 and 90 in the appendix. The activation energies are listed in Tab. 13, too.

The activation energy of conductivity is 0.2 eV for all catholyte compositions. The activation energy for catholytes in combination with an auxiliary electrolyte is 0.5 eV for both Al-LLZO-NCM622 catholytes and 0.3 eV for Nb-LLZO-NCM622 0.5:8 and 0.4 eV for Nb-LLZO-NCM622 1:1. The activation energy of conductivity of the polymer auxiliary electrolyte was determined in the previous chapter to 1.0 eV. Thus, effects of short-circuiting the electrolyte by the catholyte must be assumed for these measurements, too, although some current is suppressed by the auxiliary electrolyte. Up to 88 % of the Nb-LLZO formed hydrogarnet after the ball milling (see Tab. 12). The lower conductivity of the hydrogarnet compared to garnet seems to have no effect on the

conductivity measurements of the catholyte, probably due to percolation effects.

7.6. Thermal stability

Fig. 70 depicts the results of the Rietveld refinement against high-temperature synchrotron diffraction patterns of LLZO-NCM-Carbon mixtures. An example of a refinement is depicted in Fig. 91 in the appendix. LaB_6 was used to account for the instrumental resolution.

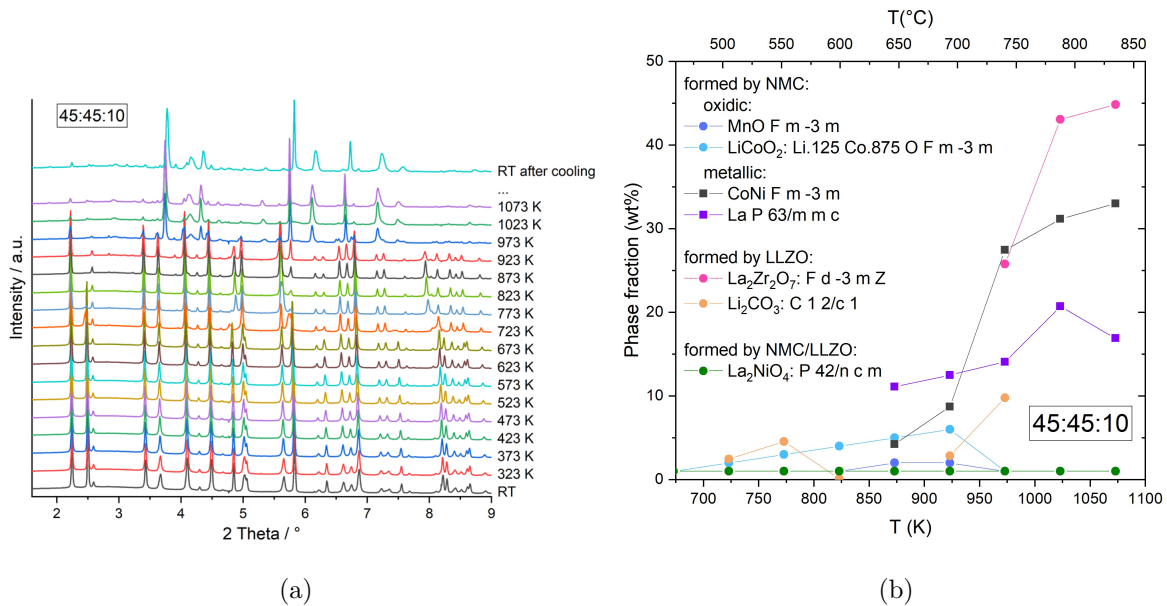No formation of impurity phases can be observed until 973 K for a LLZO/NCM622

Figure 70 – In situ HT-XRD diffraction pattern and phase fractions extracted from Rietveld refinement of LLZO/NCM622/Carbon mixture (45:45:10).

mixture in a previous study. $LaMnO_3$ was the primarily formed impurity phase at 1123 K.[164] For a LLZO/NCM622/ Carbon mixture impurity phase formation starts at 773 K with the formation of Lithium carbonate and segregation of $LiCoO_2$. Metallic phases like La and a CoNi alloy start forming from 873 K. $La_2Zr_2O_7$ forms at 973 K.

NCM is stable up to 673 K and LLZO up to 923 K. The decomposition of LLZO goes along with the formation of $La_2Zr_2O_7$.

The formation of $La_2Zr_2O_7$ and Li_2CO_3 at 973 K is often described in literature.[164,180,190] It is detrimental for the interface, as both $La_2Zr_2O_7$ and Li_2CO_3 are weak ionic conductors for Li^+.[58,156] Mixed oxides forming from Lanthanum and transition metal oxides are also known.[140,178,180,190] The formation of metallic phases has not yet been described. It is suspected that the reduction of metal oxides is strongly attributed to the presence of carbon. One can conclude from this data that 600 °C is the highest temperature that the catholyte composite with carbon can be sintered.

7.7. Conclusion and Outlook

Four different cathode composites were fabricated, which differ in their LLZO substituents (Al or Nb) and the weight ratio. The synthesis was carried out by ball milling, whereby in the case of Nb-LLZO the formation of relatively large amounts of hydrogarnet could be quantified with X-ray diffraction. The particle morphology was investigated with TEM and an approximately 2.5 nm large interface between LLZO and NCM with an amorphous structure could be observed.

The TEM micrographs demonstrate, that a majority of the NCM particles seems to have no direct contact to LLZO. With regard to an electrode that is to be charged at high currents, it might be advisable to increase the LLZO percentage.

With an auxiliary electrolyte, a possible diffusion barrier of the lithium ions in the catholyte composite is aimed to be measured with impedance spectroscopy. Due to the relatively high electrical conductivity of the electrolyte, the effects of ionic conductivity are superimposed by those of electrical current. However, conceptual proof of the feasibility of this method could be obtained. With an electrolyte with a lower electrical conductivity, it should be possible to determine the diffusion or conductivity of the lithium through the cathode composite. Another reason for the high resistance of the 1:1 NCM:LLZO catholytes, sandwiched into an auxiliary electrolyte, can be that the catholytes were not sintered beforehand. Therefore they are not dense enough to enable Li ion diffusion across the particles.

High-temperature synchrotron diffraction of LLZO-NCM-Carbon mixtures yielded in a reduction of the metal cations to metallic phases of Co, Ni and La at 650 ℃. $La_2Zr_2O_7$ and Li_2CO_3 start to form at 750 ℃. Knowing the temperature, up to which the NCM-LLZO compositions can be sintered, the experiment could be carried out with sintered NCM-LLZO pellets together with the auxiliary electrolyte.

8. Microstructural characterization of Lithium Aluminum Titanium Phosphate

$Li_{1.3}Al_{0.3}Ti_{1.7}(PO_4)_3$ (LATP) is a promising ceramic Lithium conductor with the highest ionic conductivities known for oxidic ceramics of about 10^{-3} S cm^{-1}.[4,125] Another advantage of this material is that it can be sintered together with NCM up to 800 °C without impurity phase formation[88], which is higher than NCM together with LLZO. The following chapter contains results that are part of the manuscript *Upscaling of LATP synthesis: Stoichiometric screening of phase purity and microstructure to ionic conductivity maps* by Nikolas Schiffmann, Ethel C. Bucharsky, Karl G. Schell, Charlotte A. Fritsch, Michael Knapp and Michael J. Hoffmann.[150]

8.1. Aim of the work

Studies about the synthesis of LATP by different methods such as calcination of oxidic precursors,[5] glass crystallization,[125] or sol-gel.[14] focus on an output limited to laboratory scale. To address the need for ceramic electrolytes usable in next generation batteries, processing routes need to be upscaled. The sol-gel route is already successfully used on a large scale in industry and therefore provides a good basis for LATP synthesis.[153] In order to ensure reproducibility, crucial processing parameters have to be identified. The influence of possible deviations in the concentration of the precursors were investigated. This applies especially to phosphoric acid, difficult to specify precisely in concentration due to its hygroscopy. Deviations from stoichiometric mixtures of the precursors can easily lead to second-phase formation. In the case of LATP, side phases have a great influence on densification and ionic conductivity. Hupfer et al.[73] present, how the second phases $AlPO_4$ and $LiTiOPO_4$ impact the properties of LATP.

The following analysis using Rietveld refinement examines the microstructural parameters and impurity phases in the event of deviations in the phosphoric acid content. LATP-st refers to a stoichiometric synthesis, LATP-ex and LATP-def refer to an excess or a deficiency of phosphoric acid.

8.2. Green powder

The graphs of the refinements of the XRD patterns for calcined LATP powders derived from the sol-gel batches are depicted in Fig. 72 to 74. Apparently, the calcined $Li_{1.3}Al_{0.3}Ti_{1.7}(PO_4)_3$ powders crystallize in the trigonal NZP -type structure, derived from $NaZr_2(PO_4)_3$ (R-3c, space group No. 167) from the PDF-2-database (ICDD). Fig. 71 illustrates the crystal structure of LATP as a result of the Rietveld refinement of

sintered stoichiometric LATP (LATP-st) based on a model of Dashjav and Tietz.[22] Rietveld refinement reveals that an excess of 7.5 wt.-% H_3PO_4 leads to the formation of 4.7 wt.-% $AlPO_4$ and a deficit of 7.5 wt.-% H_3PO_4 to 5.6 wt.-% $LiTiOPO_4$ as an impurity.

Further crystallographic information extracted from the refinement is listed in Tab. 14. The phase-pure calcined LATP-st sample shows the least amount of microstructural strain in the powder analysis. A comparably larger volume of the unit cell is observed for calcined LATP-ex. The cell volume of calcined LATP-def is comparable to the cell volume of calcined LATP-st with a slightly increased microstrain. No size broadening could be detected. The analysis demonstrates that small changes in the synthesis route cause the formation of second phases and influence the crystal geometry of the unit cell size.
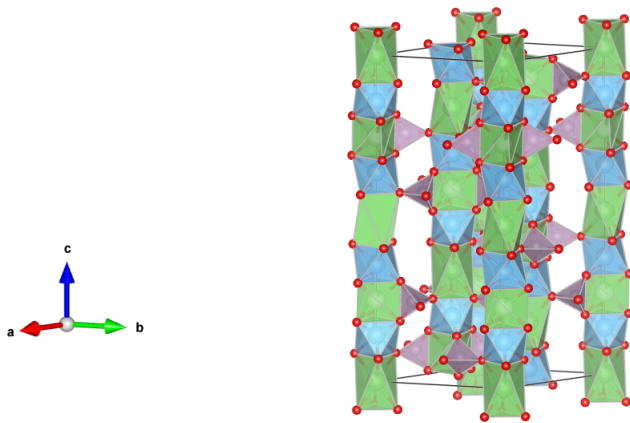

Figure 71 – Crystalline structure of LATP as a result of the Rietveld refinement of sintered stoichiometric LATP (LATP-st), green: Li, light blue: Al, Ti, brown: P, red: O.
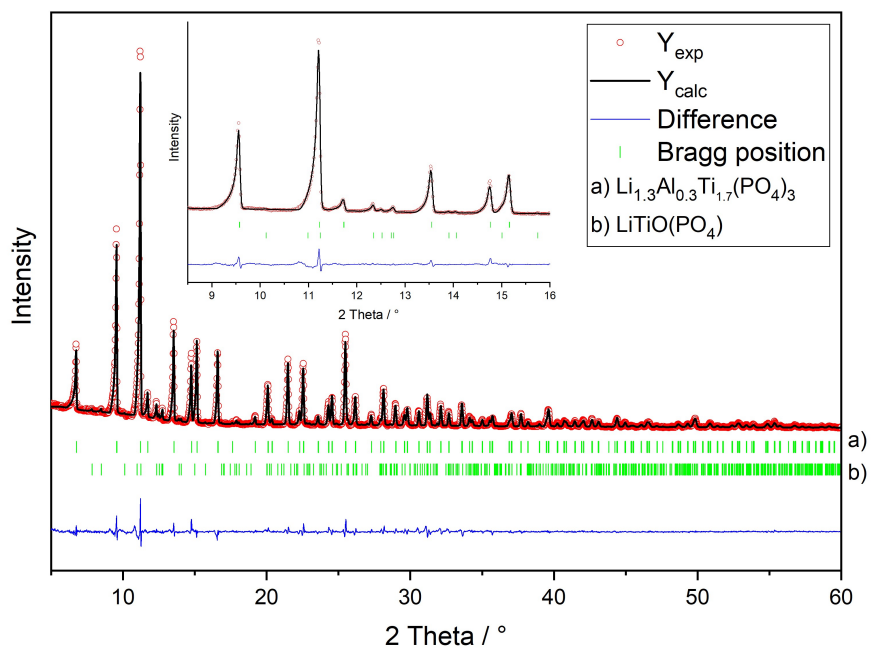
Figure 72 – Rietveld refinement of the structure model of LATP, synthesized with phosphorus acid deficiency LATP-def, based on powder diffraction data (Mo $K_{\alpha 1}$).
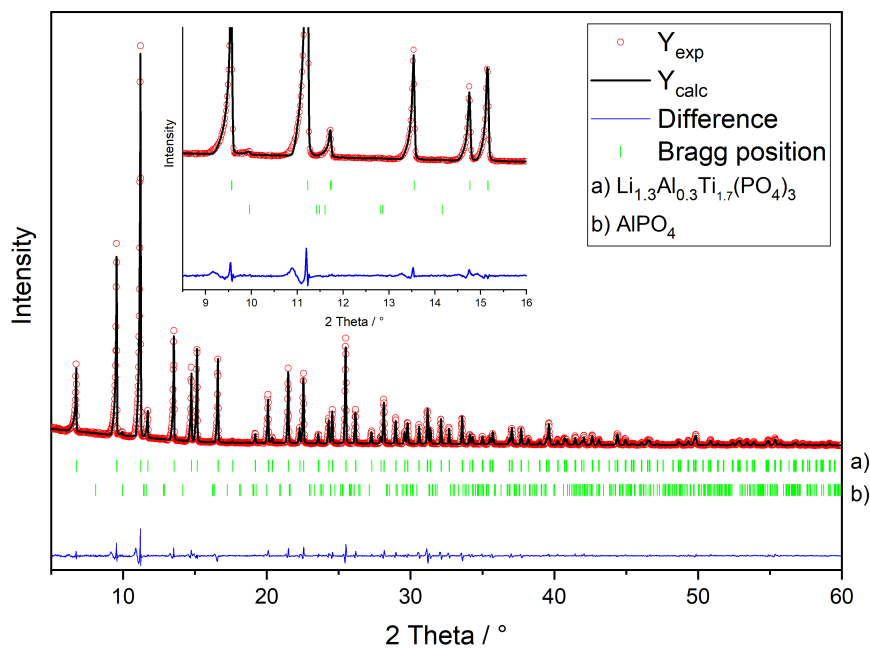

Figure 73 – Rietveld refinement of the structure model of LATP, synthesized under stoichiometric conditions LATP-st, based on powder diffraction data (Mo $K_{\alpha 1}$).
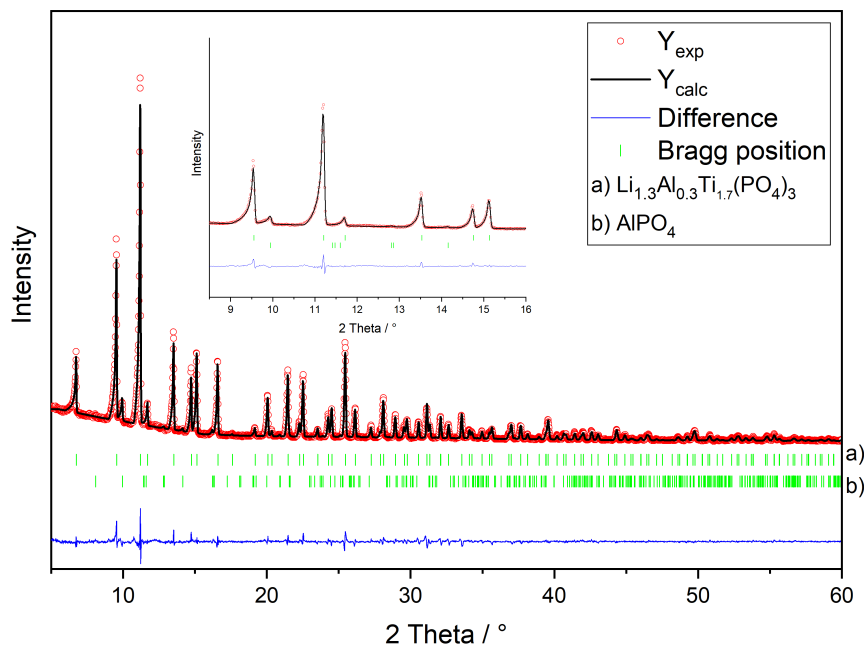
Figure 74 – Rietveld refinement of the structure model of LATP, synthesized with phosphorus acid excess LATP-ex, based on powder diffraction data (Mo $K_{\alpha 1}$).

8.3. Sintered powder

XRD investigations of selected sintered samples show the influence of the heat treatment on the crystal structure and the evolution of the secondary phases.

The parameters extracted from Rietveld refinements are also listed in Tab. 14. The sample sintered from LATP-st powder remains phase pure, but shows more structural strain and an expansion of the unit cell predominantly along the c-axis. The sample derived from LATP-ex powder features a slight decline in the unit cell volume and a reduction of the structural strain. $AlPO_4$ remains present as a second phase. The analysis of a sintered LATP-def sample shows less structural strain and a contraction of the unit cell mainly by shortening of the c-axis. There is less secondary phase $LiTiOPO_4$ present compared to the calcined powder, but TiO_2 is detectable in addition. It seems that $LiTiOPO_4$ decomposes under the formation of TiO_2.

The graphs of the refinement are depicted in the appendix in Fig. 92 to 94.

8.4. Conclusion

The study enables the evaluation of fluctuations in the concentration of the precursor phosphoric acid. Details on the ionic conductivity and optical characterization can be found in the manuscript.[150] A stoichiometric synthesis yields ionic conductivities of $1 \cdot 10^{-3}$ S cm^{-1}.[150] An excess of H_3PO_4 leads to the formation of the impurity phase

Table 14. – Results of Rietveld refinement of diffraction patterns from green powders and sintered samples of LATP-ex, LATP-st and LATP-def.

Sample	Impurities / wt-%	Lattice parameter / Å	Cell Volume / Å^3	Structural strain / $\mathrm{d}D/D \cdot 10^{-4}$
LATP-ex green	4.7 ($\pm$0.4) AlPO$_4$	a, b = 8.115 c = 20.8507	1308.2 ($\pm$0.1)	16.6 ($\pm$0.1)
LATP-ex sintered	4.1 ($\pm$0.4) AlPO$_4$	a, b = 8.5078 c = 20.8388	1306.3 ($\pm$0.1)	11.0 ($\pm$0.1)
LATP-st green	< 1% AlPO$_4$	a,b = 8.5058 c = 20.8112	1303.9 ($\pm$0,4)	11.7 ($\pm$0.1)
LATP-st sintered	-	a,b = 8.5176 c = 20.9248	1314.7 ($\pm$0.8)	21.6 ($\pm$0.2)
LATP-def green	5.6 ($\pm$0.4) LiTiOPO$_4$	a, b = 8.5035 c = 20.8119	1303.3 ($\pm$0.1)	17.8 ($\pm$0.2)
LATP-def sintered	3.5 ($\pm$0.5) LiTiOPO$_4$ 1.8 ($\pm$0.4) TiO$_2$	a, b = 8.4692 c = 20.7187	1287.0 ($\pm$0.1)	11.2 ($\pm$0.3)

AlPO$_4$. This impurity has a significant reducing effect on the conductivity, resulting in $3 \cdot 10^{-4}$ S cm^{-1}.[150] The deficiency of H$_3$PO$_4$ can be tolerated. LiTiOPO$_4$ is formed as a second phase, which does not impede ionic mobility. A conductivity of $1 \cdot 10^{-3}$ S cm^{-1} was measured.[150] However, the LiTiOPO$_4$ is suspected to hinder densification. Therefore, sintering time and temperature have to be adjusted in the case of H$_3$PO$_4$ deficiency.

9. Experimental

9.1. Syntheses and chemical processing

9.1.1. Mechanochemical synthesis of sodium thiophosphates

The following work steps were carried out under inert atmosphere in an argon filled glovebox (M Braun, O_2, H_2O < 0.1 ppm).

A batch of 4 g of a stoichiometric mixture of Na_2S (Sigma Aldrich) and P_2S_2 (Honeywell-Fluka 99%) together with 70 g ZrO_2 balls with a diameter of 3 mm was ball milled in a ZrO_2 bowl of 45 mL using a planetary ball mill *Pulverisette 7 Premium Line* (Fritsch) under argon atmosphere at 510 rpm, grinding without solvent. Full amorphization of the starting materials was reached at 240 grinding cycles (5 min alternating with 15 min rest for cooling). Crystalline $Na_2P_2S_6$ is obtained through thermal annealing of amorphous $Na_2P_2S_6$. The amorphous material was calcined in Al_2O_3 crucibles sealed in quartz glass tubes under vacuum at 623 K for 10 h to reach crystallization. The heating and cooling rate was 2 K min^{-1}.

As a reference material for NMR and Raman spectroscopy, Na_3PS_4 was synthesized by the procedure described above using a molar concentration of 75 % Na_2S and 25 % P_2S_5. In contrast to $Na_2P_2S_6$, this phase already crystallizes during ball milling after only 30 min. Even after milling for 20 h the sample remains crystalline.

9.1.2. Commercial samples

LLZO samples were purchased from MSE supplies with different substituents. Their stoichiometry is published by the supplier: $Li_{6.25}Al_{0.25}La_3Zr_2O_{12}$, $Li_{6.5}La_3Zr_{1.5}Nb_{0.5}O_{12}$, $Li_{6.4}La_3Zr_{1.4}Ta_{0.6}O_{12}$, $Li_{6.3}La_3Zr_{1.65}W_{0.35}O_{12}$. The stoichiometry was revised by ICP-OES, see chapter 9.10. The material was stored under inert atmosphere in an argon filled glovebox (M Braun, O_2, H_2O < 0.1 ppm).

9.1.3. Ceramic synthesis of LLZO

LLZO was prepared by a high temperature route using Li_2CO_3 (Alfa Aesar), ZrO_2 (Alfa Aesar) and La_2O_3 (Fischer Scientific) and stoichiometric amounts of $AlNO_3$ (Merck), NbO_2, Ta_2O5 or $WO_{2.9}$ substituents (Alfa Aesar). The starting materials were mixed in stoichiometric amounts (with 5 wt% Li_2CO_3 excess) and milled for 1 h in 2-propanol in a planetary ball mill (Fritsch, Pulverisette) with zirconia balls and grinding bowls. After calcination at 1100 °C in MgO crucibles, garnet-type LLZO was obtained as a white powder. LiOH (Merck) as a reference was dried in vacuum overnight.

9.1.4. Ball milling

The powder was ball milled at 510 rpm with 5 mL 2-propanol for 1 h in a planetary ball mill (Fritsch, Pulverisette) with zirconia balls and grinding bowls. 5 min of milling time were alternated with 15 min resting to prevent overheating.

9.1.5. Sintering

The powder was pressed to pellets, covered with mother powder, and sintered at 1100 °C for 10 h.

9.1.6. Diluting, drying

The powder was stirred for 1 h at 60 °C in the specified solvent and afterwards dried at 80°C for 24 h.

9.1.7. Composite electrolytes

Composite electrolytes were synthesized by dissolving LLZO, LiTFSI and PEO ($M_v = 10^6$) in acetonitrile and stirring at 60°C for 2 h. The slurry was tape casted on Alumina foil and dried at 80 °C over night in vacuum. The electrolytes were stored under inert atmosphere in an argon filled glovebox (M Braun, O_2, H_2O < 0.1 ppm).
Nanomyte SE50 and *H-Polymer* were purchased from NEI corporation and have a highly viscous and sticky texture. It was fabricated into coin cells by rolling between two sheets of coated paper. Diluting with Acetonitrile, washing and subsequent drying yielded a white powder which is suspected to be almost pure LLZO.

9.1.8. Catholyte composites

Synthesis of cubic, Al-doped LLZO is described above. NCM622 was purchased from BASF SE. 8 g of NCM 622 and 0.5 g of LLZO were ball milled with 5 mL of Isopropanol in a 80 mL ZrO_2 grinding bowl with 70 g ZrO_2 balls for 1 h and 500 rpm. After ball milling, the powder is dried at 80 °C for 24 h.
A CAM-LLZO-carbon mixture with a weight ratio of 45:45:10 was mortared under argon atmosphere. LLZO was supplied by Schott AG.

9.2. Nuclear magnetic resonance spectroscopy

9.2.1. MAS-NMR

^{6}Li, ^{23}Na, ^{27}Al, and ^{31}P MAS NMR spectra were obtained at a spinning speed of 20 kHz on a Bruker Avance 500 MHz spectrometer at a field of 11.7 T, which corresponds to

resonance frequencies of 73.6 MHz (^{6}Li), 132.3 MHz (^{23}Na), 130.3 MHz (^{27}Al), and 202.5 MHz (^{31}P). For these measurements, the sample was packed into a 2.5 mm zirconia MAS rotor in an argon-filled glove box. The spectra were recorded with a rotor-synchronized Hahn-echo pulse sequence. 1 M LiCl, 1 M NaCl, 1 M Al(NO$_3$)$_3$, and H$_3$PO$_4$ (85%) were used to calibrate the chemical shift for each to 0 ppm.

9.2.2. Temperature-dependent NMR spectroscopy: Relaxation, linewidth vs. temperature, PFG-NMR

Solid state static ^{7}Li NMR spectra were acquired on a Bruker NMR spectrometer operating at 200 MHz proton frequency. The spectrometer was equipped with a high-temperature probe which allows measurements in a temperature range -100 to 250 °C. Static spectra were measured with a quadrupolar echo pulse sequence with an inter-pulse delay of 30 μs. The relaxation delays were optimized for every measurement basing on the value of the spin-lattice relaxation time. T_1 relaxation times were obtained with a saturation recovery pulse sequence. The number of experimental points building a relaxation curve was set in a such way to observe a full restoration of the initial signal. Pulsed-field gradient self-diffusion coefficient measurements were accomplished on a Bruker NMR spectrometer with a static field of 7.05 T. The stimulated echo pulse sequence with bipolar gradients was used to measure the long-range translational motion of the ^{7}Li ions. The temperature range assessed with the gradient probe is 25 to 80 °C. A pre-scan delay has been chosen on the base of prior relaxation time measurements. The diffusion parameters were optimized before measurements in order to gain a visible drop of a signal intensity as a function of gradient strength. The diffusion times varied in the range of 75-100 ms and the gradient duration was set between 3 and 4.5 ms.

9.3. Impedance spectroscopy

Electrochemical impedance spectroscopy (EIS) measurements were performed using a BioLogic SP300 potentiostat at frequencies from 1 MHz to 10 mHz with a 100 mV sinusoidal amplitude at 25 °C. The (ion) conductivity was calculated based on the equation:

$$\sigma = d/(a \cdot R) \tag{28}$$

where σ is the ion conductivity, d is the pellet thickness, a is the pellet size and R is the resistance.

9.4. Raman spectroscopy

Raman spectroscopy was performed on a LabRAM HR Evolution spectrometer (HORIBA Scientific) using a 100× magnification objective with an excitation wavelength of 632.81 nm. The spectral data were recorded with exposure times of 10 s over the wavenumber range of 100 to 1100 cm^{-1}. All samples were measured in sealed glass capillaries. All Raman spectra were baseline corrected using the Horiba Labspec 6 software.

9.5. Infrared spectroscopy

Infrared spectroscopy was performed with a Bruker Tensor 27 Fourier transform infrared spectroscopy (FT-IR) spectrometer. Data was recorded from 4000 - 400 cm^{-1}.

9.6. Diffraction

9.6.1. X-ray diffraction

Diffractograms were recorded with a STOE Stadi P powder diffractometer using the Debye-Scherrer method in the range of $2\,\theta = 5$ to 50° and 0.017° steps with a molybdenum anode. The Mo K$_{\alpha 1}$ radiation has a wavelength of $\lambda = 0.70932$ Å. A graphite furnace with a capillary holder was used for the high temperature measurements. Quartz capillaries were used with 10 min of holding time to adjust the temperature.

The Rietveld refinement is done with the software WinPlotr by FullProf.[148] LaB$_6$ is taken to account for the instrumental resolution.

Synchrotron

The diffraction patterns of the catholyte-carbon mixtures were recorded at the P02.1 beamline at PETRA-III, DESY, in Hamburg with a wavelength of 0.20714 Å[30] from 25-700 °C. Integration of the diffraction patterns from the 2D-detector was performed using the software Fit2D.

9.6.2. Total scattering pair distribution function analysis

Room temperature synchrotron total scattering experiments were performed at the high-resolution powder diffraction beamline (P02.1) at PETRA III, DESY, using synchrotron radiation with a photon energy of 60 keV ($\lambda = 0.20723$ Å).[30] The diffraction patterns were acquired using a PerkinElmer area detector with a sample-detector distance of 350 mm. The exposure time for each diffraction pattern was 20 min. The obtained 2D images were integrated to 1D patterns by using the program DAWNscience.[40] Powder samples were measured in sealed glass capillaries with 0.5 mm diameter. An empty

capillary was measured under the same conditions and used for background subtraction. To account for the instrumental resolution function, LaB_6 (NIST660a) and a Ni reference were measured. The corresponding pair distribution function was calculated using pdfgetx3[81] with $Q_{max} = 20$ Å^{-1}. Calculation of PDFs based on molecular models and real space Rietveld fitting was performed with PDFgui.[39]

9.6.3. Neutron diffraction

Neutron diffraction measurements were carried out on the high-resolution powder diffractometer SPODI (research neutron source FRM-II, Garching, Germany) with monochromatic neutrons ($\lambda = 1.5482$ Å). The measurements were carried out in Debye-Scherrer geometry from $2\theta = 4$ - 150 ° with an exposure time of 12 h.
The powder sample was placed under argon in a cylindrical thin-walled vanadium container with a diameter of 10 mm and sealed with indium wire. The data analysis was carried out using the Rietveld method using the FullProf software package. Instrumental resolution was taken into account using a $Na_2Ca_3Al_2F_{14}$ standard.

9.7. Thermogravimetry

Thermogravimetric analysis (TGA) and dynamic difference calorimetry measurements were carried out with a STA 499 C device of the Jupiter series from the company Netsch over temperature range from 120 to 700 °C with a heating rate of 5 K / min. The data were evaluated with the Proteus software.

9.8. Scanning electron microscopy

Scanning electron microscopy (SEM) micrographs were recorded using a Zeiss Merlin microscope with 10 kV acceleration voltage.

9.9. Transmission electron microscopy

For microstructural examinations, transmission electron microscopy (TEM) and scanning transmission microscopy (STEM) were conducted using a Cs-corrected *JEM-ARM200F* microscope with an accelerating voltage of 200 kV. Thin foils for TEM and STEM were prepared by crushing small amount of sample and dispersing them onto a carbon grid. Thin foils were examined by TEM bright-field and dark-field imaging modes as well as by selected-area electron diffraction (SAED) analysis. STEM was conducted with energy dispersive X-ray spectroscopy (EDS) using a silicon drift detector and by high-angle annular dark-field (HAADF) imaging mode using a convergence angle of 46 mrad and

detecting angles of 90-370 mrad.

The radial intensity profile was created with ImageJ with the radial profile plugin. The diffraction simulations and the overlay were created with JEMS.[149]

9.10. Elemental analysis

The elemental analysis was performed for the commercial LLZO samples.

The stoichiometry was revised by X-ray fluorescence spectroscopy (XRF) (*Pioneer S4, Bruker AXS*), inductively-coupled plasma optical-emission spectroscopy (*iCAP 7600 ICP-OES Duo*, Thermo Fisher Scientific) and carrier gas hot extraction (CGHE) (*TC 600*, LECO) for oxygen, as described below.

For the XRF measurement, 25 mg (accuracy $\pm$ 0.05 mg) of each sample together with 6000 mg (49.75 % $Li_2B_4O_7$+ 49.75 % $LiBO_2$ + 0.5 % LiBr) has been balanced in a platinum crucible and fused by 1100 ℃. Afterwards the flux has been poured out in a platinum dish. For the calibration four fusion tablets with matrix-adapted standards (Li_2CO_3, Al_2O_3, ZrO_2, La_2O_3, Nb_2O_5, Ta_2O_5, WO_3) were melted. The range of the calibration solutions did not exceed a decade. Two to three energy lines of the elements have been used for calculation.

For the ICP-OES measurement, 30 mg of the samples (accuracy $\pm$ 0.05 mg) was dissolved in 4 ml hydrochloric acid, 4 ml sulfuric acid and 0.02 ml Hydrofluoric acid at 250 ℃ for 12 h in the pressure digestion vessel *DAB-2* (Berghof). The analysis of the elements was accomplished with four different calibration solutions and an internal standard (Sc). The range of the calibration solutions did not exceed a decade. Two to three wavelengths of the elements have been used for calculation.

The oxygen concentration was calibrated with the certified standard KED 1025, a steel powder from ALPHA. The calibration was verified with two oxide powders (La_2O_3, ZrO_2). The calibration range was close to the concentration of the samples. The standards and the samples were weighed with 3 mg to 100 mg (weighing accuracy $\pm$ 0.05 mg) in Sn crucibles (5 · 12 mm). 5 mg Graphite was added and wrapped. Combined with a Sn pellet (about 200 mg) it was put into a Ni crucible. The package was loaded in an outgassed (6300 W) double graphite crucible and measured at 5800 W. The evolving gases CO_2 and CO were swept out by helium as an inert carrier gas and measured by infrared detectors.

10. Summary and Outlook

Amorphous and crystalline Na$_2$P$_2$S$_6$

Amorphous Na$_2$P$_2$S$_6$ was synthesized via ball milling and subsequently thermally crystallized. The local structures and P-S building blocks in amorphous and crystalline Na$_2$P$_2$S$_6$ differ which has been examined by XRD, XRD-PDF analysis, and ^{23}Na/^{31}P MAS NMR spectroscopy. The NMR spectrum of crystalline Na$_2$P$_2$S$_6$ shows two P signals that are in good agreement with the crystalline structure of Na$_2$P$_2$S$_6$ determined by Rietveld refinement. ^{31}P MAS NMR shows a difference in the chemical shifts of crystalline and amorphous Na$_2$P$_2$S$_6$, revealing the presence of different local building blocks in these materials. The measurements indicate that single PS$_4^{3-}$ tetrahedra and corner-sharing tetrahedra are transformed to edge-sharing-tetrahedra during crystallization of amorphous Na$_2$P$_2$S$_6$ to crystalline Na$_2$P$_2$S$_6$. The difference in molecular structure with the same stoichiometry causes a difference in the material characteristics, which was demonstrated by impedance measurements of the ionic conductivity. A re-amorphization of the crystalline Na$_2$P$_2$S$_6$ can be observed after ball milling with XRD, XRD-PDF analysis, and ^{31}P MAS NMR spectroscopy. Impedance shows a higher conductivity of amorphous Na$_2$P$_2$S$_6$. The higher conductivity is measured again after ball milling and amorphization of crystalline Na$_2$P$_2$S$_6$.

Garnet vs. hydrogarnet LLZO

The formation of a hydrogarnet structure starting from garnet LLZO with Al, Nb, Ta, and W substitution was investigated with XRD, NPD, XRD-PDF analysis, ^{6}Li and ^{27}Al MAS NMR. Ball milling transforms the higher symmetric garnet structure to the hydrogarnet structure and thermal annealing causes the reverse effect. The formation of the hydrogarnet structure does not depend on the type of substituting cation. The two crystal structures can be distinguished by diffraction methods due to the symmetry reduction $Ia\bar{3}d$ to $I\bar{4}3d$, i.e. a loss of the threefold inversion axis in the hydrogarnet structure. PDF analysis shows a distortion of the octahedral MO$_6$ (M = Al, Zr, Nb, Ta, W) coordination in the hydrogarnet. With ^{6}Li MAS NMR, we observe two different local environments of Li in the hydrogarnet structure and one in the garnet, as expected from the XRD and NPD results. The hydrogarnet structure offers an additional Li site that is highly occupied and therefore is supposed to slow down the long-range Li transport. The mobility of Li in the hydrogarnet structure was measured on different time/length scales from single local jumps to bulk and long-range conductivity with ^{7}Li NMR and impedance spectroscopy. The conductivity of garnet LLZO is in the range of 10^{-4} S cm^{-1} with an activation energy of 0.33- 0.39 eV measured by impedance spectroscopy which is

in good agreement with the results of PFG-NMR. Both T_1 relaxation and motional line narrowing demonstrate that the hydrogarnet structure causes a lower mobility of Li on short time scales. PFG NMR indicates a lower long-range mobility in the hydrogarnet structure. Stability against solvents and temperature stability and expansion were examined with diffraction. No impurity phase formation occurs with polar protic solvents during stirring at 60 ℃ for 1 h and there is no evidence of an H^+ exchange. The thermal expansion of garnet W-LLZO is in good agreement with literature values for Al-LLZO.

LLZO polymer composite electrolytes

In order to evaluate the long-range conductivity of Li in the hydrogarnet structure, an approach without a sintering step is chosen to exclude the conversion of $I\bar{4}3d$ to $Ia\bar{3}d$. LLZO in garnet and hydrogarnet structure is incorporated into a polymer matrix to form a composite electrolyte. With PFG-NMR and EIS it could be shown independently that the long-range Li^+ conductivity and diffusion in the hydrogarnet structure is subject to the garnet structure. We measure a conductivity of $3.4 \cdot 10^{-6}$ S cm^{-1} for the garnet composite and $1.2 \cdot 10^{-6}$ S cm^{-1} for the hydrogarnet composite. These results are confirmed by measuring the activation energy of diffusion with both EIS and PFG-NMR. A higher activation energy of lithium diffusion of 1.1 eV is measured in the hydrogarnet composite, compared to 1.0 eV in the garnet composite. The conductivity of the composite electrolyte, using polyethylene oxide and the salt LiTFSI, is two orders of magnitude lower compared to pure LLZO.

Interface LLZO - NCM

Four different cathode composites were fabricated, which differ in their LLZO substituents, Al or Nb, and the weight ratio: 1:1 or 0.5:8. The synthesis was carried out by ball milling, whereby in the case of Nb-LLZO the formation of relatively large amounts of hydrogarnet could be quantified with XRD. The particle morphology was investigated with TEM and an approximately 2.5 nm large interface between LLZO and NCM with an amorphous structure could be observed. The TEM micrographs demonstrate, that a majority of the NCM particles seems to have no direct contact to LLZO after ball milling. A possible diffusion barrier of the lithium ions in the catholyte composite is aimed to be measured with impedance spectroscopy using two layers of an auxiliary electrolyte on both sides of the catholyte to block electric current flow through the catholyte. Due to the relatively high electrical conductivity of the electrolyte, the effects of ionic conductivity are superimposed by those of electrical current. However, conceptual proof of the feasibility of this method could be obtained. High-temperature synchrotron diffraction

of LLZO-NCM-Carbon mixtures yielded in a reduction of the metal cations to metallic phases of Co, Ni and La at 650 °C. $La_2Zr_2O_7$ and Li_2CO_3 start to form at 750 °C.

LATP

A stoichiometric synthesis of LATP yields ionic conductivities of $1\cdot10^{-3}$ S cm^{-1}.[150] An excess of H_3PO_4 leads to the formation of the impurity phase $AlPO_4$. This impurity has a significant reducing effect on the conductivity, resulting in $3\cdot10^{-4}$ S cm^{-1}. The deficiency of H_3PO_4 can be tolerated better in terms of the resulting conductivity. $LiTiOPO_4$ is formed as a second phase, which does not impede ionic mobility. We measure $1\cdot10^{-3}$ S cm^{-1}. However, the $LiTiOPO_4$ is suspected to hinder densification. Therefore, sintering time and temperature would have to be adjusted in the case of H_3PO_4 deficiency.

The findings from this work can be used to improve the processing of electrolytes and upscale their production. Harsh mechanical treatment can lead to phase transitions and amorphization. The formation of the desired phase can be sensitive to fluctuations in concentration of the educts.

Future works can focus on the compatibility of the solid electrolyte with the electrodes. In order to be able to observe the entry and exit of lithium ions into the solid electrolyte over a period of time, the development of a suitable electrochemical cell housing for *operando* diffraction or spectroscopy is helpful. The long-term stability of the electrolyte-electrode interface can also be examined in this way.

The experiment with the cathode composite with an auxiliary electrolyte could be repeated using an electrolyte with a lower electrical conductivity to separate more clearly between electrical and ionic conductivity. Another approach is to carry out the experiment with sintered NCM-LLZO pellets together with an auxiliary electrolyte to exclude hindered ion transport across grain boundaries.

A process for uniform coating of the CAM with the electrolyte must be developed in order to enable an optimal Li transfer.

11. References

[1] AIST: Spectral Database for Organic Compounds SDBS.

[2] ICSD Datenbank FIZ Karlsruhe - Leibniz Institute for Information Infrastructure. https://icsd.fiz-karlsruhe.de, 2018.

[3] S. Adams and R. P. Rao. *Journal of Materials Chemistry*, 22(4):1426–1434, 2012.

[4] H. Aono, E. Sugimoto, Y. Sadaoka, N. Imanaka, and G. ya Adachi. *Journal of The Electrochemical Society*, 137(4):1023–1027, 1990.

[5] K. Arbi, M. Hoelzel, A. Kuhn, F. Garcia-Alvarado, and J. Sanz. *Inorganic Chemistry*, 52(16):9290–9296, 2013.

[6] M. I. Aroyo, P.-M. J. Manuel, C. Cesar, K. Eli, I. Svetoslav, M. Gotzon, K. Asen, and W. Hans. Bilbao Crystallographic Server: I. Databases and crystallographic computing programs, 2006.

[7] J. Awaka, A. Takashima, K. Kataoka, N. Kijima, Y. Idemoto, and J. Akimoto. *Chemistry Letters*, 40(1):60–62, 2011.

[8] S. S. Berbano, I. Seo, C. M. Bischoff, K. E. Schuller, and S. W. Martin. *Journal of Non-Crystalline Solids*, 358(1):93 – 98, 2012.

[9] G. Bergerhoff, M. Berndt, K. Brandenburg, and T. Degen. . *Acta Crystallographica Section B*, 55(2):147–156, 1999.

[10] C. Bischoff, K. Schuller, N. Dunlap, and S. W. Martin. *The Journal of Physical Chemistry B*, 118(7):1943–1953, 2014.

[11] C. Bischoff, K. Schuller, M. Haynes, and S. W. Martin. *Journal of Non-Crystalline Solids*, 358(23):3216 – 3222, 2012.

[12] F. Bloch, W. W. Hansen, and M. Packard. *Phys. Rev.*, 69:127–127, 1946.

[13] K. Borzutzki, J. Thienenkamp, M. Diehl, M. Winter, and G. Brunklaus. *J. Mater. Chem. A*, 7:188–201, 2019.

[14] E. Bucharsky, K. Schell, A. Hintennach, and M. Hoffmann. *Solid State Ionics*, 274:77 – 82, 2015.

[15] H. Buschmann, S. Berendts, B. Mogwitz, and J. Janek. *Journal of Power Sources*, 206:236 – 244, 2012.

[16] H. Buschmann, J. Dölle, S. Berendts, A. Kuhn, P. Bottke, M. Wilkening, P. Heitjans, A. Senyshyn, H. Ehrenberg, A. Lotnyk, V. Duppel, L. Kienle, and J. Janek. *Phys. Chem. Chem. Phys.*, 13:19378–19392, 2011.

[17] G. G. Cameron. *British Polymer Journal*, 20(3):299–300, 1988.

[18] F. Croce, L. Persi, B. Scrosati, F. Serraino-Fiory, E. Plichta, and M. Hendrickson. *Electrochimica Acta*, 46(16):2457 – 2461, 2001.

[19] F. Croce, L. Settimi, and B. Scrosati. *Electrochemistry Communications*, 8(2):364 – 368, 2006.

[20] S. P. Culver, R. Koerver, W. G. Zeier, and J. Janek. *Advanced Energy Materials*, 9(24):1900626, 2019.

[21] Y. Dai, Y. Wang, S. Greenbaum, S. Bajue, D. Golodnitsky, G. Ardel, E. Strauss, and E. Peled. *Electrochimica Acta*, 43(10):1557 – 1561, 1998.

[22] E. Dashjav and F. Tietz. *Zeitschrift für anorganische und allgemeine Chemie*, 640(15):3070–3073, 2014.

[23] G. de la Flor, D. Orobengoa, E. Tasci, J. M. Perez-Mato, and M. I. Aroyo. *Journal of Applied Crystallography*, 49(2):653–664, 2016.

[24] A. Demont, C. Prestipino, O. Hernandez, E. Elkaim, S. Paofai, N. Naumov, B. Fontaine, R. Gautier, and S. Cordier. *Chemistry - A European Journal*, 19(38):12711–12719, 2013.

[25] D. Di Stefano, A. Miglio, K. Robeyns, Y. Filinchuk, M. Lechartier, A. Senyshyn, H. Ishida, S. Spannenberger, D. Prutsch, S. Lunghammer, D. Rettenwander, M. Wilkening, B. Roling, Y. Kato, and G. Hautier. *Chem*, 5(9):2450–2460, 2019.

[26] K. M. Diederichsen, H. G. Buss, and B. D. McCloskey. *Macromolecules*, 50(10):3831–3840, 2017.

[27] C. Dietrich, M. Sadowski, S. Sicolo, D. A. Weber, S. J. Sedlmaier, K. S. Weldert, S. Indris, K. Albe, J. Janek, and W. G. Zeier. *Chemistry of Materials*, 28(23):8764–8773, 2016.

[28] C. Dietrich, M. Sadowski, S. Sicolo, D. A. Weber, S. J. Sedlmaier, K. S. Weldert, S. Indris, K. Albe, J. Janek, and W. G. Zeier. *Journal of Materials Chemistry. A*, 5(34), 2017.

[29] C. Dietrich, D. A. Weber, S. Culver, A. Senyshyn, S. J. Sedlmaier, S. Indris, J. Janek, and W. G. Zeier. *Inorganic Chemistry*, 56(11):6681–6687, 2017. PMID: 28485931.

[30] A. C. Dippel, H. P. Liermann, J. T. Delitz, P. Walter, H. Schulte-Schrepping, O. H. Seeck, and H. Franz. *Journal of Synchrotron Radiation*, 22:675–687, 2015.

[31] M. Doyle, T. F. Fuller, and J. Newman. *Electrochimica Acta*, 39(13):2073 – 2081, 1994.

[32] C. F. Du, K. N. Dinh, Q. Liang, Y. Zheng, Y. Luo, J. Zhang, and Q. Yan. *Advanced Energy Materials*, 8(26):1–9, 2018.

[33] M. Duchardt, S. Neuberger, U. Ruschewitz, T. Krauskopf, W. G. Zeier, J. S. Auf Der Günne, S. Adams, B. Roling, and S. Dehnen. *Chemistry of Materials*, 30(12):4134–4139, 2018.

[34] A. Duvel, P. Heitjans, P. Fedorov, G. Scholz, G. Cibin, A. V. Chadwick, D. M. Pickup, S. Ramos, L. W. Sayle, E. K. Sayle, T. X. Sayle, and D. C. Sayle. *Journal of the American Chemical Society*, 139(16):5842–5848, 2017.

[35] A. Einstein. *Annalen der Physik*, 322:549–560, 1905.

[36] H. Every, A. G. Bishop, M. Forsyth, and D. R. MacFarlane. *Electrochimica Acta*, 45(8):1279–1284, 2000.

[37] T. Famprikis, P. Canepa, J. A. Dawson, M. S. Islam, and C. Masquelier. *Nature Materials*, 18:1278–1291, 2019.

[38] C. Y. Fan, X. H. Zhang, Y. H. Shi, H. Y. Xu, J. P. Zhang, and X. L. Wu. *Journal of Materials Chemistry A*, 7(4):1529–1538, 2019.

[39] C. L. Farrow, P. Juhas, J. W. Liu, D. Bryndin, E. S. Boin, J. Bloch, T. Proffen, and S. J. Billinge. *Journal of Physics Condensed Matter*, 19(33), 2007.

[40] J. Filik, A. W. Ashton, P. C. Y. Chang, P. A. Chater, S. J. Day, M. Drakopoulos, M. W. Gerring, M. L. Hart, O. V. Magdysyuk, S. Michalik, A. Smith, C. C. Tang, N. J. Terrill, M. T. Wharmby, and H. Wilhelm. *Journal of Applied Crystallography*, 50(3):959–966, 2017.

[41] K. D. Fong, J. Self, K. M. Diederichsen, B. M. Wood, B. D. McCloskey, and K. A. Persson. *ACS Central Science*, 5(7):1250–1260, 2019.

[42] M. Forsyth, J. Sun, D. R. Macfarlane, and A. J. Hill. *Journal of Polymer Science Part B: Polymer Physics*, 38(2):341–350, 2000.

[43] C. Fritsch, A.-L. Hansen, S. Indris, M. Knapp, and H. Ehrenberg. *Dalton Trans.*, 49:1668–1673, 2020.

[44] C. Fritsch, A.-L. Hansen, T. Zinkevich, S. Indris, T. Bergfeldt, and M. Knapp. *in preparation*, 2021.

[45] T. Fuchs, S. P. Culver, P. Till, and W. G. Zeier. *ACS Energy Letters*, 5(1):146–151, 2020.

[46] G. S. Fulcher. *Journal of the American Ceramic Society*, 8(6):339–355, 1925.

[47] J. Gai, E. Zhao, F. Ma, D. Sun, X. Ma, Y. Jin, Q. Wu, and Y. Cui. *Journal of the European Ceramic Society*, 38(4):1673 – 1678, 2018.

[48] C. Galven, J. Dittmer, E. Suard, F. Le Berre, and M. P. Crosnier-Lopez. *Chemistry of Materials*, 24(17):3335–3345, 2012.

[49] C. Galven, J.-L. Fourquet, M.-P. Crosnier-Lopez, and F. Le Berre. *Chemistry of Materials*, 23(7):1892–1900, 2011.

[50] F. Gam, C. Galven, A. Bulou, F. Le Berre, and M.-P. Crosnier-Lopez. *Inorganic Chemistry*, 53(2):931–934, 2014.

[51] B. M. Gatehouse and A. D. Wadsley. *Acta Crystallographica*, 17(12):1545–1554, 1964.

[52] C. A. Geiger, E. Alekseev, B. Lazic, M. Fisch, T. Armbruster, R. Langner, M. Fechtelkord, N. Kim, T. Pettke, and W. Weppner. *Inorganic Chemistry*, 50(3):1089–1097, 2011. PMID: 21188978.

[53] M. Ghidiu, J. Ruhl, S. P. Culver, and W. G. Zeier. *J. Mater. Chem. A*, 7(30):17735–17753, 2019.

[54] A. M. Glass, K. Nassau, and T. J. Negran. *Journal of Applied Physics*, 49(9):4808–4811, 1978.

[55] J. Goodenough, H.-P. Hong, and J. Kafalas. *Materials Research Bulletin*, 11(2):203 – 220, 1976.

[56] W. Gorecki, M. Jeannin, E. Belorizky, C. Roux, and M. Armand. *Journal of Physics: Condensed Matter*, 7(34):6823–6832, 1995.

[57] F. M. Gray. *Polymer electrolytes.* RSC Materials Monographs. Royal Society of Chemistry, United Kingdom, 1997.

[58] F. Han, Y. Zhu, X. He, Y. Mo, and C. Wang. *Advanced Energy Materials*, 6(8):1501590, 2016.

[59] J. Han, J. Zhu, Y. Li, X. Yu, S. Wang, G. Wu, H. Xie, S. C. Vogel, F. Izumi, K. Momma, Y. Kawamura, Y. Huang, J. B. Goodenough, and Y. Zhao. *Chem. Commun.*, 48:9840–9842, 2012.

[60] A.-K. Harm, Saschaand Hatz, I. Moudrakovski, R. Eger, A. Kuhn, C. Hoch, and B. V. Lotsch. *Chemistry of Materials*, 31(4):1280–1288, 2019.

[61] H. Hartung. *Journal für Praktische Chemie/Chemiker-Zeitung*, 340(2):187–188, 1998.

[62] K. Hayamizu, Y. Aihara, and W. S. Price. *The Journal of Chemical Physics*, 113(11):4785–4793, 2000.

[63] A. Hayashi, K. Noi, N. Tanibata, M. Nagao, and M. Tatsumisago. *Journal of Power Sources*, 258(Supplement C):420 – 423, 2014.

[64] X. He, Q. Bai, Y. Liu, A. M. Nolan, C. Ling, and Y. Mo. *Advanced Energy Materials*, 9(43):1–12, 2019.

[65] P. Heitjans and S. Indris. *Journal of Physics Condensed Matter*, 15(30), 2003.

[66] P. Heitjans, A. Schirmer, and S. Indris. 2005.

[67] J. Hendrickson and P. Bray. *Journal of Magnetic Resonance (1969)*, 9(3):341 – 357, 1973.

[68] H.-P. Hong. *Materials Research Bulletin*, 11(2):173 – 182, 1976.

[69] B. H. Hou, Y. Y. Wang, Q. L. Ning, H. J. Liang, X. Yang, J. Wang, M. Liu, J. P. Zhang, X. Wang, and X. L. Wu. *Advanced Electronic Materials*, 5(3):1–10, 2019.

[70] W. Hua, K. Wang, M. Knapp, B. Schwarz, S. Wang, H. Liu, J. Lai, M. Müller, A. Schökel, A. Missyul, D. Ferreira Sanchez, X. Guo, J. R. Binder, J. Xiong, S. Indris, and H. Ehrenberg. *Chemistry of Materials*, 32(12):4984–4997, 2020.

[71] A. A. Hubaud, D. J. Schroeder, B. J. Ingram, J. S. Okasinski, and J. T. Vaughey. *Journal of Alloys and Compounds*, 644:804–807, 2015.

[72] A. A. Hubaud, D. J. Schroeder, B. Key, B. J. Ingram, F. Dogan, and J. T. Vaughey. *J. Mater. Chem. A*, 1:8813–8818, 2013.

[73] T. Hupfer, E. Bucharsky, K. Schell, and M. Hoffmann. *Solid State Ionics*, 302:49 – 53, 2017. ISSFIT12.

[74] H. Hyooma and K. Hayashi. *Materials Research Bulletin*, 23(10):1399–1407, 1988.

[75] S. Indris, P. Heitjans, R. Uecker, and B. Roling. *Journal of Physical Chemistry C*, 116(27):14243–14247, 2012.

[76] J. T. Irvine, D. C. Sinclair, and A. R. West. *Advanced Materials*, 2(3):132–138, 1990.

[77] H. Jagodzinski. *Berichte der Bunsengesellschaft für physikalische Chemie*, 79(6):553–553, 1975.

[78] J. Janek and W. G. Zeier. *Nature Energy*, 1(9):16141, 2016.

[79] P. Jayathilaka, M. Dissanayake, I. Albinsson, and B.-E. Mellander. *Electrochimica Acta*, 47(20):3257 – 3268, 2002.

[80] Y. Jiang, Y. Zhou, Z. Hu, Y. Huang, and X. Zhu. *Ceramics International*, 2019.

[81] P. Juhas, T. Davis, C. L. Farrow, and S. J. Billinge. *Journal of Applied Crystallography*, 46(2):560–566, 2013.

[82] T. Kato, T. Hamanaka, K. Yamamoto, T. Hirayama, F. Sagane, M. Motoyama, and Y. Iriyama. In-situ li7la3zr2o12/licoo2 interface modification for advanced all-solid-state battery. *Journal of Power Sources*, 260:292–298, 2014.

[83] M. Kaus, M. Guin, M. Yavuz, M. Knapp, F. Tietz, O. Guillon, H. Ehrenberg, and S. Indris. *The Journal of Physical Chemistry C*, 121(3):1449–1454, 2017.

[84] M. Kaus, H. Stöffler, M. Yavuz, T. Zinkevich, M. Knapp, H. Ehrenberg, and S. Indris. *The Journal of Physical Chemistry C*, 121(42):23370–23376, 2017.

[85] M. Keller, G. B. Appetecchi, G.-T. Kim, V. Sharova, M. Schneider, J. Schuhmacher, A. Roters, and S. Passerini. *Journal of Power Sources*, 353:287–297, 2017.

[86] S. Ketabi and K. Lian. *Electrochimica Acta*, 154:404 – 412, 2015.

[87] K. H. Kim, Y. Iriyama, K. Yamamoto, S. Kumazaki, T. Asaka, K. Tanabe, C. A. Fisher, T. Hirayama, R. Murugan, and Z. Ogumi. *Journal of Power Sources*, 196(2):764–767, 2011.

[88] S. Kim, M. Hirayama, K. Suzuki, and R. Kanno. *Solid State Ionics*, 262:578 – 581, 2014. Solid State Ionics 19 Proceedings of the 19th International Conference on Solid State Ionics.

[89] T. Kim, W. Song, D.-Y. Son, L. K. Ono, and Y. Qi. *J. Mater. Chem. A*, 7:2942–2964, 2019.

[90] Y. Kim, D. Kim, R. Bliem, G. Vardar, I. Waluyo, A. Hunt, J. T. Wright, J. P. Katsoudas, and B. Yildiz. *Chemistry of Materials*, 2020.

[91] R. Koerver, F. Walther, I. Aygün, J. Sann, C. Dietrich, W. G. Zeier, and J. Janek. *J. Mater. Chem. A*, 5:22750–22760, 2017.

[92] M. Kotobuki and M. Koishi. *Ceramics International*, 39(4):4645 – 4649, 2013.

[93] M. Kotobuki, S. Song, C. Chen, and L. Lu. World scientific, 2018.

[94] B. Kozinsky. *Handbook of Materials Modeling*, pages 1–20, 2018.

[95] B. Kozinsky, S. A. Akhade, P. Hirel, A. Hashibon, C. Elsässer, P. Mehta, A. Logeat, and U. Eisele. *Physical Review Letters*, 116(5):1–5, 2016.

[96] M. A. Kraft, S. P. Culver, M. Calderon, F. Böcher, T. Krauskopf, A. Senyshyn, C. Dietrich, A. Zevalkink, J. Janek, and W. G. Zeier. *Journal of the American Chemical Society*, 139(31):10909–10918, 2017.

[97] C. Kranz and B. Mizaikoff. Chapter 6 - microscopic techniques for the characterization of gold nanoparticles. In M. Valcárcel and Ángela I. López-Lorente, editors, *Gold Nanoparticles in Analytical Chemistry*, volume 66 of *Comprehensive Analytical Chemistry*, pages 257–299. Elsevier, 2014.

[98] T. Krauskopf, R. Dippel, H. Hartmann, K. Peppler, B. Mogwitz, F. H. Richter, W. G. Zeier, and J. Janek. *Joule*, 3(8):2030 – 2049, 2019.

[99] T. Krauskopf, C. Pompe, M. A. Kraft, and W. G. Zeier. *Chemistry of Materials*, 29(20):8859–8869, 2017.

[100] M. Krengel, A. L. Hansen, M. Kaus, S. Indris, N. Wolff, L. Kienle, D. Westfal, and W. Bensch. *ACS Applied Materials and Interfaces*, 9(25):21282–21291, 2017.

[101] A. Kuhn, R. Eger, J. Nuss, and B. V. Lotsch. *Zeitschrift für anorganische und allgemeine Chemie*, 640(5):689–692, 2014.

[102] R. Kun, F. Langer, M. Delle Piane, S. Ohno, W. G. Zeier, M. Gockeln, L. Colombi Ciacchi, M. Busse, and I. Fekete. *ACS Applied Materials and Interfaces*, 10(43):37188–37197, 2018.

[103] V. Lacivita, A. S. Westover, A. Kercher, N. D. Phillip, G. Yang, G. Veith, G. Ceder, and N. J. Dudney. *Journal of the American Chemical Society*, 140(35):11029–11038, 2018.

[104] G. Larraz, A. Orera, J. Sanz, I. Sobrados, V. Diez-Gomez, and M. L. Sanjuan. *Journal of Materials Chemistry A*, 3(10):5683–5691, 2015.

[105] A. Le Bail, I. Madsen, L. M. D. Cranswick, J. K. Cockcroft, P. Norby, A. D. Zuev, A. Fitch, J. Rodriguez-Carvajal, C. Giacovazzo, R. B. Von Dreele, P. Scardi, N. C. Popa, R. Allmann, L. A. Solovyov, B. Hinrichsen, U. Schwarz, A. Altomare, A. Moliterni, R. Caliandro, R. Rizzi, N. V. Y. Scarlett, and M. Jansen. *Powder Diffraction*. The Royal Society of Chemistry, 2008.

[106] X. Lei, Y. Jee, and K. Huang. *J. Mater. Chem. A*, 3(39):19920–19927, 2015.

[107] Y. Li, X. Chen, A. Dolocan, Z. Cui, S. Xin, L. Xue, H. Xu, K. Park, and J. B. Goodenough. *Journal of the American Chemical Society*, 140(20):6448–6455, 2018.

[108] Y. Li, Z. Wang, Y. Cao, F. Du, C. Chen, Z. Cui, and X. Guo. *Electrochimica Acta*, 180:37 – 42, 2015.

[109] Z. Li, H.-M. Huang, J.-K. Zhu, J.-F. Wu, H. Yang, L. Wei, and X. Guo. *ACS Applied Materials & Interfaces*, 11(1):784–791, 2019.

[110] C. C. Liang. *Journal of The Electrochemical Society*, 120(10):1289, 1973.

[111] Q. Liang, L. Zhong, C. Du, Y. Luo, Y. Zheng, S. Li, and Q. Yan. *Nano Energy*, 47:257–265, 2018.

[112] T. Liu, Y. Zhang, X. Zhang, L. Wang, S. X. Zhao, Y. H. Lin, Y. Shen, J. Luo, L. Li, and C. W. Nan. *Journal of Materials Chemistry A*, 6(11):4649–4657, 2018.

[113] Y. Liu, J. Lee, and L. Hong. *Journal of Power Sources*, 109(2):507 – 514, 2002.

[114] A. Logéat, T. Köhler, U. Eisele, B. Stiaszny, A. Harzer, M. Tovar, A. Senyshyn, H. Ehrenberg, and B. Kozinsky. *Solid State Ionics*, 206:33 – 38, 2012.

[115] W. A. P. Luck. *Berichte der Bunsengesellschaft für physikalische Chemie*, 94(9):1047–1047, 1990.

[116] J. Malugani and G. Robert. *Solid State Ionics*, 1(5):519 – 523, 1980.

[117] D. Mazza. *Materials Letters*, 7(5):205–207, 1988.

[118] L. J. Miara, W. D. Richards, Y. E. Wang, and G. Ceder. *Chemistry of Materials*, 27(11):4040–4047, 2015.

[119] J. Mindemark, M. Lacey, T. Bowden, and D. Brandell. *Progress in Polymer Science*, 81:114 – 143, 2018.

[120] K. Momma and F. Izumi. *Journal of Applied Crystallography*, 44(6):1272–1276, 2011.

[121] K. Mori, T. Kasai, K. Iwase, F. Fujisaki, Y. Onodera, and T. Fukunaga. *Solid State Ionics*, 301:163–169, 2017.

[122] M. Motoyama, Y. Tanaka, T. Yamamoto, N. Tsuchimine, S. Kobayashi, and Y. Iriyama. *ACS Applied Energy Materials*, 2(9):6720–6731, 2019.

[123] R. Murugan, W. Weppner, P. Schmid-Beurmann, and V. Thangadurai. *Materials Science and Engineering: B*, 143(1):14 – 20, 2007.

[124] R. V. P. N. Bloembergen, E. M. Purcell. *Physical Review*, 137(2A), 1965.

[125] J. Narváez-Semanate and A. Rodrigues. *Solid State Ionics*, 181(25):1197 – 1204, 2010.

[126] P. K. Nayak, L. Yang, W. Brehm, and P. Adelhelm. *Angewandte Chemie International Edition*, 57(1):102–120, 2018.

[127] K. Noi, A. Hayashi, and M. Tatsumisago. *Journal of Power Sources*, 269(Supplement C):260 – 265, 2014.

[128] M. Nyman, T. M. Alam, S. K. McIntyre, G. C. Bleier, and D. Ingersoll. *Chemistry of Materials*, 22(19):5401–5410, 2010.

[129] S. Ohta, T. Kobayashi, J. Seki, and T. Asaoka. *Journal of Power Sources*, 202:332–335, 2012.

[130] A. Orera, G. Larraz, J. A. Rodriguez-Velamazan, J. Campo, and M. L. Sanjuan. *Inorganic Chemistry*, 55(3):1324–1332, 2016.

[131] V. Palomares, P. Serras, I. Villaluenga, K. B. Hueso, J. Carretero-Gonzalez, and T. Rojo. *Energy Environ. Sci.*, 5:5884–5901, 2012.

[132] K. Park, B. C. Yu, J. W. Jung, Y. Li, W. Zhou, H. Gao, S. Son, and J. B. Goodenough. *Chemistry of Materials*, 28(21):8051–8059, 2016.

[133] K. Pfeifer, S. Arnold, J. Becherer, C. Das, J. Maibach, H. Ehrenberg, and S. Dsoke. *ChemSusChem*, 12(14):3312–3319, 2019.

[134] K. Pfeifer, S. Arnold, z. Budak, X. Luo, V. Presser, H. Ehrenberg, and S. Dsoke. *J. Mater. Chem. A*, 8:6092–6104, 2020.

[135] K. Pfeifer, M. F. Greenstein, D. Aurbach, X. Luo, H. Ehrenberg, and S. Dsoke. *ChemElectroChem*, 7(16):3487–3495, 2020.

[136] E. M. Purcell, H. C. Torrey, and R. V. Pound. *Phys. Rev.*, 69:37–38, 1946.

[137] A. Rabenau. *Zeitschrift für anorganische und allgemeine Chemie*, 288(3-4):221–234, 1956.

[138] S. Randau, D. A. Weber, O. Kötz, R. Koerver, P. Braun, A. Weber, E. Ivers-Tiffée, T. Adermann, J. Kulisch, W. G. Zeier, F. H. Richter, and J. Janek. *Nature Energy*, 2020.

[139] D. Ravaine. *Journal of Non-Crystalline Solids*, 38-39:353 – 358, 1980. XIIth International Congress on Glass.

[140] Y. Ren, T. Liu, Y. Shen, Y. Lin, and C. W. Nan. *Journal of Materiomics*, 2(3):256–264, 2016.

[141] D. Rettenwander, P. Blaha, R. Laskowski, K. Schwarz, P. Bottke, M. Wilkening, C. A. Geiger, and G. Amthauer. *Chemistry of Materials*, 26(8):2617–2623, 2014.

[142] D. Rettenwander, J. Langer, W. Schmidt, C. Arrer, K. J. Harris, V. Terskikh, G. R. Goward, M. Wilkening, and G. Amthauer. *Chemistry of Materials*, 27(8):3135–3142, 2015.

[143] D. Rettenwander, G. Redhammer, F. Preishuber-Pflügl, L. Cheng, L. Miara, R. Wagner, A. Welzl, E. Suard, M. M. Doeff, M. Wilkening, J. Fleig, and G. Amthauer. *Chemistry of Materials*, 28(7):2384–2392, 2016.

[144] A. Reupert. Ionic conductivity and local structures in ball milled sodium thiophosphate solid electrolytes. Master thesis, Karlsruhe Institute of Technology, Institute for Applied Materials -Energy Storage Systems, 2020.

[145] E. Riedel and C. Janiak. *Anorganische Chemie*. DE GRUYTER, Berlin, München, Boston, 2015.

[146] H. M. Rietveld. *Journal of Applied Crystallography*, 2(2):65–71, 1969.

[147] L. Robben, E. Merzlyakova, P. Heitjans, and T. M. Gesing. *Acta Crystallographica Section E: Crystallographic Communications*, 72(2):287–289, 2016.

[148] T. Roisnel and J. Rodriguez-Carvajal. . *Materials Science Forum, Proceedings of the Seventh European Powder Diffraction Conference (EPDIC 7)*, pages 118–123, 1998.

[149] C. T. Rueden, J. Schindelin, M. C. Hiner, B. E. DeZonia, A. E. Walter, E. T. Arena, and K. W. Eliceiri. *BMC Bioinformatics*, 18(1):529, 2017.

[150] N. Schiffmann, E. C. Bucharsky, K. G. Schell, C. A. Fritsch, M. Knapp, and M. J. Hoffmann. *Ionics, accepted for publication*, 2021.

[151] R. Schlem, M. Ghidiu, S. P. Culver, A. L. Hansen, and W. G. Zeier. *ACS Applied Energy Materials*, 3(1):9–18, 2020.

[152] R. Schlenker. *Understanding the Solid-Electrolyte Li_6PS_5Cl and its Lifetime with Stripped and Plated Lithium Electrode*. PhD thesis, Karlsruhe Institute of Technology, 2020.

[153] U. Schubert. John Wiley & Sons, Ltd, 2015.

[154] R. Shakhovoy, M. Deschamps, A. Rakhmatullin, V. Sarou-Kanian, P. Florian, and C. Bessada. *Solid State Nuclear Magnetic Resonance*, 71:80 – 86, 2015.

[155] S. L. Shang, Z. Yu, Y. Wang, D. Wang, and Z. K. Liu. *ACS Applied Materials and Interfaces*, 9(19):16261–16269, 2017.

[156] A. Sharafi, E. Kazyak, A. L. Davis, S. Yu, T. Thompson, D. J. Siegel, N. P. Dasgupta, and J. Sakamoto. *Chemistry of Materials*, 29(18):7961–7968, 2017.

[157] H. Shen, E. Yi, S. Heywood, D. Y. Parkinson, G. Chen, N. Tamura, S. Sofie, K. Chen, and M. M. Doeff. *ACS Applied Materials & Interfaces*, 12(3):3494–3501, 2020.

[158] S. Shiotani, K. Ohara, H. Tsukasaki, S. Mori, and R. Kanno. *Scientific Reports*, 7(1):6972, 2017.

[159] D. J. Smith, Jeffrey G.and Siegel. *Nature Communications*, 11(1):1483, 2020.

[160] R. Snyder, J. Fiala, and H. Bunge. *Defect and Microstructure Analysis by Diffraction*. Oxford University Press, 1999.

[161] S. Srivastava, J. L. Schaefer, Z. Yang, Z. Tu, and L. A. Archer. *Advanced Materials*, 26(2):201–234, 2014.

[162] E. O. Stejskal and J. E. Tanner. *The Journal of Chemical Physics*, 42(1):288–292, 1965.

[163] N. C. Stephenson and R. S. Roth. *Acta Crystallographica Section B*, 27(5):1037–1044, 1971.

[164] H. Stöffler. *Charakterisierung der Struktur und Li-Transport-Eigenschaften von Feststoffelektrolyten in Li-Ionen Feststoffbatterien.* PhD thesis, Karlsruhe Institute of Technology, 2019.

[165] H. Stöffler, T. Zinkevich, M. Yavuz, A. L. Hansen, M. Knapp, J. Bednarcik, S. Randau, F. H. Richter, J. Janek, H. Ehrenberg, and S. Indris. *Journal of Physical Chemistry C*, 123(16):10280–10290, 2019.

[166] H. Stöffler, T. Zinkevich, M. Yavuz, A. Senyshyn, J. Kulisch, P. Hartmann, T. Adermann, S. Randau, F. H. Richter, J. Janek, S. Indris, and H. Ehrenberg. *The Journal of Physical Chemistry C*, 122(28):15954–15965, 2018.

[167] F. Strauss, T. Bartsch, L. De Biasi, A. Y. Kim, J. Janek, P. Hartmann, and T. Brezesinski. *ACS Energy Letters*, 3(4):992–996, 2018.

[168] A. Stukowski. *Modelling Simul. Mater. Sci. Eng.*, 18(1), 2010.

[169] R. Sudo, Y. Nakata, K. Ishiguro, M. Matsui, A. Hirano, Y. Takeda, O. Yamamoto, and N. Imanishi. *Solid State Ionics*, 262:151 – 154, 2014. Solid State Ionics 19 Proceedings of the 19th International Conference on Solid State Ionics.

[170] E. Takeshi and S. J. Billinge. Chapter 3 - the method of total scattering and atomic pair distribution function analysis. In T. Egami and S. J. Billinge, editors, *Underneath the Bragg Peaks*, volume 16 of *Pergamon Materials Series*, pages 55 – 111. Pergamon, 2012.

[171] G. Tammann and W. Hesse. *Zeitschrift für anorganische und allgemeine Chemie*, 156(1):245–257, 1926.

[172] X. Tan, Y. Wu, W. Tang, S. Song, J. Yao, Z. Wen, L. Lu, S. V. Savilov, N. Hu, and J. Molenda. Preparation of nanocomposite polymer electrolyte via in situ synthesis of sio2 nanoparticles in peo. *Nanomaterials*, 10(1), 2020.

[173] N. Tanibata, H. Tsukasaki, M. Deguchi, S. Mori, A. Hayashi, and M. Tatsumisago. *Solid State Ionics*, 311(Supplement C):6 – 13, 2017.

[174] J.-M. Tarascon. *Nature Chemistry*, 2:510, 2010.

[175] V. Thangadurai, H. Kaack, and W. J. Weppner. *Journal of the American Ceramic Society*, 86(3):437–440, 2003.

[176] G. Tian, Z. Zhao, T. Zinkevich, K. Elies, F. Scheiba, and H. Ehrenberg. *ChemSusChem*, 12(20):4708–4718, 2019.

[177] F. Tietz, T. Wegener, M. T. Gerhards, M. Giarola, and G. Mariotto. *Solid State Ionics*, 230(C):77–82, 2013.

[178] S. Uhlenbruck, J. Dornseiffer, S. Lobe, C. Dellen, C. L. Tsai, B. Gotzen, D. Sebold, M. Finsterbusch, and O. Guillon. *Journal of Electroceramics*, 38(2-4):197–206, 2017.

[179] L. Van Wüllen, T. Echelmeyer, H. W. Meyer, and D. Wilmer. *Physical Chemistry Chemical Physics*, 9(25):3298–3303, 2007.

[180] G. Vardar, W. J. Bowman, Q. Lu, J. Wang, R. J. Chater, A. Aguadero, R. Seibert, J. Terry, A. Hunt, I. Waluyo, D. D. Fong, A. Jarry, E. J. Crumlin, S. L. Hellstrom, Y. M. Chiang, and B. Yildiz. *Chemistry of Materials*, 30(18):6259–6276, 2018.

[181] L. Vegard. *Zeitschrift für Physik*, 5(1):17–26, 1921.

[182] J. Vila, P. Ginés, J. Pico, C. Franjo, E. Jiménez, L. Varela, and O. Cabeza. *Fluid Phase Equilibria*, 242(2):141 – 146, 2006.

[183] H. Vogel. *Phys. Z*, 22:645–646, 1921.

[184] M. von Smoluchowski. *Annalen der Physik*, 326(14):756–780, 1906.

[185] A. Wachter-Welzl, J. Kirowitz, R. Wagner, S. Smetaczek, G. Brunauer, M. Bonta, D. Rettenwander, S. Taibl, A. Limbeck, G. Amthauer, and J. Fleig. *Solid State Ionics*, 319:203 – 208, 2018.

[186] R. Wagner, G. Redhammer, D. Rettenwander, A. Senyshyn, W. Schmidt, M. Wilkening, and G. Amthauer. *Chemistry of Materials*, 28, 2016.

[187] R. Wagner, G. J. Redhammer, D. Rettenwander, G. Tippelt, A. Welzl, S. Taibl, J. Fleig, A. Franz, W. Lottermoser, and G. Amthauer. *Chemistry of Materials*, 28(16):5943–5951, 2016.

[188] Z. Wan, D. Lei, W. Yang, C. Liu, K. Shi, X. Hao, L. Shen, W. Lv, B. Li, Q. H. Yang, F. Kang, and Y. B. He. *Advanced Functional Materials*, 29(1):1–10, 2019.

[189] C. Wang, K. Fu, S. P. Kammampata, D. W. McOwen, A. J. Samson, L. Zhang, G. T. Hitz, A. M. Nolan, E. D. Wachsman, Y. Mo, V. Thangadurai, and L. Hu. *Chemical Reviews*, 120(10):4257–4300, 2020.

[190] D. Wang, Q. Sun, J. Luo, J. Liang, Y. Sun, R. Li, K. Adair, L. Zhang, R. Yang, S. Lu, H. Huang, and X. Sun. *ACS Applied Materials & Interfaces*, 11(5):4954–4961, 2019.

[191] A. F. Wells. *Structural inorganic chemistry*. Oxford, Oxfordshire, Clarendon Press, 5th ed edition, 1984.

[192] P. V. Wright. *British Polymer Journal*, 7(5):319–327, 1975.

[193] H. Xie, C. Yang, K. K. Fu, Y. Yao, F. Jiang, E. Hitz, B. Liu, S. Wang, and L. Hu. *Advanced Energy Materials*, 8(18):1–7, 2018.

[194] L. Xu, J. Li, W. Deng, H. Shuai, S. Li, Z. Xu, J. Li, H. Hou, H. Peng, G. Zou, and X. Ji. *Advanced Energy Materials*, 11(2):2000648, 2021.

[195] Z. Xue, D. He, and X. Xie. *J. Mater. Chem. A*, 3, 07 2015.

[196] H. Yamada, T. Ito, R. Hongahally Basappa, R. Bekarevich, and K. Mitsuishi. *Journal of Power Sources*, 368:97–106, 2017.

[197] Y. L. Yap, A. H. You, L. L. Teo, and H. Hanapei. *Int. J. Electrochem. Sci.*, 8:2154–2163, 2013.

[198] Z. Yu, S.-L. Shang, J.-H. Seo, D. Wang, X. Luo, Q. Huang, S. Chen, J. Lu, X. Li, Z.-K. Liu, and D. Wang. *Advanced Materials*, 29(16):1605561, 2017.

[199] W. Zaman, N. Hortance, M. B. Dixit, V. De Andrade, and K. B. Hatzell. *J. Mater. Chem. A*, 7:23914–23921, 2019.

[200] W. G. Zeier, S. Zhou, B. Lopez-Bermudez, K. Page, and B. C. Melot. *ACS Applied Materials and Interfaces*, 6(14):10900–10907, 2014.

[201] J. Zhang, N. Zhao, M. Zhang, Y. Li, P. K. Chu, X. Guo, Z. Di, X. Wang, and H. Li. *Nano Energy*, 28:447–454, 2016.

[202] N. Zhang, X. Long, Z. Wang, P. Yu, F. Han, J. Fu, G. Ren, Y. Wu, S. Zheng, W. Huang, C. Wang, H. Li, and X. Liu. *ACS Applied Energy Materials*, 1(11):5968–5976, 2018.

[203] Q. Zhang, D. Cao, Y. Ma, A. Natan, P. Aurora, and H. Zhu. *Advanced Materials*, 31, 2019.

[204] W. Zhang, F. H. Richter, S. P. Culver, T. Leichtweiss, J. G. Lozano, C. Dietrich, P. G. Bruce, W. G. Zeier, and J. Janek. *ACS Applied Materials and Interfaces*, 10(26):22226–22236, 2018.

[205] X. Zhao, G. Liang, and D. Lin. *RSC Adv.*, 7:37588–37595, 2017.

[206] J. Zheng, M. Tang, and Y. Y. Hu. *Angewandte Chemie - International Edition*, 55(40):12538–12542, 2016.

[207] J. Zhou and P. S. Fedkiw. *Solid State Ionics*, 166(3):275 – 293, 2004.

[208] Y. Zhu, X. He, and Y. Mo. *ACS Applied Materials and Interfaces*, 7(42):23685–23693, 2015.

Appendix
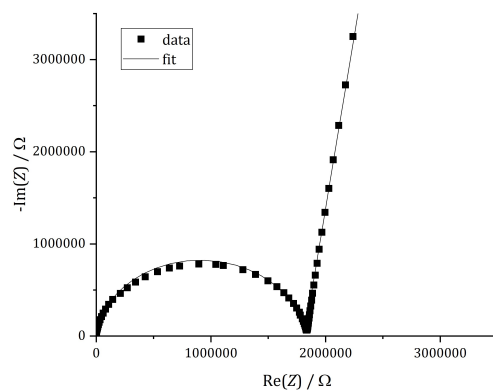
Figure 75 – Nyquist plot of impedance spectra of remilled calcined $Na_2P_2S_6$.
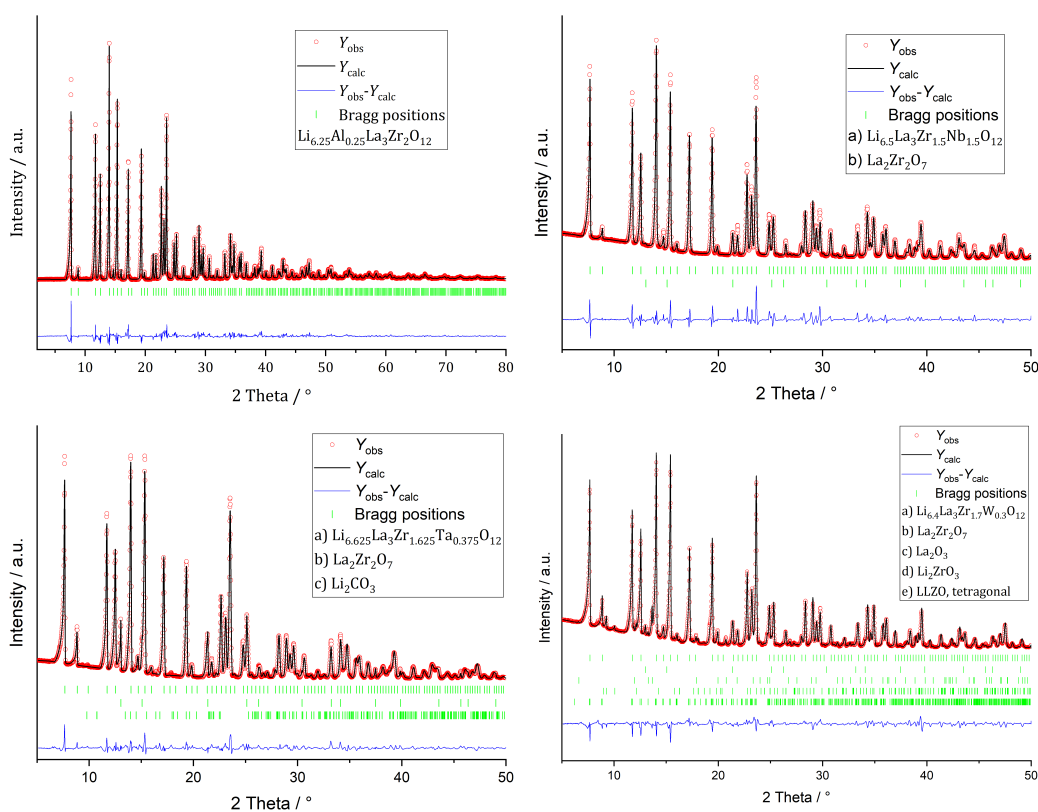
Figure 76 – Rietveld refinement of the structure models of synthesized LLZO, based on powder diffraction data (Mo K$_{\alpha1}$).

(a)

(b)
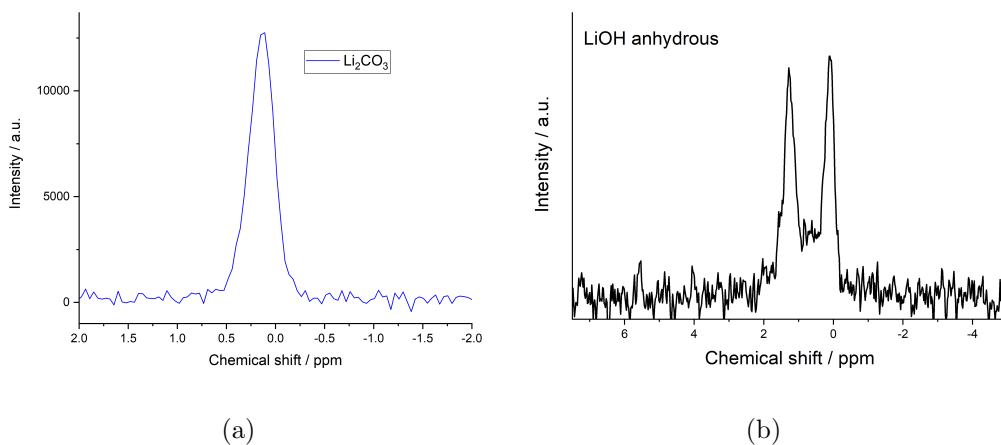
Figure 77 – a) ^{7}Li MAS NMR spectrum of Li_2CO_3, b) ^{6}Li MAS NMR spectrum of dried and anhydrous LiOH.
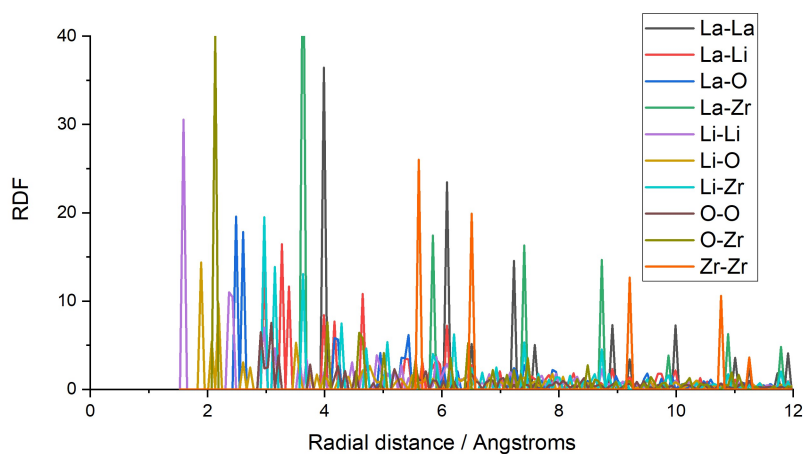
Figure 78 – Coordination analysis of a unsubstituted cubic garnet structure with OVITO.[168]
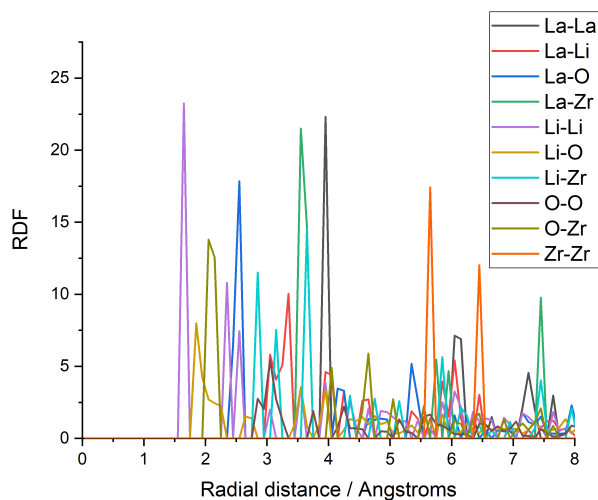
Figure 79 – Coordination analysis of a unsubstituted cubic hydrogarnet structure with OVITO.[168]

XVII

Table 15. – Structural model of Ta-LLZO with hydrogarnet structure.

	Phase 1	Phase 2
Space group	$I\bar{4}3d$	$I\bar{4}3d$
Lattice parameter a / Å	13.082	12.985
Cell volume V / Å^3	2237.8	2189.5
Li 12a x, y, z	0.37500, 0.00000, 0.25000	-
Li 12b x, y, z	-	0.87500, 0.00000, 0.25000
Li 48e x, y, z	0.15866, 0.11313, 0.43897	0.07017, 0.16488, 0.38160
Zr 16c x, y, z	-0.01589, -0.01589, -0.01589	-0.00841, -0.00841, -0.00841
Ta x, y, z	24d 0.11960, 0.00000, 0.25000	16c -0.00841, -0.00841, -0.00841
La 16c x, y, z	-0.01589, -0.01589, -0.01589	-
La 24d x, y, z	0.11960, 0.00000, 0.25000	0.11684, 0.00000, 0.25000
O 48e x, y, z	0.09460, 0.18790, 0.26781	0.02889, 0.46005, 0.14787
O 48e x, y, z	0.03650, 0.44616, 0.13666	0.11639, 0.18995, 0.27359
Structural strain d$D/D\cdot10^{-4}$	50.74	50.74

Table 16. – Results of the Rietveld refinement of synthesized Al-, Nb- Ta-, and W-substituted LLZO.

Substituent: Stoichiometry	Crystal structure	Lattice parameter a / Å	Cell volume / Å^3	Structural strain / $\mathrm{d}D/D \cdot 10^{-4}$
Al: $Li_{6.1}Al_{0.3}La_3Zr_2O_{12}$	Garnet	13.002	2198.04	20.87
Nb: $Li_{6.5}La_3Zr_{1.5}Nb_{0.5}O_{12}$	Garnet	12.959	2176.422	30.61
Ta: $Li_{6.625}La_3Zr_{1.625}Ta_{0.375}O_{12}$	Hydrogarnet / Garnet	13.007	2200.52	31.16
W: $Li_{6.4}La_3Zr_{1.7}W_{0.3}O_{12}$	Garnet	12.926	2159.894	18.08

Table 17. – Results of the ICP-OES analysis, n.a.: not analyzed.

Atom	%	Al-LLZO Mean	±	Nb-LLZO Mean	±	Ta-LLZO Mean	±	W-LLZO Mean	±
Li	(wt-%)	4.39	0.09	4.76	0.10	4.26	0.09	5.14	0.11
C	(wt-%)	0.956	0.083	1.30	0.11	2.52	0.22	0.620	0.054
O	(wt-%)	27.9	2.2	28.6	2.3	27.0	2.1	22.9	1.8
Al	(wt-%)	0.632	0.016	n.a.	-	n.a.	-	n.a.	-
Zr	(wt-%)	19.5	0.4	12.7	0.3	12.8	0.3	15.7	0.3
Nb	(wt-%)	n.a.	-	5.78	0.01	n.a.	-	n.a.	-
La	(wt-%)	45.6	-	42.3	-	39.3	-	43.4	-
Ta	(wt-%)	n.a.	-	n.a.	-	8.70	0.01	n.a.	-
W	(wt-%)	n.a.	-	n.a.	-	n.a.	-	6.79	0.23
Sum	(wt-%)	98.98		95.44		94.58		94.55	
Li	(Atom-%)	21.5		23.0		22.1		27.5	
C	(Atom-%)	-		-		-		-	
O	(Atom-%)	59.3		60.0		60.9		53.1	
Al	(Atom-%)	0.796		-		-		-	
Zr	(Atom-%)	7.27		4.67		5.06		6.39	
Nb	(Atom-%)	-		2.09		-		-	
La	(Atom-%)	11.2		10.2		10.2		11.6	
Ta	(Atom-%)	-		-		1.73		-	
W	(Atom-%)	-		-		-		1.37	
Sum	(Atom-%)	100.00		100.00		100.00		100.00	
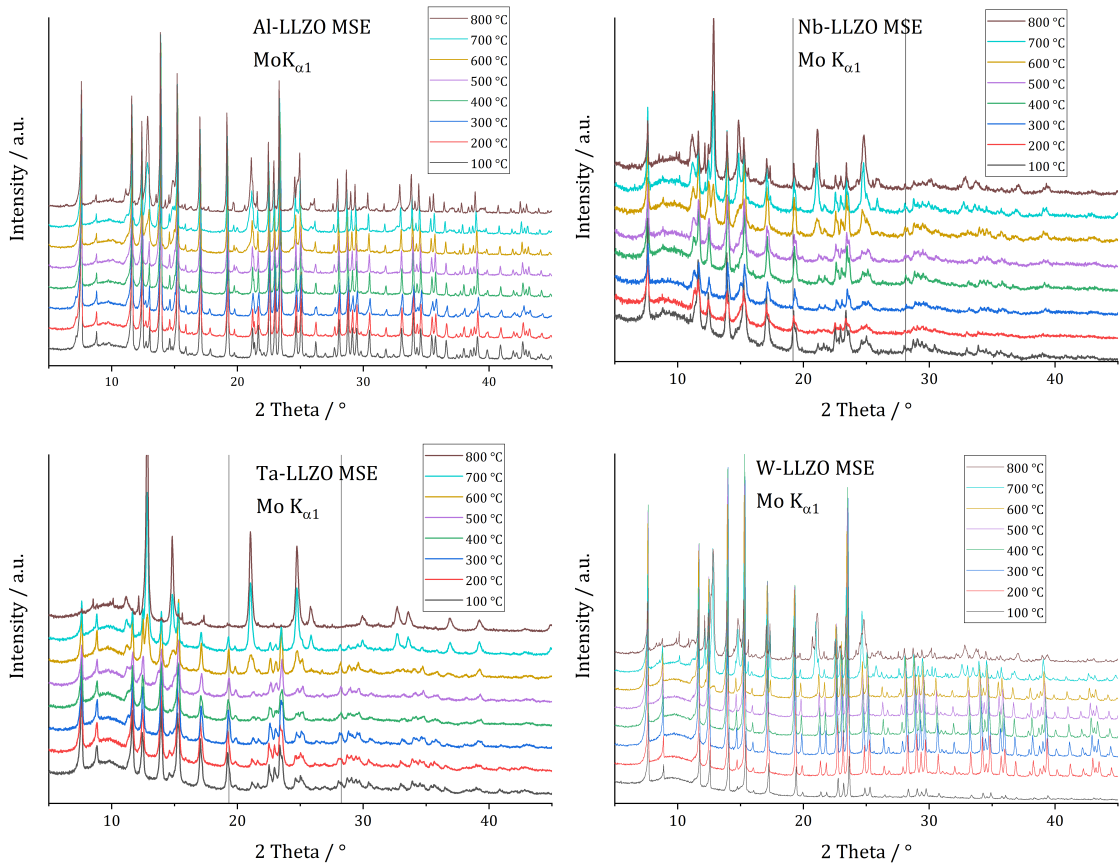
Figure 80 – High-temperature diffraction data of commercial LLZO samples.

(a)   (b)
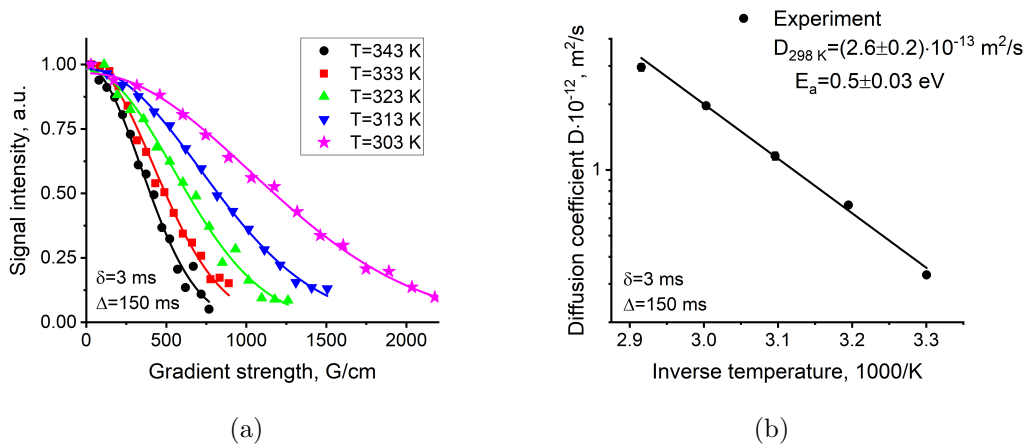
Figure 81 – Echo damping vs. gradient strength measurement of the commercial electrolyte nanomyte SE50.
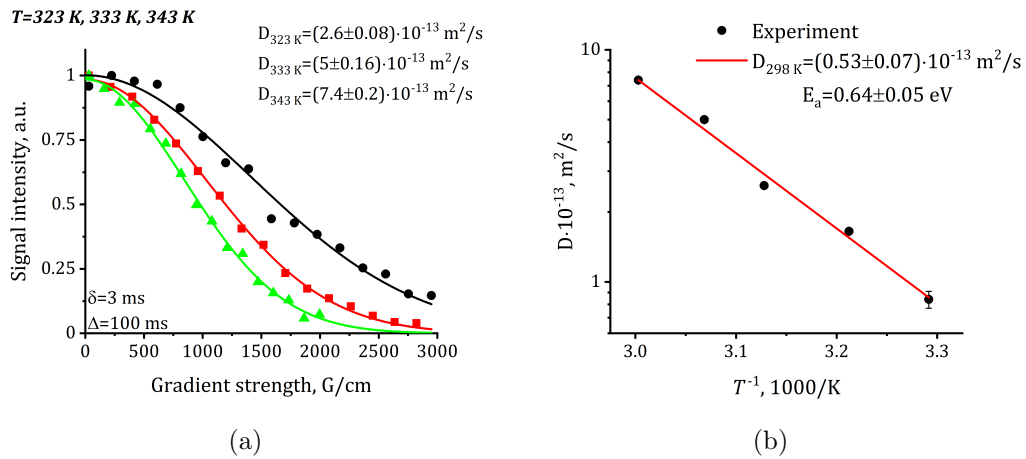
Figure 82 – Echo damping vs. gradient strength measurement of the commercial electrolyte H-
Polymer.
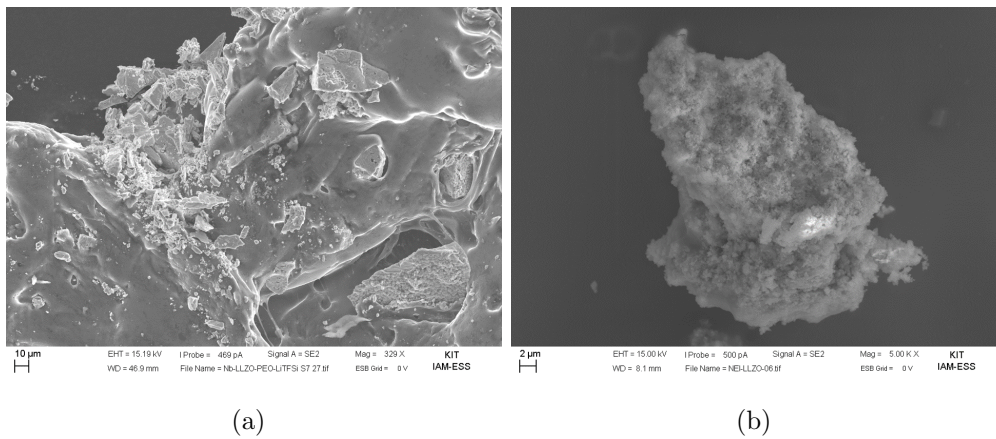
Figure 83 – SEM micrographs of a) synthesized composite electrolyte with garnet-type LLZO, b)
commercial composite electrolyte.

Figure 84 – a) commercal electrolyte nanomyte SE50, b) Li—nanomyte SE50—Li cells were burst-
ing after several days.

XXI
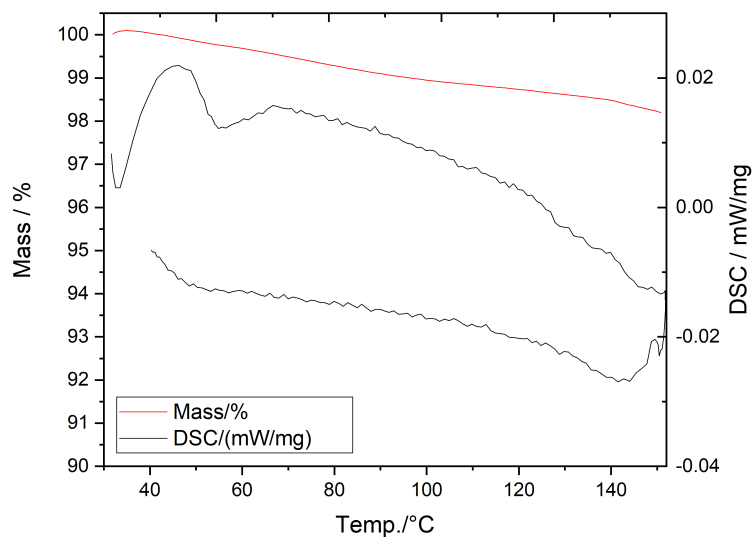
Figure 85 – Thermogravimetrical analysis of the commercial electrolyte nanomyte SE50. Exothermal ↓.

(a)   (b)
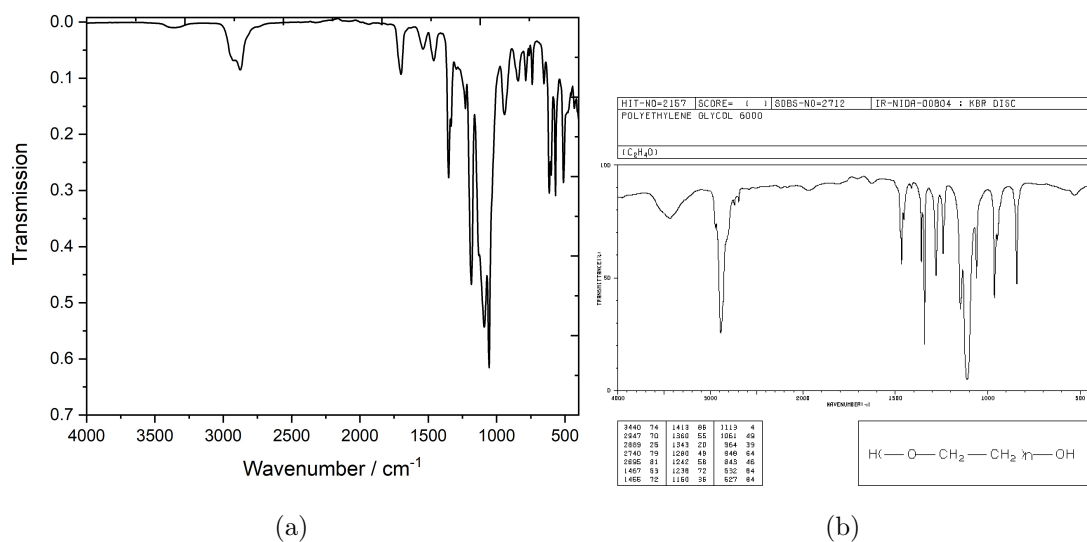
Figure 86 – a) Infrared spectrum of the commercial electrolyte nanomyte SE50, b) Infrared spectrum of polyethylene-oxide from SDBS database[1]
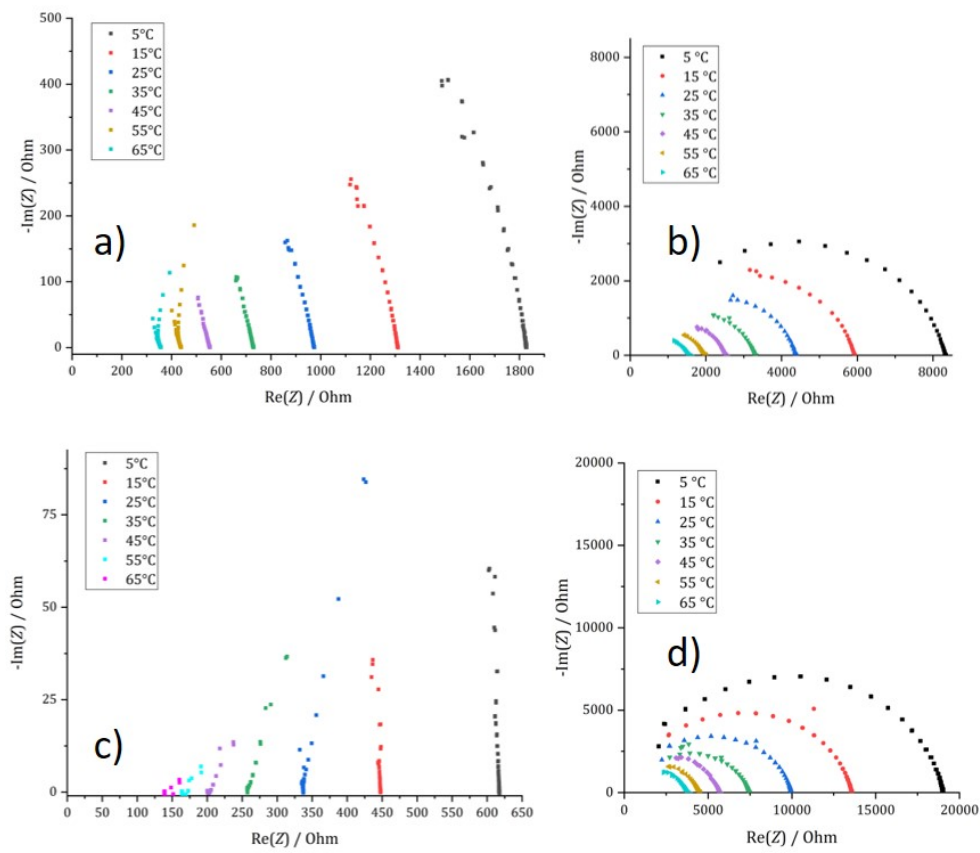
Figure 87 – Electrical impedance spectra of catholytes: a) Al-LLZO-NCM622 0.5:8, b) Al-LLZO-NCM622 1:1, c) Nb-LLZO-NCM622 0.5:8, d) Nb-LLZO-NCM622 1:1 (wt-%).
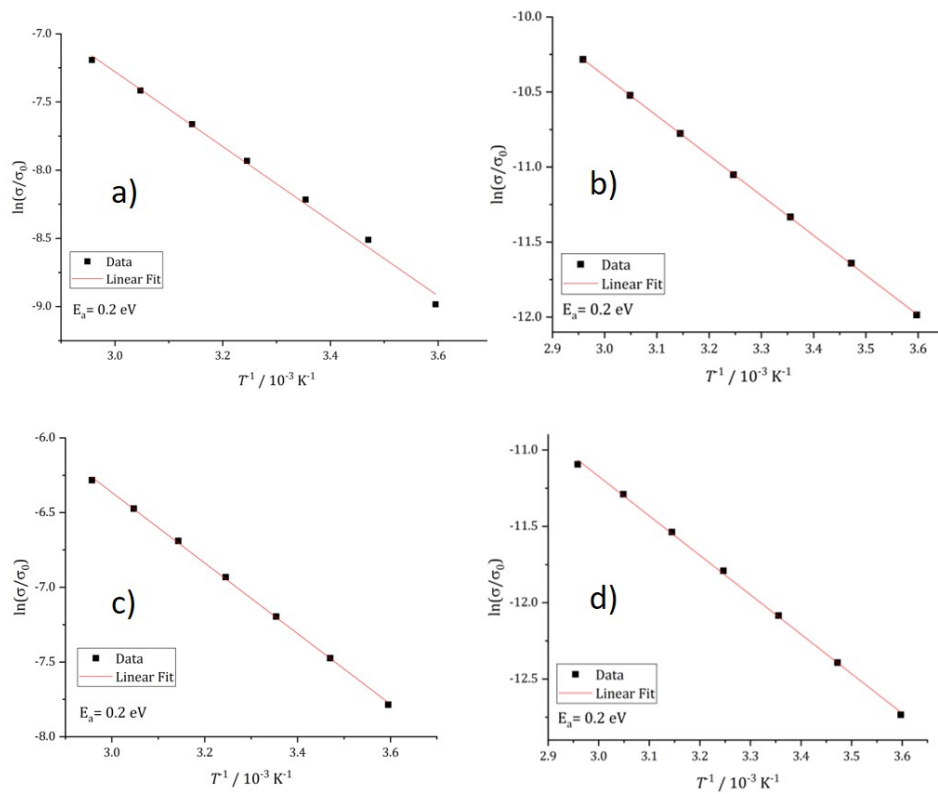
Figure 88 – Arrhenius fits of conductivities of catholytes from 5°C to 65 °C, a) Al-LLZO-NCM622 0.5:8, b) Al-LLZO-NCM622 1:1, c) Nb-LLZO-NCM622 0.5:8, d) Nb-LLZO-NCM622 1:1 (wt-%).
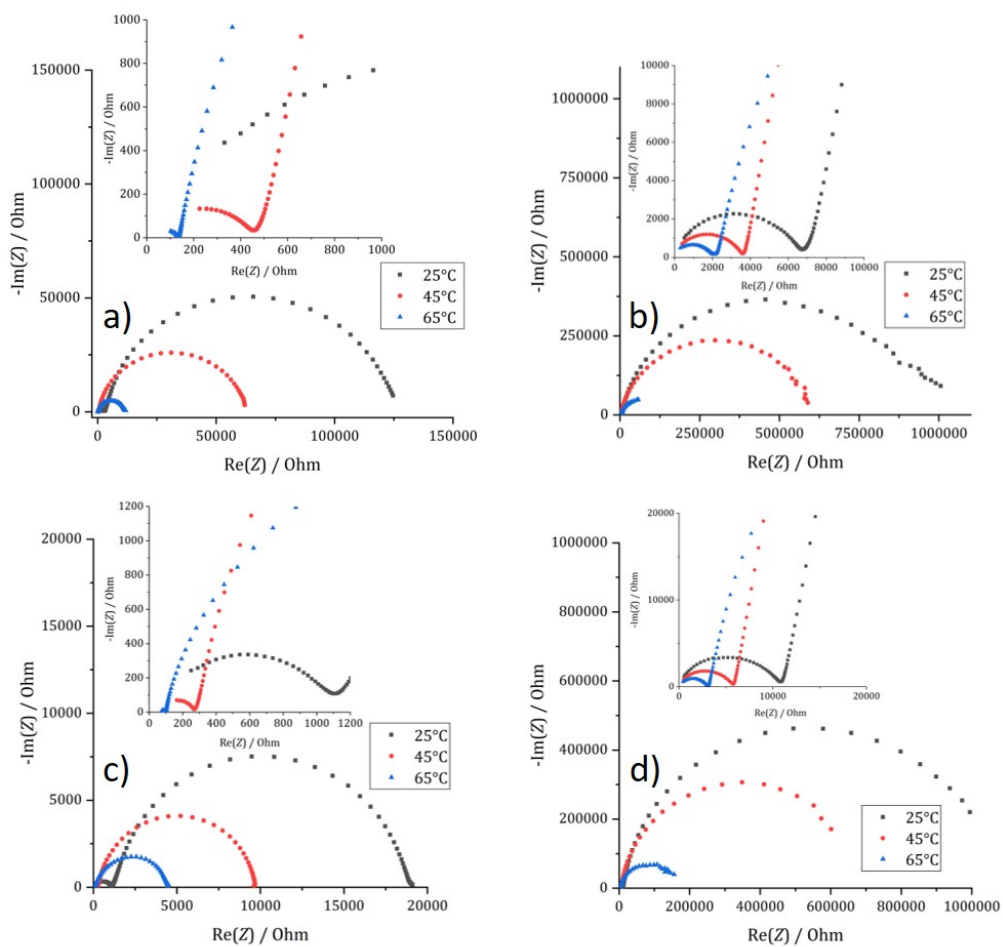
Figure 89 – Electrical impedance spectra of catholytes with auxiliary electrolyte at 25 ˚C, 45 ˚C, 65 ˚C, a) Al-LLZO-NCM622 0.5:8, b) Al-LLZO-NCM622 1:1, c) Nb-LLZO-NCM622 0.5:8, d) Nb-LLZO-NCM622 1:1 (wt-%).

(a)

(b)

(c)

(d)
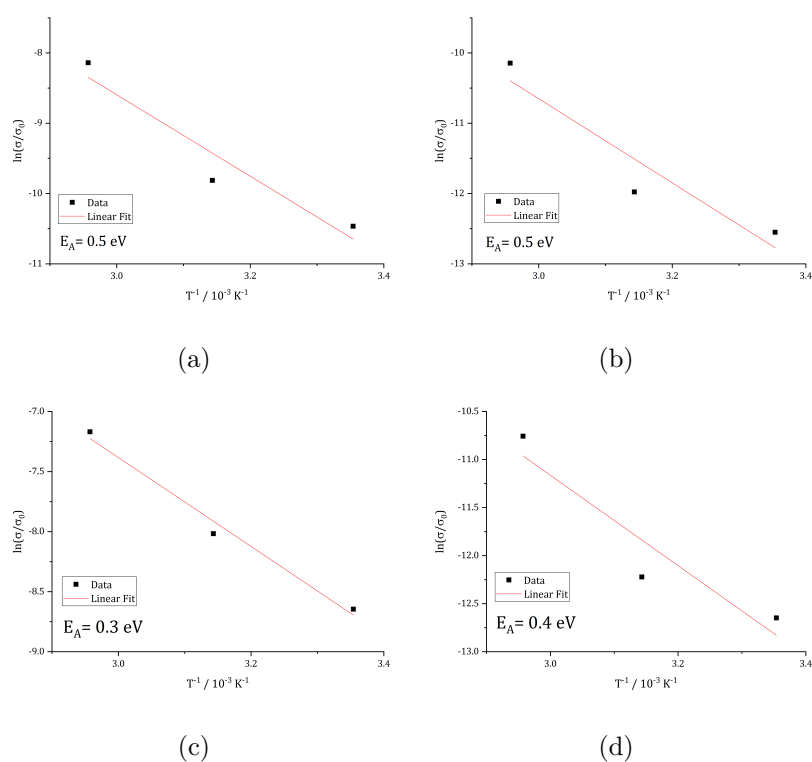
Figure 90 – Arrhenius fits of conductivities of catholytes with auxiliary electrolyte at 25 °C, 45 °C, 65 °C, a) Al-LLZO-NCM622 0.5:8, b) Al-LLZO-NCM622 1:1, c) Nb-LLZO-NCM622 0.5:8, d) Nb-LLZO-NCM622 1:1 (wt-%).
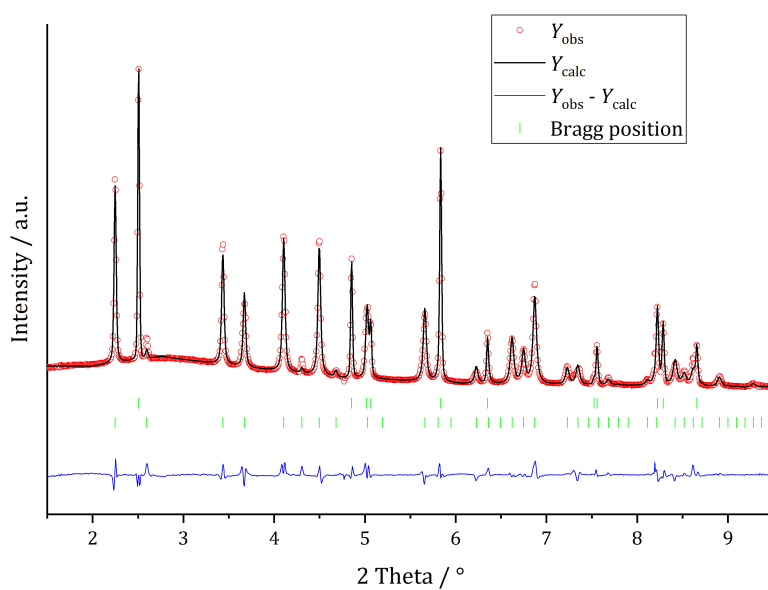
Figure 91 – Rietveld refinement of the structure models of a LLZO-NCM622-Carbon mixture 45:45:10 (wt-%) at 25 °C, based on powder diffraction data.
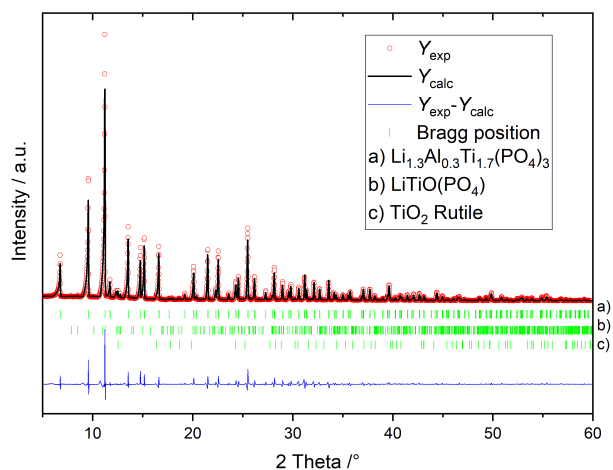
Figure 92 – Rietveld refinement of the structure model of sintered LATP, (1000 °C for 480 min) with phosphoric acid defiency, based on powder diffraction data (Mo $K_{\alpha 1}$).
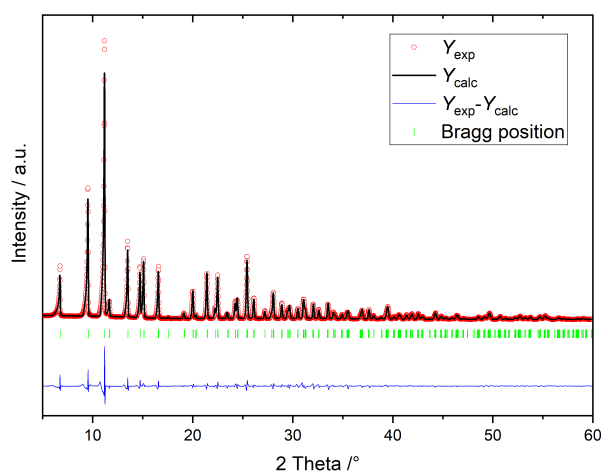
Figure 93 – Rietveld refinement of the structure model of sintered LATP, (900 °C for 30 min) in stoichiometric composition, based on powder diffraction data (Mo $K_{\alpha 1}$).
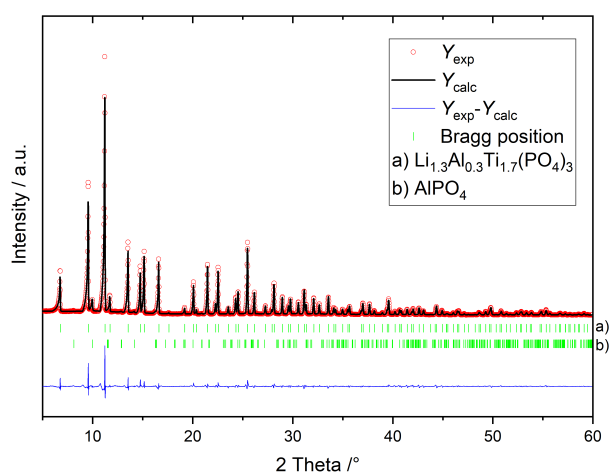
Figure 94 – Rietveld refinement of the structure model of sintered LATP, (900 °C for 480 min) with phosphoric acid excess, based on powder diffraction data (Mo $K_{\alpha 1}$).

XXVII

I. Note of thanks - Danksagung

II. Publications & Scientific contributions

Journals

(1)   Charlotte Fritsch, Anna-Lena Hansen, Sylvio Indris, Michael Knapp, Helmut Ehrenberg, Dalton Trans., 2020, 49, 1668-1673, *Mechanochemical synthesis of amorphous and crystalline $Na_2P_2S_6$ – Elucidation of local structural changes by X-ray total scattering and NMR,*
DOI: 10.1039/C9DT04777H

(2) Michael Poschmann, Hendrik Groß, Reza Amin, Charlotte Fritsch, Torben Dankwort, Hannes Radinger, Sylvio Indris, Lorenz Kienle, Wolfgang Bensch, Eur. J. Inorg. Chem. 2020, 1–12, *$CuCo_2S_4$ Deposited on TiO_2: Controlling the pH Value Boosts Photocatalytic Hydrogen Evolution,* DOI: 10.1002/ejic.202000555

(3)   Marc-André Serrer, Abhijeet Gaur, Jelena Jelic, Sebastian Weber, Charlotte Fritsch, Adam H. Clark, Erisa Saraçi, Felix Studt, Jan-Dierk Grunwaldt, Catal. Sci. Technol., 2020, Advance Article, *Structural dynamics in Ni–Fe catalysts during CO_2 methanation - role of iron oxide clusters,* DOI: 10.1039/D0CY01396J

Talks

(1)   Charlotte Fritsch, Anna-Lena Hansen, Sylvio Indris, Michael Knapp, Helmut Ehrenberg, *Local structure of glass-ceramic sodium sulfidic solid state electrolytes - What kind of P-S subunits do we have?,* EMRS Fall Meeting September 2019, Warsaw, Poland

(2)   Charlotte Fritsch, Anna-Lena Hansen, Sylvio Indris, Tatiana Zinkevich, Michael Knapp, Thomas Bergfeldt, Volodymyr Baran, and Helmut Ehrenberg, *LLZO: Al, Ta, Nb, W – different dopants and their effect on microstructure and lithium diffusion,* MRS Fall meeting, Boston, United states, December 2020

Posters

(1)   Charlotte Fritsch, Anna-Lena Hansen, Sylvio Indris, Michael Knapp, Helmut Ehrenberg, *Local structure of glass-ceramic sodium sulfidic solid state electrolytes,* ECM32, Vienna, Austria

(2)   Charlotte Fritsch, Anna-Lena Hansen, Sylvio Indris, Michael Knapp, Helmut Ehrenberg, *Granat oder Hydrogranat? Eine strukturelle Analyse mittels Diffraktion und NMR,* FestBatt Industrietag, virtual event.

(3) Charlotte Fritsch, Anna-Lena Hansen, Sylvio Indris, Michael Knapp, Volodymyr Baran, Thomas Bergfeldt, Helmut Ehrenberg, *Garnet or Hydrogarnet? A structural analysis with diffraction and NMR*, Deutsche Neutronenstreutagung. virtual event organized by Heinz Maier-Leibnitz Zentrum, Garching.

(4) Charlotte Fritsch, Anna-Lena Hansen, Sylvio Indris, Tatiana Zinkevich, Michael Knapp, Helmut Ehrenberg, *Granat oder Hydrogranat? Eine strukturelle Analyse mittels Diffraktion und NMR*, Batterieforum Detschland, virtual event.

Workshops & Sumer schools

(1) Shortcourse nuclear magnetic resonance spectroscopy, Deutsche Mineralogische Gesellschaft, Michael Fechtelkord, Ruhr Universität Bochum, 10.-14- June 2019.

(2) Analysis Diffraction Data, Insititute Laue-Langevin & European Synchrotron Reasearch Facility, Michela Brunelli, Gabriel Cuello, Henry Fischer, Gavin Vaughan, European Photon and Neutron campus Grenoble, France, 17-22 March 2019.

(3) Surface catalysis, Denmark Technical University, Birgit Bohn, Gilleleje, Denmark, 5-10 August 2018.